Molecular charge transport : relating orbital structures to the conductance properties

Guédon, C.M.

MOLECULAR CHARGE TRANSPORT

Relating orbital structures to the conductance properties

MOLECULAR CHARGE TRANSPORT

Relating orbital structures to the conductance properties

Proefschrift

ter verkrijging van
de graad van doctor aan de Universiteit Leiden,
op gezag van Rector Magnificus prof. mr. P. F. van der Heijden,
volgens besluit van het College voor Promoties
te verdedigen op dinsdag 6 november 2012
klokke 15:00 uur

door

Constant Marcel GUÉDON

geboren te Den Haag
in 1979

Promotiecommissie

Promotor:	Prof. dr. J. M. van Ruitenbeek	Universiteit Leiden
Copromotor:	Dr. ir. S. J. van der Molen	Universiteit Leiden
Overige leden:	Prof. Dr. E. R. Eliel	Universiteit Leiden
	Prof. Dr. B. Doudin	Université de Strasbourg
	Dr. ir. C. F. J. Flipse	Technische Universiteit Eindhoven
	Prof. Dr. ir. H. S. J. van der Zant	Technische Universiteit Delft
	Prof. Dr. M. van Hecke	Universiteit Leiden

Casimir PhD Series, Delft-Leiden 2012-30

ISBN 978-90-8593-136-2

An electronic version of this dissertation is available at
http://www.physics.leidenuniv.nl/sections/cm/amc/.

Printed by: Gildeprint Drukkerijen

Front & Back: Constant Guédon

LaTeX template: Jos Seldenthuis

Voor Lucas

Contents

Thesis Outline

Chapter 1 (p. 1)
Basic concepts.

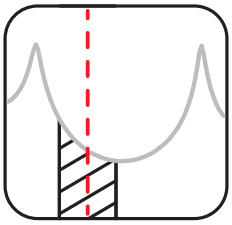

In this chapter we present the basic concepts of molecular charge transport. We also introduce the most common measurement methodologies.

Chapter 2 (p. 23)
2D nanoparticle networks for molecular electronics

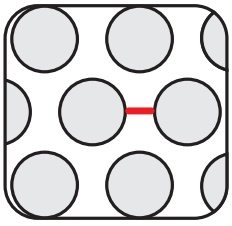

In this chapter we introduce a new approach to molecular charge transport. We make use of a 2D nanoparticle network to connect the molecules, with the nanoparticles acting as miniature electrodes. This technique allows for additional optical measurements on the devices.

Chapter 3 (p. 59)
Nanoparticle array based strain sensor.

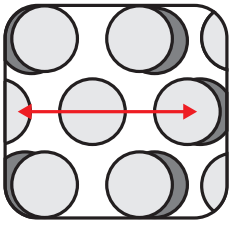

Here, we combine mechanically controlled break junctions and 2D nanoparticle networks to create a robust platform for molecular charge transport measurements with control over the interelectrode distance on the picometer scale. The resistance change due to bending of our structures is dependent on the molecular species present between the nanoparticles.

1

Basic concepts

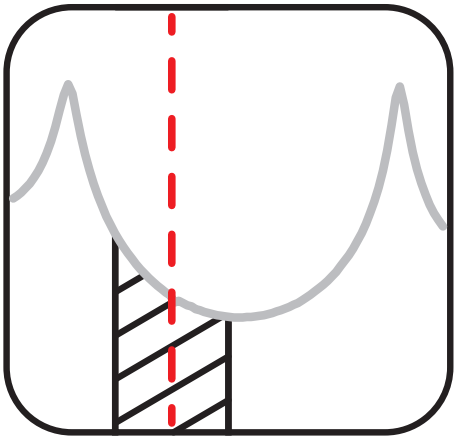

1.1 A BRIEF HISTORICAL VIEW ON MOLECULAR CHARGE TRANSPORT

The field of science that is now called molecular charge transport, emerged with the first measurements on metal-molecule-metal junctions by Mann and Kuhn already back in 1971 [1]. Shortly after a paper by Aviram and Ratner [2], this appealing idea gave a lot of momentum to this field. In their theoretical paper, they did not only predict the rectification properties of their designed molecular junction but also the challenges scientists would encounter trying to connect and characterize molecular junctions: "A large number of materials and synthesis problems must, clearly, be overcome before such molecular electronics device can be tested in the laboratory.". To this they added: " Efforts towards the solution of these problems are presently under way.", not knowing that it would cost at least twenty years before the first single molecule measurements were claimed [3, 4]. Since then the field of molecular electronics has been an active field developing numerous experiments and techniques. The field also has encountered many ups and downs [5–7]. Nevertheless scientists kept working on the possibilities of contacting molecules developing new methodologies and improving the measurements techniques. By now, the field has gained maturity and the focus is on carefully exploring molecular charge transport.

The promise of molecular electronics in Aviram and Ratner's seminal paper is, as the name already says, to integrate molecular junctions to replace the ever shrinking integrated circuit components. This has motivated most of the research in the field even though no direct application in integrated circuitry has been found yet. But the truly exciting side of molecular electronics is the fundamental questions it raises. Indeed studying the charge transport in molecular species profits from the versatility of organic chemistry to systematically vary the properties of microscopic conductors contacted by macroscopic leads. The physics of such systems is often referred to as mesoscopic physics. Indeed mesoscopic physics functions as a bridge between the macroscopic world of the bulk materials and the microscopic world of atoms. So we may say that molecular junctions are well suited and versatile tools to study mesoscopic charge transport phenomena. In this chapter we will first introduce some basic concepts about charge transport through nanometer-scale objects and see how molecular junctions fit in this picture. This is followed by a short description of the principal methodologies to connect molecules to electrodes.

1.2 Basic concepts

1

1.2.1 Conductance quantization

When dealing with conductors on the nanometer scale a few length scales are of great importance, namely: i) L_i, (with $i = x, y, z$) the characteristic dimensions of the conductor in the x, y and z directions (z being in the direction of charge transport). ii) l_e, the elastic scattering length for electrons (or mean free path)i.e. the distance an electron can travel without experiencing an elastic scattering event (walls, dislocations, impurities). iii) l_φ, the phase coherence length i.e. the distance an electron can travel before its phase is randomized. iv) λ_F, the Fermi wavelength, the wavelength of the electrons at the Fermi energy i.e. the electrons responsible for the transport phenomena we describe. The relation between those length scales determine to a great extent the way electrons move through a conductor.

So now, more specifically, if we connect a conductor with dimensions such that $L_{x,y} \ll l_e, l_\varphi$ and $L_{x,y} \sim \lambda_F$ and $l_e, l_\varphi < L_z \gg \lambda_F$, we are in the so called quantum ballistic regime. We can calculate the density of states in such a quantum ballistic conductor by solving the time-independent Schrödinger equation. The solutions to it are the transversal modes propagating in the z-direction. The corresponding energy for these modes is given in equation 1.1 [8]. Solely the modes with an energy crossing the Fermi level do contribute to the conduction.

$$E = \frac{\hbar^2}{2m} \sum_{i=x,y,z} \left(\frac{n_i \pi}{L_i} \right)^2 \tag{1.1}$$

If $L_z \to \infty$ the energy of the electrons are quantized in the x and y direction while continuous in the z direction. Now we know the electron energy, we can express the conductance of the conductor. If the dimensions $L_{x,y}$ for our conductor are small, the resulting energy spacing will be large so we can restrict our discussion to one single mode or conductance channel. We apply a bias of eV_b on the conductor, shifting the chemical potentials μ_L and μ_R of the electrodes (reservoirs) with respect to each other so that: $\mu_L - \mu_R = eV$. We can calculate the density of states, ρ in this single channel (equation 1.2) [8].

$$\rho(E) = \frac{1}{\pi\hbar} \sqrt{\frac{m}{2E}} \tag{1.2}$$

Finally we can express the current by integrating over the density of states, limiting for the right-moving electrons and correcting for the spin degeneracy (equation 1.3) and over $v(E) = \sqrt{2E/m}$ the electron velocity and f_R and f_L the

Fermi-Dirac functions for the right and left electrode respectively (equation 1.4).

$$I = \int_{-\infty}^{\infty} ev(E)\rho(E)(f_L - f_R)dE = \frac{2e^2}{h}V_b \tag{1.3}$$

$$f_{L,R} = \left(1 + \exp\left(\frac{\varepsilon - \mu_{L,R}}{k_B T}\right)\right)^{-1} \tag{1.4}$$

We see here that for an ideal single channel conductor, the conductance G, can be expressed as a function of fundamental constants and it is independent of the length L_z. This fundamental conductance is called the quantum of conductance $G_0 = \frac{2e^2}{h}$. The conductance increases in steps of $\frac{2e^2}{h}$ for an increasing number of channels. The conductance quantization has been first observed in 1988 by van Wees *et al.* in a two dimensional electron gas (2DEG) by tuning the width of the channels with electrostatic gates[9]. The Fermi wavelength in the semiconductor used (GaAs) was in the order of 200 nm, resulting in separation of the modes in the order of meV's and thus requiring low temperatures ($\sim$ 1 K) to resolve the steps. Quantized conductance is also observed in metals, where the Fermi wavelength is about two orders of magnitude smaller ($\lambda_{F,Au} \sim 0.5$ nm) requiring contacts of atomic dimensions to have the conductance quantized[10]. The small dimensions of the atomic contact result in a much larger separation of the modes ($\sim$ eV) as compared to 2DEG's making the observation of quantized conductance possible at room temperature [10].

1.2.2 LANDAUER-BÜTTIKER FORMALISM

The situation above is described in a more generalized way by Landauer and Büttiker by treating the conductor as a scatterer that couples incoming states (I) and outgoing states (O) phase-coherently via a scattering matrix as shown in figure 1.1 and equation 1.5 [11, 12].

$$\begin{pmatrix} O_L \\ O_R \end{pmatrix} = \begin{pmatrix} r & t' \\ t & r' \end{pmatrix} \begin{pmatrix} I_L \\ I_R \end{pmatrix} \tag{1.5}$$

The matrices r and t denote the reflection and transmission when the states are coming from the left and r' and t' when the states are coming from the right. Current conservation imposes that $rr^\dagger + tt^\dagger = r'r'^\dagger + t't'^\dagger$. The eigenvalues of $tt^\dagger$ correspond to the transmission probability T_n for all the n eigenchannels of the scatterer. We can now express the conductance as follow:

$$G = G_0 \sum_n T_n \tag{1.6}$$

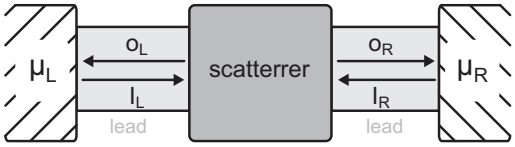

FIGURE 1.1: **Representation of the scattering approach used by Landauer and Büttiker.** μ_L and μ_R are the chemical potentials of the left and right reservoirs respectively. The scatterer is connected to the reservoirs by two fully transparent leads. O_L and O_R represent the outgoing states to the left and right respectively. I_L and I_R represent the ingoing states from the left and right respectively.

In general, we can extend equation 1.6 with an energy dependent transmission for the current through a scatterer (as the channels have independent eigenstates).

$$I = \frac{2e}{h}\int_o^\infty T(E)(f_R - f_L)dE \tag{1.7}$$

If we consider conductors involving more electronic orbitals the picture gets more complicated. The Landauer-Büttiker formalism still can be applied together with more involved calculations to find the corresponding T(E) as we will see later on.

1.2.3 A MOLECULE AS A CONDUCTOR

Until now we discussed purely ballistic transport in conductors contacted by transparent leads (reservoirs, leads and conductor made out of the same material). Small organic molecules (nanoscale) tend to fulfill the requirements for ballistic transport at room temperature as their size is still much smaller than the characteristic lengths for electrons (l_e and l_φ). So if we insert organic molecules between the leads what will happen to the transmission characteristics? An important parameter here is the extent to which the molecule interacts with the electrodes, the so-called coupling that we will discuss later on. At one side we have the strong coupling limit where the overlap of the molecular wavefunctions and electrodes wavefunctions is so that we can describe it as a quasi-ballistic conductor i.e. the measured single-molecule conductances will be close to G_0 [13, 14]. At the other side of the spectrum we have the weak coupling limit where the molecule interacts weakly with the leads, in fact in that case

the molecule is best described as a quantum dot. In this limit the Landauer approach does not hold anymore, indeed charging effects, like electron-electron interactions take place. In this thesis we consider the strong coupling limit. Molecules also differ from 'traditional' conductors in the sense that their composition and structure can be engineered by organic chemistry. Additionally in organic molecules the ion-electron interactions are stronger resulting in vibrational influences on the conductance making electronic spectroscopy possible (Inelastic tunneling spectroscopy and point contact spectroscopy [13]).

Organic chemistry tool-box

Organic chemistry offers the possibility to design molecules almost at will and thus engineer the resulting transmission function. Although relating the chemical structure to the conduction properties is still a challenging task, one can rely on empirical organic chemistry rules-of-thumb and on more evolved quantum chemistry calculations. A wide variety of molecules have been engineered. Series of aliphatic carbon chains have been synthesized to study the length dependence of the conduction through 'isolating' molecular wires (reference [15] for a review of the numerous experiments). Synthetically a bit more involved, series of conjugated molecules of variable length have been synthesized to study the length dependence of molecules with delocalized π-electrons [16–18] (chapter 5). For both groups of experiments on molecules the conduction appeared to be dependent of the length.

Chemists have introduced functionality to molecular conductors. One of the most appealing functionality is the possibility of switching from a low conductance state to a high conductance state by an external stimulus (for a review on molecular switches see reference [19]). Such switchable molecules are highly interesting for both applied and fundamental research. Indeed we can then probe two conducting states in exactly the same conditions. Different stimuli can be used to switch between the two conformations of the molecule. They can be switched by light [20], redox reaction [21], strain [22] or change in the electrochemical potential [23]. To illustrate the possibilities of engineering the conductance of molecule we present here a molecular switch. In figure 1.2 we show the chemical structures of the two conformations of an anthraquinone based switch and the associated change in the transmission function. The 'ON' state of the molecule is conjugated while in the 'OFF' state the conjugation is broken, which will lead to quantum interferences that suppress the transmission as can be seen in figure 1.2-B (see chapter 6 for more details). The important message here is that a only a small change in the chemical structure can induce large changes in the transmission function i.e. the conductance of molecule (see equation 1.7).

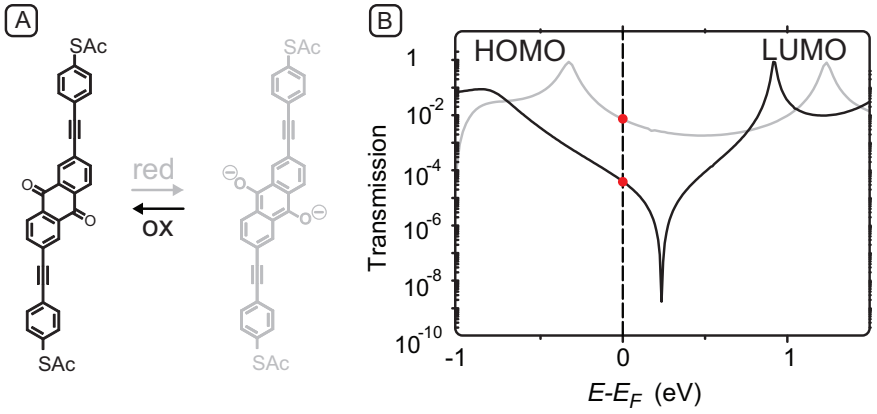

FIGURE 1.2: **Anthraquinone based switch [21]. A** Chemical structure of the two stable configurations of the switch. **B** Corresponding calculated energy-dependent transmission curves. The dots indicate the transmission at the Fermi energy and indicate almost two orders of magnitude difference in conductance (calculations by Troels Markussen).

Connecting the molecules electronically

The molecules need to be connected somehow to the electrodes in order to make charge transport study possible. The most used connection between the organic molecules and the electrodes is the sulfur-gold bond or thiol bond. Indeed a molecule terminated with a sulfur atom binds strongly to the gold electrodes, the bond strength is about 2.1 eV [24]. Besides the most widely used thiol binding a wide range of attachements groups have been used: amines [17], selenols [25], pyridines [26], carboxylic acids [27], isocianides [17] and phosphines [28] or no linking groups at all [13, 14, 29].

We will see that connecting a molecule to metal electrodes results in a dramatic change of its energy landscape. To get an physical intuitive picture of the effect of inserting a molecule in metal-molecule-metal junction, let us have a look at a simple tight-binding model for a virtual molecule. In figure 1.3-A we show the molecule in free space as an interacting chain of hopping sites. In figure 1.3-B we show the molecule connected to electrodes. We can write the corresponding Hamiltonians for the isolated molecule (equation 1.8) resulting

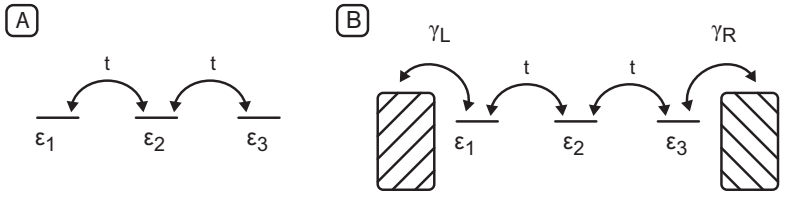

FIGURE 1.3: **Tight-binding representation of a molecule. A** Molecule composed of three site of energy ε and hopping integral t. **B** Same molecule as in A but connected to the electrodes by the coupling γ.

in discrete levels.

$$H_{(mol,isol)} = \begin{pmatrix} \varepsilon_1 & t & & \\ t & \varepsilon_2 & \ddots & \\ & \ddots & \ddots & t \\ & & t & \varepsilon_n \end{pmatrix} \tag{1.8}$$

When the molecule is connected to electrodes as shown in figure 1.3-B (equation 1.9) the levels are broadened.

$$H_{(mol,junction)} = \begin{pmatrix} \varepsilon_1 - \Sigma_L & t & & \\ t & \varepsilon_2 & \ddots & \\ & \ddots & \ddots & t \\ & & t & \varepsilon_n - \Sigma_R \end{pmatrix} \tag{1.9}$$

Here $\Sigma_{L,R}$ represent the self-energy matrices that account for the effect of the electrodes on the molecule. Its anti-Hermitian part is the broadening matrix $\Gamma_{L,R} = i[\Sigma_{L,R} - \Sigma_{L,R}^{\dagger}]$. Now using non-equilibrium Green's function (NEGF) formalism we can calculate the current self-consistently resulting in equation 1.10. The NEGF method is a formalism for solving the many-body Schrödinger equation of a non-equilibrium system coupled to semi-finite electrodes (For a complete description of the NEGF formalism we refer to [30]).

$$I = \frac{2e}{h} \int_{-\infty}^{\infty} [Tr(\Gamma_L G \Gamma_R G^{\dagger})(f_L - f_R)] dE \tag{1.10}$$

With $G(E) = (ES - H - \Sigma_L - \Sigma_R)^{-1}$ being the Green's function and $Tr(\Gamma_L G \Gamma_R G^{\dagger})$ being the transmission function $T(E)$ giving the Landauer-Büttiker formula found in equation 1.7. Here the $\Sigma_{L,R}$ matrices, as their name indicate, are responsible for: i) The broadening of the molecular levels as the residence time of the electrons on the level is now finite. ii) The shift of the molecular levels due to charge transfer from the leads to the molecule. In figure 1.4 we show the broadening of a level as it is more and more coupled to a surface i.e. an electrode, illustrating the effect of $\Gamma_{L,R}$.

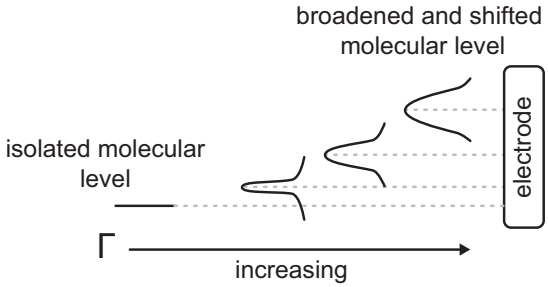

FIGURE 1.4: **Broadening of molecular levels.** Here we schematically show the effect of coupling (to the leads) on a molecular level. On the left we see a discrete level for molecule in free-space and moving to the right we see the level broadening and shifting in energy.

In chapter 4 we use a simplified single level model and we treat the discrete molecular level of a free molecule as a Lorentzian density of state when it connects to a surface [31, 32]):

$$DOS(E) = \frac{1}{2\pi} \frac{\Gamma_L + \Gamma_R}{(E - \varepsilon)^2 + ((\Gamma_L + \Gamma_R)/2)^2} \tag{1.11}$$

With $\Gamma_{L,R}$ still being the coupling between the electrodes (L,R) and the molecule, but not in matrix form anymore. In this simple model the transmission T(E) is 1 at the center of the Lorentzian (resonant tunneling), representing the HOMO or the LUMO depending on the position of the Fermi level, E_F. In the multi-level model presented above and certainly in the more evolved DFT-based calcula-

tions both the HOMO and the LUMO are taken into account, the only uncertainty is their relative position to E_F which we will discuss in chapter 6 and appendix C.

Another important ingredient in molecular charge transport, besides the coupling to the leads, is the potential profile over the junction. Indeed this can have a dramatic influence on the current-voltage characteristics. We introduce η a parameter characterizing the voltage profile within the junction. For $\eta = 0.5$ the voltage drop, V_b, over the molecule is symmetric meaning that the chemical potential μ_R is lowered by $eV_b/2$ and μ_L is increased by $eV_b/2$. In the case of $\eta = 1$ or $\eta = 0$ the voltage drop is asymmetric, meaning that the molecular level is following one of the two electrodes. So the chemical potential $\mu_{L,R}$ can be rewritten as $\mu_R = E_F - (1-\eta)eV_b$ and $\mu_L = E_F + \eta eV_b$. Resulting in an expression for the current at $T = 0$K:

$$I = \frac{2e}{\hbar}\int_{-\infty}^{\infty} T(E)(f_L - f_R)dE \tag{1.12}$$

In the experiments we present in this thesis not only the current-voltage (I(V)-curves) characteristics are studied, also the first derivative of those characteristics, the dI/dV are studied to reveal more details on the charge transport through molecules (chapter 5 and 6). In equation 1.13 we express the dI/dV for $T = 0K$ to show the influence of η on the measured dI/dV.

$$\frac{dI}{dV} = \frac{2e^2}{h}(\eta T(E_F + \eta eV) + (1-\eta)(T(E_F - (1-\eta)eV))) \tag{1.13}$$

Here we can see that for a symmetric voltage drop the I(V)-curve is antisymmetric as well as the dI/dV curve whereas for an asymmetric voltage drop and an asymmetric transmission function the resulting curves are asymmetric, this is discussed in further details in chapter 5, 6 and in appendix C.

To summarize, molecules are fascinating systems to study mesoscopic charge transport, their conductance properties can be tuned by organic chemistry. The behaviour of those molecules can be predicted by calculations at different levels of complexity (from a simple single level model to DFT-NEGF calculations). The way molecules couple with the electrodes is determinant for the conductance properties of the formed junction.

1.3 Overview of the most common experimental techniques

The principal barrier for the development of molecular electronics since the paper of Aviram and Ratner has long been the technology to connect the

molecules to an electronic circuit. A few mile-stones in science have accelerated the development of techniques to contact molecules for charge transport measurements. First, the invention in the 1980's of the scanning tunneling microscope (STM) [33] made the first conductance experiment on a single molecule possible [34]. More generally Binnig and Rohrer opened the way for a whole set of scanning probe techniques that enable the connection to nanometer-scale objects as well as their imaging. Secondly, tremendous advances have been made in the fabrication of nanometer-sized structures by electron beam lithography making molecular electronic based devices possible. Most of the common experimental techniques used nowadays are connected directly or sideways to the two above-mentioned technical advancements. Parallel to the advancement of scanning probe techniques, an other technique was developed by Moreland *et al.* enabling atomic sized contacts with high stability [35]. The mechanically controlled break junction (MCBJ) made the first measurements to a single molecular wire possible [4]. We describe here three types of methodologies to contact molecules and study their charge transport properties, they are representative for a large part of the existing techniques.

We have learned in the short history of molecular charge transport that original mistakes had to do with the lack of information available about the electrode-molecule interface. Indeed voltage-driven switching has been observed while filaments were growing from one electrode to another [6, 36]. Additionally the improper use of electromigrated break-junctions [37, 38] introduced some reasonable doubts on the obtained results (possible presence of metallic clusters in the junction) [39]. So it is of utmost importance to carefully characterize the method for contacting the molecules.

Molecules can be contacted individually (one or a few molecules connected) or as a group usually in the form of a self-assembled monolayer. Most of the measurements are performed in a so-called two-terminal junction, where the molecule is connected to the electrodes at both ends. In a three-terminal junction a third electrode is added, without actually contacting the molecule, to apply an electrical field on the molecule[37]. The third electrode is often referred to as the gate in analogy to transistors. Moreover gating is also obtained in liquid environment in so-called electrochemical gating devices[23, 40]. Experiments on molecular charge transport are often executed at liquid Helium temperatures and high vacuum conditions for an optimal stability [41]. Nevertheless impressive results have also been reported at ambient conditions [42] or even in liquid environment[43], indeed as we have seen above the quantum properties of molecules are still dominant at room temperature due to their small size.

1.3.1 BREAK-JUNCTION EXPERIMENTS

Under the definition 'break-junctions' we can distinguish three types of junctions: the mechanically controlled break-junction (MCBJ)[10], the electromigrated break-junction [37] that we will discuss in a separated section and the scanning tunneling microscope break-junction (STM-BJ) [44]. The common feature of these techniques is the breaking of a metalic wire into a nanometer-sized junction. The control on the gap size is different for each technique. Here we discuss the MCBJ and the STM-BJ as they allow for a continuous and controlled breaking and making of the junction, in that sense electromigrated junctions are different as the gap can only be formed once.

MCBJs are made of a constricted metallic wire (notched wire or lithographically defined) that is placed on a flexible substrate. The bending of the substrate induces an elongation of the wire at the constriction which eventually breaks. This technique permits a control of the electrode separation on sub-nanometer scale. Moreover, if the breaking is done in high-vacuum, the contacts are atomically clean. The wire can be reformed and broken at will [10, 14, 41, 45].

The same breaking-forming cycles can be obtained with the STM-BJ technique. Unlike for the MCBJ, here we start with two separated electrodes: the conducting substrate and the tip both made of the same metal. By pushing the tip gently in the substrate a wire can be formed and broken again [17, 44, 46, 47]. The STM-BJ does not allow for the same clean conditions and stability but makes it possible to obtain topological information on the substrate.

So the common feature of these two techniques is to be able to repeatedly form and break nanometer-sized junctions. When this is done in the presence of molecules, molecular junctions are formed and broken continuously allowing for a massive, statistically sound, dataset [45, 48]. In figure 1.5 we show the characteristic steps of the measurements on a molecular junction with a break-junction setup. With this technique over 10000 molecular junctions can be measured in one experiment. The molecules can bind to the electrodes in different configurations resulting in different conductance values [49], representing the measured conductances in an histogram shows the variation around the average conductance value.

1.3.2 THREE-TERMINAL ELECTROMIGRATION EXPERIMENTS

Electromigrated break-junctions present the same advantages as the above mentioned MCBJ in terms of contaminations, indeed the wire can be broken in vacuum resulting in atomically clean electrodes. Here the formation of a junction in a metallic wire is due to the direct migration of atoms by momentum transfer from the electrons at high current densities[50]. Hence when the wire

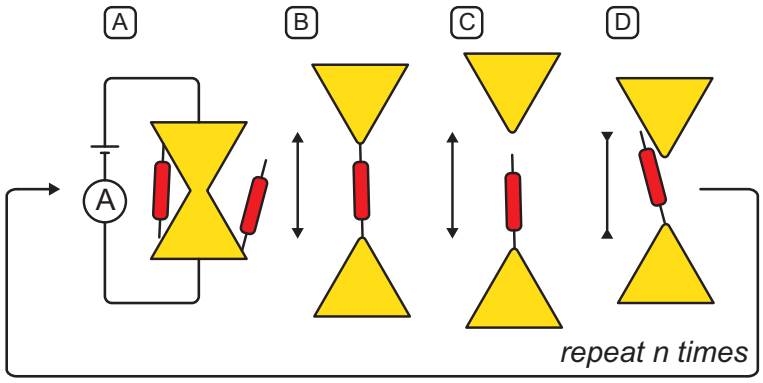

FIGURE 1.5: **Typical break junction experiment performed on a MCBJ or STM-BJ setup. A** Both electrodes are still in contact with each other. **B** The molecule bridges the junction. **C** The junction breaks, the contact is lost with molecule. **D** The junction is closing again.

is broken it is not possible to close the junction again as it is done with MCBJ's for example. A careful methodology has been developed to avoid the formation of metallic grains in the junction, which could be confused with molecules in the transport measurements[37]. The main advantage of electromigrated junctions is the possibility to have a gate electrode close to the inserted molecules resulting in an optimal molecule-gate coupling (typically 0.1 [51, 52]). In figure 1.6 we show a schematic view of three-terminal electromigrated junction. Although electromigration break-junctions have a low yield of working devices, they permit the observation of numerous transport phenomena like Kondo effect and Coulomb blockade as it is one of the few techniques making gated measurements possible[51, 53]. Recently Martin *et al.* succeeded in building a promissing MCBJ with a gate electrode [54, 55]. Although in this technique the gate coupling is lower than in electromigrated junctions it combines the robust statistical analysis typical of MCBJ's to a three-terminal junction.

1.3.3 LARGE AREA MOLECULAR JUNCTIONS

A measurement technique with a different philosophy, the large area molecular junction (LAMJ), is described here. These devices are focused on contacting a large area of self-assembled monolayers of molecules (ranging from 10 to 100

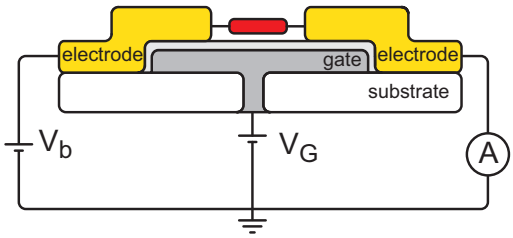

FIGURE 1.6: **Schematic view of an ideal three-terminal electromigrated break-junction.** The gate electrode just below the source and drain electrodes is covered by a thin insulating oxide layer.

μm in diameter) [56, 57]. In LAMJ devices the SAM is sandwiched between the two electrodes, the bottom electrode is used to grow the SAM and the top electrode is evaporated on top of the formed SAM. To prevent damage to the SAM and the formation of metallic filaments during measurements an interstitial layer of conducting polymer (PEDOT:PSS) is used. This fabrication process offers the possibility for up-scaling, indeed wafers with over 20000 junctions have been made with more than 200 junctions connected in series [58].

To wrap up, we discussed three different techniques for studying charge transport in molecular junctions. Important criteria for charge transport measurements are : i) the possibility of harvesting enough data to be able to conduct a statistically sound analysis. ii) the possibility to vary other parameters like the applied voltage bias, a gate voltage or optical probes.

REFERENCES

[1] B. Mann, *Tunneling through Fatty Acid Salt Monolayers*, Journal of applied physics **42**, 4398 (1971).

[2] A. Aviram and M. Ratner, *Molecular Rectifiers*, Chemical Physics Letters **29**, 277 (1974).

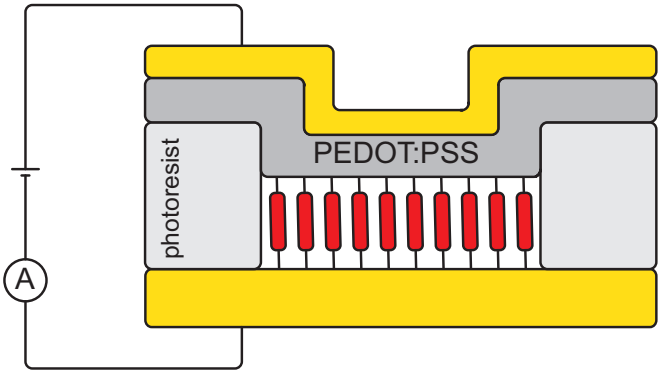

FIGURE 1.7: **Schematic view of a large area molecular junction.** .

[3] C. Joachim, J. Gimzewski, R. Schlittler, and C. Chavy, *Electronic transparency of a single c-60 molecule*, Physical Review Letters **74**, 2102 (1995).

[4] M. Reed, C. Zhou, C. Muller, T. Burgin, and J. Tour, *Conductance of a molecular junction*, Science **278**, 252 (1997).

[5] R. Service, *Molecules get wired*, Science **294**, 2442 (2001).

[6] R. Service, *Molecular electronics - Next-generation technology hits an early midlife crisis*, Science **302**, 556 (2003).

[7] R. Service, *Molecular electronics - Nanodevices make fresh strides toward reality*, Science **302**, 1310 (2003).

[8] C. Kittel, *Introduction to Solid State Physics* (Wiley, 1995).

[9] B. Vanwees, H. Van Houten, C. Beenakker, J. Williamson, L. Kouwenhoven, D. Van der Marel, and C. Foxon, *Quantized conductance of point contacts in a two-dimensional electron-gas*, Physical Review Letters **60**, 848 (1988).

[10] N. Agrait, A. L. Yeyati, and J. M. van Ruitenbeek, *Quantum properties of atomic-sized conductors*, Physics Reports-Review Section Of Physics Letters **377**, 81 (2003).

[11] R. Landauer, *Spatial variation of currents and fields due to localized scatterers in metallic conduction*, Ibm Journal Of Research And Development **1**, 223 (1957).

[12] M. Buttiker, *Scattering-theory of current and intensity noise correlations in conductors and wave guides*, Physical Review B **46**, 12485 (1992).

[13] O. Tal, M. Krieger, B. Leerink, and J. M. van Ruitenbeek, *Electron-vibration interaction in single-molecule junctions: From contact to tunneling regimes*, Physical Review Letters **100**, 196804 (2008).

[14] R. H. M. Smit, Y. Noat, C. Untiedt, N. D. Lang, M. C. van Hemert, and J. M. van Ruitenbeek, *Measurement of the conductance of a hydrogen molecule*, Nature **419**, 906 (2002).

[15] H. B. Akkerman and B. de Boer, *Electrical conduction through single molecules and self-assembled monolayers*, Journal Of Physics-Condensed Matter **20** (2008).

[16] B. F. C. Choi, S.H.; Kim, *Electrical Resistance of Long Conjugated Molecular Wires*, Science **320**, 1482 (2008).

[17] L. Venkataraman, J. E. Klare, I. W. Tam, C. Nuckolls, M. S. Hybertsen, and M. L. Steigerwald, *Single-molecule circuits with well-defined molecular conductance*, Nano Letters **6**, 458 (2006).

[18] R. Huber, M. T. González, S. Wu, M. Langer, S. Grunder, V. Horhoiu, M. Mayor, M. R. Bryce, C. Wang, R. Jitchati, et al., *Electrical Conductance of Conjugated Oligomers at the Single Molecule Level*, Journal of the American Chemical Society **130**, 1080 (2008).

[19] S. J. van der Molen and P. Liljeroth, *Charge transport through molecular switches*, Journal Of Physics-Condensed Matter **22**, 133001 (2010).

[20] S. J. van der Molen, J. H. Liao, T. Kudernac, J. S. Agustsson, L. Bernard, M. Calame, B. J. van Wees, B. L. Feringa, and C. Schönenberger, *Light-Controlled Conductance Switching of Ordered Metal-Molecule-Metal Devices*, Nano Letters **9**, 76 (2009).

[21] E. H. van Dijk, D. J. T. Myles, M. H. van der Veen, and J. C. Hummelen, *Synthesis and Properties of an Anthraquinone-Based Redox Switch for Molecular Electronics*, Org. Lett. **8**, 2333 (2006).

[22] R. Chandrasekar, F. Schramm, O. Fuhr, and M. Ruben, *An Iron(II) spin-transition compound with thiol anchoring groups*, European Journal Of Inorganic Chemistry pp. 2649–2653 (2008).

[23] X. Y. Xiao, L. A. Nagahara, A. M. Rawlett, and N. J. Tao, *Electrochemical gate-controlled conductance of single oligo(phenylene ethynylene)s*, Journal Of The American Chemical Society **127**, 9235 (2005).

[24] J. Love, L. Estroff, J. Kriebel, R. Nuzzo, and G. Whitesides, *Self-assembled monolayers of thiolates on metals as a form of nanotechnology*, Chemical Reviews **105**, 1103 (2005).

[25] L. Patrone, S. Palacin, J. Charlier, F. Armand, J. Bourgoin, H. Tang, and S. Gauthier, *Evidence of the key role of metal-molecule bonding in metal-molecule-metal transport experiments*, Physical Review Letters **91**, 96802 (2003).

[26] B. Xu and N. Tao, *Measurement of single-molecule resistance by repeated formation of molecular junctions*, Science **301**, 1221 (2003).

[27] F. Chen, X. Li, J. Hihath, Z. Huang, and N. Tao, *Effect of anchoring groups on single-molecule conductance: Comparative study of thiol-, amine-, and carboxylic-acid-terminated molecules*, Journal Of The American Chemical Society **128**, 15874 (2006).

[28] Y. S. Park, A. C. Whalley, M. Kamenetska, M. L. Steigerwald, M. S. Hybertsen, C. Nuckolls, and L. Venkataraman, *Contact chemistry and single-molecule conductance: A comparison of phosphines, methyl sulfides, and amines*, Journal Of The American Chemical Society **129**, 15768 (2007).

[29] Z. L. Cheng, R. Skouta, H. Vazquez, J. R. Widawsky, S. Schneebeli, W. Chen, M. S. Hybertsen, R. Breslow, and L. Venkataraman, *In situ formation of highly conducting covalent Au-C contacts for single-molecule junctions*, Nature Nanotechnology **6**, 353 (2011).

[30] S. Datta, *Electrical resistance: an atomistic view*, Nanotechnology **15**, S433 (2004).

[31] M. P. Samanta, W. Tian, S. Datta, J. I. Henderson, and C. P. Kubiak, *Electronic conduction through organic molecules*, Physical Review B **53**, R7626 (1996).

[32] J. A. Malen, P. Doak, K. Baheti, T. D. Tilley, R. A. Segalman, and A. Majumdar, *Identifying the Length Dependence of Orbital Alignment and Contact Coupling in Molecular Heterojunctions*, Nano Letters **9**, 1164 (2009).

[33] G. Binnig, H. Rohrer, C. Gerber, and E. Weibel, *Surface Studies by Scanning Tunneling Microscopy*, Physical Review Letters **49**, 57 (1982).

[34] A. Aviram, C. Joachim, and M. Pomerantz, *Evidence of switching and rectification by a single molecule effected with a scanning tunneling microscope*, Chemical Physics Letters **146**, 490 (1988).

[35] J. Moreland and J. Ekin, *Electron tunneling experiments using NbSn break junctions*, Journal of Applied Physics **58**, 3888 (1985).

[36] J. E. Green, J. W. Choi, A. Boukai, Y. Bunimovich, E. Johnston-Halperin, E. DeIonno, Y. Luo, B. A. Sheriff, K. Xu, Y. S. Shin, et al., *A 160-kilobit molecular electronic memory patterned at 10(11) bits per square centimetre*, Nature **445**, 414 (2007).

[37] H. S. J. van der Zant, Y. V. Kervennic, M. Poot, K. O'Neill, Z. de Groot, J. M. Thijssen, H. B. Heersche, N. Stuhr-Hansen, T. Bjornholm, D. Vanmaekelbergh, et al., *Molecular three-terminal devices: fabrication and measurements*, Faraday Discussions **131**, 347 (2006).

[38] M. Trouwborst, S. van der Molen, and B. van Wees, *The role of Joule heating in the formation of nanogaps by electromigration*, Journal Of Applied Physics **99** (2006).

[39] H. Song, Y. Kim, Y. H. Jang, H. Jeong, M. A. Reed, and T. Lee, *Observation of molecular orbital gating*, Nature **462**, 1039 (2009).

[40] Z. Li, Y. Liu, S. F. L. Mertens, I. V. Pobelov, and T. Wandlowski, *From Redox Gating to Quantized Charging*, Journal Of The American Chemical Society **132**, 8187 (2010).

[41] C. A. Martin, D. Ding, H. S. J. van der Zant, and J. M. van Ruitenbeek, *Lithographic mechanical break junctions for single-molecule measurements in vacuum: possibilities and limitations*, New Journal of Physics **10**, 065008 (2008).

[42] D. J. Wold and C. D. Frisbie, *Fabrication and characterization of metal-molecule-metal junctions by conducting probe atomic force microscopy*, J. Am. Chem. Soc. **123**, 5549 (2001).

[43] L. Venkataraman, J. E. Klare, C. Nuckolls, M. S. Hybertsen, and M. L. Steigerwald, *Dependence of single-molecule junction conductance on molecular conformation*, Nature **442**, 904 (2006).

[44] X. Y. Xiao, B. Q. Xu, and N. J. Tao, *Measurement of single molecule conductance: Benzenedithiol and benzenedimethanethiol*, Nano Letters **4**, 267 (2004).

[45] E. H. Huisman, M. L. Trouwborst, F. L. Bakker, B. de Boer, B. J. van Wees, and S. J. van der Molen, *Stabilizing Single Atom Contacts by Molecular Bridge Formation*, Nano Letters **8**, 3381 (2008).

[46] A. Mishchenko, D. Vonlanthen, V. Meded, M. Burkle, C. Li, I. V. Pobelov, A. Bagrets, J. K. Viljas, F. Pauly, F. Evers, et al., *Influence of Conformation on Conductance of Biphenyl-Dithiol Single-Molecule Contacts*, Nano Letters **10**, 156 (2010).

[47] C. Li, I. Pobelov, T. Wandlowski, A. Bagrets, A. Arnold, and F. Evers, *Charge transport in single Au/alkanedithiol/Au junctions: coordination geometries and conformational degrees of freedom.*, Journal of the American Chemical Society **130**, 318 (2008).

[48] M. T. Gonzalez, S. M. Wu, R. Huber, S. J. van der Molen, C. Schonenberger, and M. Calame, *Electrical conductance of molecular junctions by a robust statistical analysis*, Nano Letters **6**, 2238 (2006).

[49] X. Li, J. He, J. Hihath, B. Xu, S. M. Lindsay, and N. Tao, *Conductance of Single Alkanedithiols: Conduction Mechanism and Effect of Molecule-Electrode Contacts*, Journal of the American Chemical Society **128**, 2135 (2006).

[50] H. Park, A. Lim, A. Alivisatos, J. Park, and P. McEuen, *Fabrication of metallic electrodes with nanometer separation by electromigration*, Applied Physics Letters **75**, 301 (1999).

[51] E. A. Osorio, K. O'Neill, M. Wegewijs, N. Stuhr-Hansen, J. Paaske, T. Bjornholm, and H. S. J. van der Zant, *Electronic excitations of a single molecule contacted in a three-terminal configuration*, Nano Letters **7**, 3336 (2007).

[52] M. Poot, E. Osorio, K. O'Neill, J. M. Thijssen, D. Vanmaekelbergh, C. A. van Walree, L. W. Jenneskens, and H. S. J. van der Zant, *Temperature Dependence of Three-Terminal Molecular Junctions with Sulfur End-Functionalized Tercyclohexylidenes*, Nano Letters **6**, 1031 (2006).

[53] E. A. Osorio, K. Moth-Poulsen, H. S. J. van der Zant, J. Paaske, P. Hedegard, K. Flensberg, J. Bendix, and T. Bjornholm, *Electrical Manipulation of Spin States in a Single Electrostatically Gated Transition-Metal Complex*, Nano Letters **10**, 105 (2010).

[54] C. A. Martin, J. M. van Ruitenbeek, and H. S. J. van der Zant, *Sandwich-type gated mechanical break junctions*, Nanotechnology **21** (2010).

[55] C. A. Martin, R. H. M. Smit, H. S. J. van der Zant, and J. M. van Ruitenbeek, *A Nanoelectromechanical Single-Atom Switch*, Nano Letters **9**, 2940 (2009).

[56] H. B. Akkerman, R. C. G. Naber, B. Jongbloed, P. A. van Hal, P. W. M. Blom, D. M. de Leeuw, and B. de Boer, *Electron tunneling through alkanedithiol self-assembled monolayers in large-area molecular junctions*, Proceedings Of The National Academy Of Sciences Of The United States Of America **104**, 11161 (2007).

[57] H. B. Akkerman, P. W. M. Blom, D. M. de Leeuw, and B. de Boer, *Towards molecular electronics with large-area molecular junctions*, Nature **441**, 69 (2006).

[58] P. A. Van Hal, E. C. P. Smits, T. C. T. Geuns, H. B. Akkerman, B. C. De Brito, S. Perissinotto, G. Lanzani, A. J. Kronemeijer, V. Geskin, J. Cornil, et al., *Upscaling, integration and electrical characterization of molecular junctions*, Nature Nanotechnology **3**, 749 (2008).

2

2D NANOPARTICLE NETWORKS FOR MOLECULAR ELECTRONICS

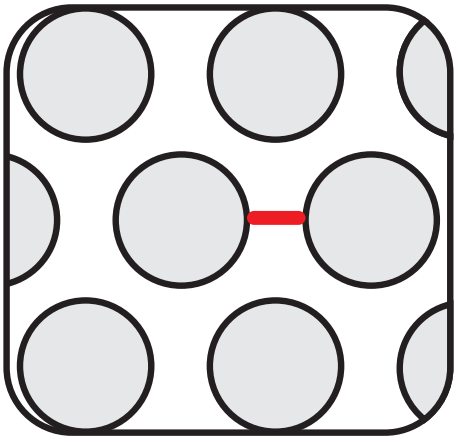

2.1 A NEW APPROACH FOR MOLECULAR CHARGE TRANSPORT

The vast arsenal of techniques to connect molecules to electrodes can be divided into two main groups based on the amount of molecules contacted. At one side we have single or very few molecules that are probed. These single molecule experiments are usually conducted at low temperatures to guarantee junction stability[1–4]. In this way a maximum of information can be extracted from the transport measurements (e.g. by point contact spectroscopy, inelastic electron tunnel spectroscopy). On the other side of the spectrum, large ensembles of molecules can also be probed simultaneously [5, 6]. These techniques are less demanding on signal-to-noise ratio and are usually stable enough to be used at room temperature. The conductances measured for such large ensembles of molecules are averaged values in contrast to single-molecule measurements.

Here we present a technique bridging these two groups of molecular electronics techniques. For this we probe a two dimensional (2D) network of single (or few) molecular junctions. So now the measured resistance is an average in space over all the junctions probed. This in contrast with single molecular experiments that require multiple measurements i.e. averaging in time, to express a statistically sound resistance value. For this approach we make use of a network of gold nanoparticles (NP's), where the NP's act as miniature electrodes to contact the molecules (see figure 2.1)[7]. The 2D array is an ordered trian-

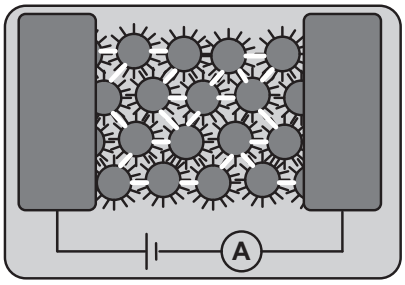

FIGURE 2.1: **Schematic view of a 2D nanoparticle array.** Nanoparticles (NP's) with a diameter of approximately 10 nm are self-assembled into a triangular lattice. The black rods surrounding the nanoparticles represent the thio-alkane ligands and the white rods bridging the NP's represent the inserted molecules. The array is contacted with electrodes to a voltage source and an amperemeter.

gular lattice of nanoparticles which is obtained by a self-assembly process[8]. Interfacing this network by larger electrodes is a straightforward step, mak-

ing this technique a versatile and easy method for contacting nanometer sized objects like molecules. Making use of a second self-assembly step one can insert the molecules of interest between the nanoparticles, creating in this way a metal-molecule-metal junction. Besides being stable at room temperature, this technique makes the studied molecules addressable by optical means (UV-Vis, IR, Raman) which remains a challenge for other techniques[9–11].

In the ideal case, we can relate the measured conductance of a 2D nanoparticle network to the conductance of a single particle-molecule-particle junction. To illustrate this we show in figure 2.2 a repetitive unit, as a building block of an ideal 2D NP's network. Hence we show how to relate the resistance of a single junction, R_j, to the measured sheet resistance $R_\square$. If we apply a bias voltage U to the building block, the total current I_{tot} can expressed as: $I_{tot} = \frac{3U}{R}$. Compensating for the size of the building block to get the sheet resistance we find: $R_\square = \frac{1}{\sqrt{3}} R_j \approx 0.6 R_j$.

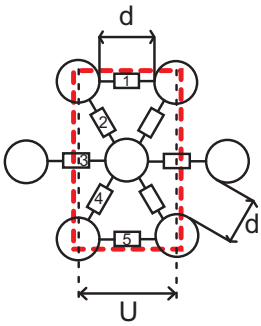

FIGURE 2.2: **Schematic view of a repeating unit in a idealized 2D nanoparticle network.** d is the inter-particle distance. Junctions between two NP's are modeled by resistors, we assume the resistance R equal for all the junctions. U is the applied bias on the building block.

Moreover a second advantage of 2D NP's networks is that using UV-vis spectroscopy we follow the surface plasmon resonance (SPR) of a 2D NP's network in order to confirm the insertion of the molecules into the array.

In this chapter we present a method for the fabrication of 2D nanoparticle networks. We also elaborate on the characterization of such networks. This is followed by experimental results on several organic molecules. Furthermore we investigate the possibility of using a back-gate for such devices. Finally we have a discussion on the pros and cons of this technique.

2.2 NANOPARTICLE NETWORKS

2.2.1 SYNTHESIS

First the nanoparticles are synthesized following the method of Slot and Geuze [12] that allows for the tuning of the diameter of the nanoparticles (NPs) (see appendix A). The size of the NP's is chosen to be not too small in order to avoid charging effects (Coulomb blockade) and level quantization and not too big in order to only connect to a few molecules. The NP's are formed from the reduction of gold chloride by two reducing agents, tannic acid and citric acid. The tannic acid reacts fast with the gold chloride and forms nucleation sites. Indeed the amount of tannic acid regulates the number of nucleation sites and hence the final size of the NP's. The reaction with citric acid is slower and is necessary for the growth of the NP's. After this first synthetic step the NP's are charge-stabilized in water i.e. as we can see in figure 2.3, the nanoparticles are surrounded by anions that prevent aggregation. For further use in the self-assembly process the NP's are transfered to an intermediary solvent, ethanol, where they are coated with alkanethiols. As a last step the NP's coated with alkanes are transfered to a chloroform solution. At the end the NP's are surrounded by alkanethiols in a solution of chloroform, they are not charge stabilized anymore but stabilized by steric repulsion of the alkane chains. A schematic view of the nanoparticles is shown in figure 2.3.

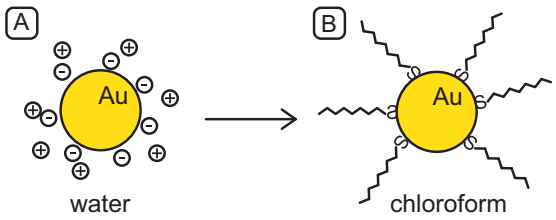

FIGURE 2.3: **Evolution of gold nanoparticles from water to chloroform. A** the nanoparticles are charge stabilized in water i.e. the repulsion of the charges surrounding the NP prevent the NP's of coalescing. **B** the NP are surrounded by thio-alkanes in chloroform that take over the repulsive action of the charges.

2.2.2 SELF-ASSEMBLY OF A TWO DIMENSIONAL NETWORK

We obtain highly-ordered networks by letting the NP's self-assemble on a water surface. The self-assembly is governed by i) the shape of the water surface ii)

the type of solvent used and iii) the characteristics of the NP's like their size and type of ligands.

Experimental details

We first give here a description of the method to form 2D nanoparticle networks. As we have seen above the NP's are dissolved in chloroform which is a volatile solvent. Additionally we make use of a curved water surface in a Teflon container (see figure 2.4). These two characteristics make it possible to self-assemble the nanoparticles into an ordered 2D network. Subsequently we spread a thin layer of colloids in chloroform on the water layer, as the chloroform does not mix with water. Immediately the chloroform starts to evaporate finally leaving the alkane coated nanoparticles on the air-water interface. The alkane ligands are responsible for the hydrophobic character of the NP's. As the chloroform evaporates a network starts to grow in the center of the ring resulting in a complete monolayer at the end. A nice example of a network is shown in figure 2.5 where the characteristic triangular lattice is clearly recognizable.

Mechanism of network formation

In this section we describe the assembly mechanism of the nanoparticles into a well ordered two-dimensional network. It is remarkable that following the above experimental protocol a well ordered network is obtained. Indeed most colloidal suspension drying experiments end up in the so called coffee-strain patterns where all the particles are concentrated at the border of the drying droplet[13]. The mechanism we describe is quite similar to the mechanism presented by Bigioni *et al.* but present some differences as we will see [14].

The formation of a long range ordered network depends on two parameters. First, on the flux of the drying front that should be fast enough that NP's impinge on the surface. Second, on the particle-interface interaction that is important for the nucleation and growth of NP islands on the surface. In brief the solvent evaporates at such a speed that NP's are impinging on the air-solvent surface due to a finite nanoparticle-interface interaction; the particles diffuse on the interface and join an existing island (nucleate with other NP's if no island is present) or diffuse back to the solution. In such fashion the islands grow to finally form a complete network. The flux of the drying front can be tuned mostly by choosing the appropriate solvent, whereas the nanoparticle-interface interaction is dependent on the particle size and the type of ligands. In Bigioni's work they observe a drying droplet of NP's in solution, in our case the experimental method is slightly different as we have a droplet of colloidal solution drying on a curved water surface. Although the basic mechanism of

self-assembly is probably the same, the curves water surface underneath is responsible for a convection flux of solvent and NP's towards the center of the droplet. Indeed as the evaporating solvent layer is the thinnest in the center of the teflon ring, a convective flow of solvent and thus NP's is directed towards the center of the ring. In figure 2.4 we show a schematic view of the self-assembly process.

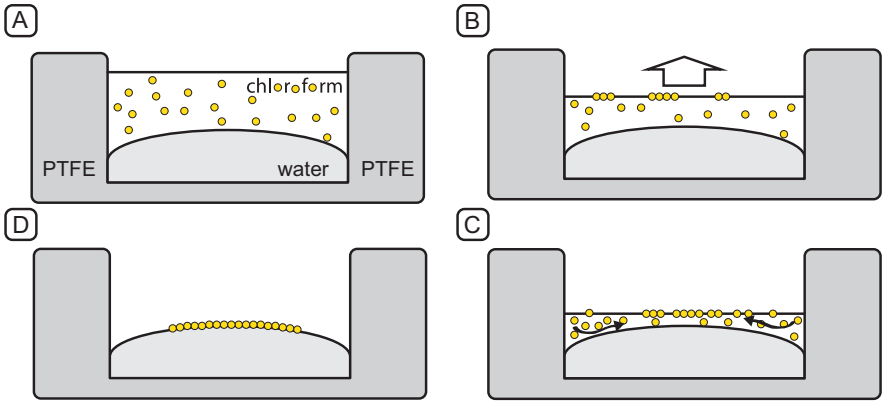

FIGURE 2.4: **Schematic view of the nanoparticle self-assembly process.** We depict a cross section of the Teflon container filled with water. **A** The solution of NP's in chloroform is pipetted on the curved water surface. **B** The chloroform is evaporating impinging the NP's on the chloroform surface. **C** A network starts to form in the center of the container as the chloroform and the NP's are driven by convection towards the center. **D** All the chloroform is evaporated and the NP network formed is floating on the water surface.

With this technique we manage to produce networks that are highly ordered on a scale of hundreds of nanometers i.e. islands with the same orientation. In figure 2.6 we show such network where we can distinguish the different orientations of the islands. However, networks with more defects are regularly encountered too, such as shown in figure 2.7.

To improve the quality of our networks i.e. to increase the long range ordering of the NP's several steps can be taken. First of all it is important to standardize the experimental conditions for the self-assembly. The size of the teflon cavities is kept fixed allowing for a constant water surface curvature. External factors like temperature and humidity are monitored showing a decrease in successful highly ordered networks with high humidity.

Second, an important factor for high quality arrays is the size distribution

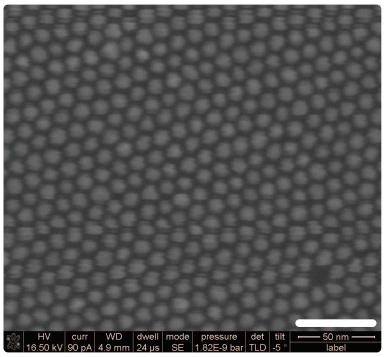

FIGURE 2.5: **SEM picture of a 2D network.** Here we focused on a highly ordered part of the array showing a single orientation. The scale bar is 50 nm.

of the NP's, indeed a narrow size distribution improves the ordering of the NP's. Therefore the synthesis steps is optimized leading to nanoparticles with a diameter of 10 ± 1 nm.

Third, the type of solvent used is determining the rate of evaporation. We use chloroform in all our experiments because of its high volatility. As shown in figure 2.7 we also obtain defect rich networks showing typical patterns for late stage drying mediated assembly [15], probably induced by a too high evaporation rate associated with chloroform. To get rid of these defects we investigate the possible use of other solvents. We use toluene and a mixtures of toluene and chloroform to slow down the evaporation. Unfortunately no significant improvement is noticed for toluene/chloroform mixtures, moreover the octanethiol caped NP's loose their stability in toluene and aggregate already in solution.

Finally, the ratio of the nanoparticle diameter and the alkanethiol length is an important factor influencing the particle-interface interaction (and the particle-particle interaction). This ratio can be tuned by modifying the NP's diameter (ϕ_{NP}) or the length of the ligands (l_{ligand}). If the ratio $\phi_{NP}/l_{ligands}$ is too big (hexanethiol for 10 nm nanoparticles), the repulsive force of the alkane chains does not counter the van der Waals forces and the NP's aggregate[16–18]. Bigioni *et al.* showed that for lower ratios (dodecanethiol for 5 nm nanoparticles) the formed networks present μm range ordering [14]. In our case we are limited by two factors: i) the interparticle distance related to the length of the ligands should match the length of the molecules we want to probe and ii) the

size of the NP's should not be too small (to avoid charging effects) and not too big (to avoid contacting too many molecules).

The optimum we found for our purpose is a network formed from NP's of 10 nm in diameter coated with octanethiols in a chloroform solution. Moreover we can decrease the size of the gap between the electrodes contacting the network (from 20 μm down to a hundreds of nm). Indeed this will maximize the likelihood of contacting a piece of network consisting of only one 'crystal' orientation, making the network closer to ideal.

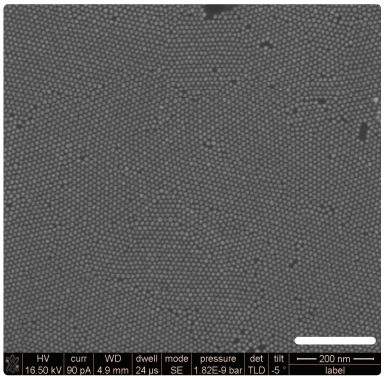

FIGURE 2.6: **SEM picture of a network.**The scale bar is 200 nm, a larger part of the network is shown here compared to figure 2.5. Here we can distinguish different orientations of the well ordered network as well as a few minor defects.

2.2.3 FROM SELF-ASSEMBLY TO WORKING DEVICES

Once we have a self-assembled network floating on the curved water surface we have to transfer it to a substrate in order to incorporate it in a working device. We make use of soft lithography patterned stamps to pick up the network from the water surface. Those stamps are made of polydimethylsyloxane (PDMS) and are molded on a lithographically patterned substrate[19]. So virtually any pattern can be designed to transfer the networks on a surface. As a substrate, two different materials are used. For charge transport measurements we use doped Si/SiO_2 substrates (250 nm oxide). For optical measurements we use quartz substrates because of their UV-transparency. Both substrates are similar at the interface with the network. Indeed in both cases the network is in contact with a SiO_2 layer. To summarize the transfer process, the hydrophobic nanoparticle network is picked up from the water surface as it has a larger

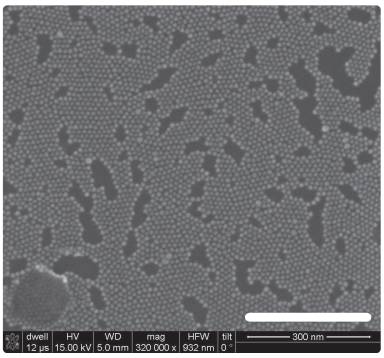

FIGURE 2.7: **SEM picture of a network with some defects.** the scale bar is 300 nm. Here we show a network where the ordered islands are smaller compared to figure 2.6. This higher level of disorder results in larger regions without Nps.

interaction with the PDMS surface and finally has a even larger interaction with the used substrates. We choose to pattern lines (20μm wide) on the PDMS stamps resulting in printed lines of nanoparticle network. Once the network is printed on the substrate we still need to make contacts to interface the network with the measurement set-up. Hence, using a TEM grid as a shadow mask we evaporate gold contacts on the printed lines[7]. [1] This results in a substrate with numerous ($\approx$ 250) nanoparticle network devices as can be seen on figure 2.8. During the process of evaporating a chromium attachment layer and a gold layer as contacts, the substrate is cooled to prevent too much heating of the network resulting in the aggregation of the nanoparticles.

2.2.4 CHARGE TRANSPORT MEASUREMENTS

Charge transport measurements are done on the devices prepared as described above. The electrodes are contacted by needles on a probe station mounted in a Faraday cage. We apply a voltage to the junction and measure the corresponding current in a two terminal fashion. The small currents obtained ($\approx$ nA) are converted to a voltage by a variable gain amplifier (Femto DLPCA-200). The measurements are controlled by a Labview routine and the computer is interfaced with our measurements by a National Instrument DAQ-mx card. In figure

[1] Lithographic techniques are not used to create electrodes on top of a network in order to prevent i) coalescence of the NPs due to the heat treatment ii) contamination of the network with photoresist molecules.

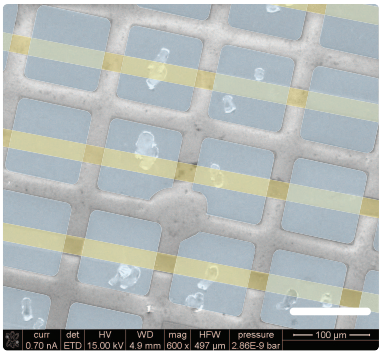

FIGURE 2.8: **SEM picture of a stamped 2D network with electrodes.** We highlighted in false colours the stamped network lines (yellow) and the corresponding electrodes (blue). Here we recognize the stamped network lines (20 μm width) covered by square gold electrodes (100 x 100 μm). On the surface of the electrode one can see the scratches made by the probe station to contact the networks. The scale bar is 100 μm.

2.9 we present a schematic view of our measurement set-up. In figure 2.9-B we show a typical voltage-current characteristic for a junction formed solely of gold nanoparticles coated with octanethiols. The I(V) curve is linear on the whole voltage range, up to 10 V. This is due to the fact that the voltage drop on a single NP-NP junction is in the range of a few mV as the network is composed of a large number ($\approx$ 1000 junctions) of NP-NP junctions in series. Nevertheless the precise voltage drop experienced for each junction will vary. The resistance of the array is determined by the slope of the I(V) curve. Therefore the measured resistance is an average of the zero bias resistances of all the active junctions in the array as explained above. A stable resistance in time is needed for the intended experiments, indeed our aim is to compare the resistance of the network before and after the insertion of the molecules of interest. First of all we monitor the conductance stability in time of our devices, the results for one sample are presented in figure 2.10. What is striking is the change in resistance in the first two hours after evapoation of the electrodes ($5 \cdot 10^4$ s), indeed the resistance is dropping a factor 10 in that time. What we also notice is that the resistance stabilizes after the drop and remains stable for a long time (measured for two days, not shown in the figure). The opposite resistance change is found when placing the sample in a low vacuum chamber (typically a few mbar) as we can see in figure 2.11. Here we measured the resistance while pumping down the chamber. This resistance reaches a maximum value after a few min-

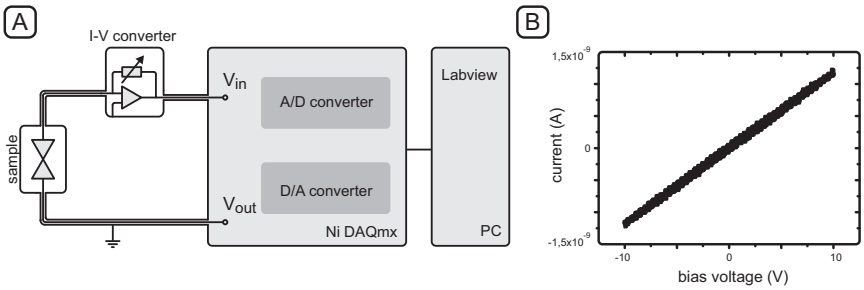

FIGURE 2.9: **Charge transport measurements setup. A** Schematic view of the measurement setup. **B** The graph shows the current-voltage characteristics of a network consisting solely of naoparticles covered by octanethiol ligands. The voltage applied over the whole network is 10 V, resulting in a bias of only a few mV for each junction.

utes in vacuum and remains constant for at least two days. It is of course of major importance to be able to disentangle the variations of the resistance in time and the effect of molecular exchange on the network's resistance.

The observed resistance change for the samples after the evaporation of the electrodes (figure 2.10) and for the samples in vacuum (figure 2.11) present two different time scales. The slower change in resistance for the samples out of the evaporator (10^{-6} mbar) is probably due to some rearrangements in the network and the influence of the ambient air. The more rapid changes in resistance as observed in the low vacuum experiments are, we guess, due to the influence of the ambient air. The most probable factor having influence on the resistance is the absorption/desorption of water molecules on the network. Indeed the presence of water molecules, that have a high polarizability, can disturb the electrostatic environment of the NP-NP junctions. The dipole moment of the water molecules can lower the tunnel barrier resulting in a lower resistance. When placed in vacuum the water is being pumped out of the network. In the low vacuum range we are using, not all the water can be pumped away. The initial resistance is therefore not fully recovered. However when the devices are put back in a high vacuum chamber, the original resistance is found back. In general, all the resistance measurements are performed after at least two hours or in vacuum in order to have a stable resistance value.

2.2.5 SURFACE PLASMON RESONANCE

We also study the 2D nanoparticle arrays by following their optical behaviour. Indeed such small metallic particles have particular optical properties. When

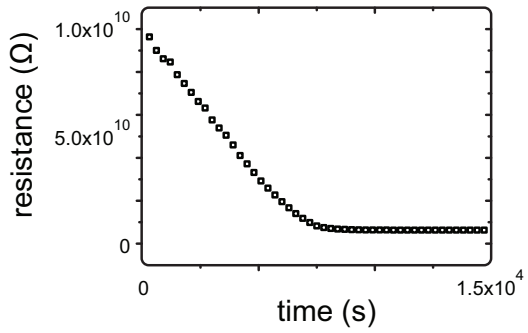

FIGURE 2.10: **Resistance recorded as a function of time in air.** The resistance of a network consisting solely of nanoparticles covered by octanethiols is recorded over night having the sample in ambient conditions. The measurement starts immediately after the electrode-evaporation step.

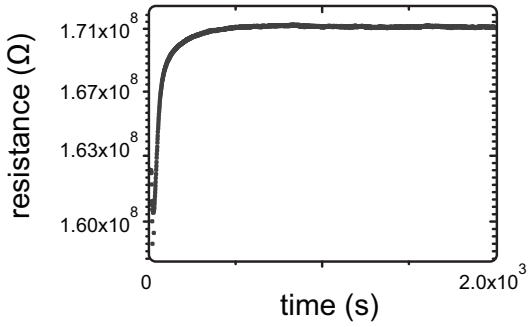

FIGURE 2.11: **Resistance recorded as a function of time in low vacuum.**The resistance of a network consisting solely of nanoparticles covered by octanethiols is recorded over night having the sample in a vacuum chamber connected to a membrane pump. The end pressure achieved by such a pump is typically in the order of a few tenth of mbar.

light interacts with the nanoparticles this gives rise to surface plasmons, a collective excitation of the free electrons. The electrons are oscillating with respect to the positive ion background creating an oscillating surface polarization. This results in a maximum of optical absorption. The strength of the surface plasmon resonance (SPR) of nanoparticles is dependent on both the internal properties of the particle and the properties of the surrounding. In figure 2.12 we depict schematically the interaction of light and a nanoparticle leading to resonances.

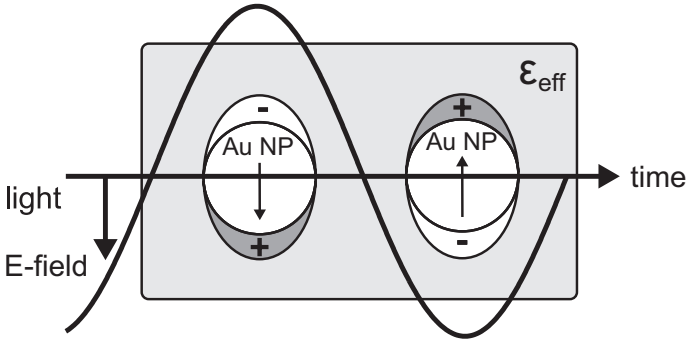

FIGURE 2.12: **Schematic view of light interacting with nanoparticles resulting in the surface plasmon resonance.** Here we only take into account the electric field component of light. We show the collective movement of electrons in the nanoparticle inducing a surface polarization. At a certain frequency this results in a strong absorption that is strongly affected by the effective medium permittivity, ε_{eff}

The optical absorption cross-section σ for nanoparticles is found according to the Mie theory[20] that present a formalism to apply Maxwell's equations for the interaction of an electromagnetic wave with metallic clusters. As the studied nanoparticles are about 10 nm in diameter we fulfill the conditions for the quasi-static approximation, indeed the radius of the particles is much smaller than the wavelength of the incident light. So the expression for σ can be approximated like shown in equation 2.1.

$$\sigma = 12\pi \frac{\omega}{c} \varepsilon_m^{3/2} R^3 \frac{\varepsilon_2(\omega)}{[\varepsilon_1(\omega) + 2\varepsilon_m]^2 + \varepsilon_2^2(\omega)} \tag{2.1}$$

With ε_m the permittivity of the medium surrounding the NPs, $\varepsilon(\omega) = \varepsilon_1(\omega) + i\varepsilon_2(\omega)$ the permittivity of the nanoparticle, ω the frequency of the incoming light and c the speed of light. We already notice here that the conditions for a resonance are found when $\varepsilon_1(\omega) = -2\varepsilon_m$ [2]. To account for the fact that the NPs are confined in a network we can introduce the effective medium permittivity, ε_{eff}, to replace ε_m in equation 2.1. The effective medium permittivity is dependent on the volume fraction occupied by the nanoparticles i.e. the filling factor f. Following the Maxwell-Garnett effective medium theory we can express ε_{eff} in equation 2.2 [21, 22].

$$\varepsilon_{eff}(\omega) = \varepsilon_m \frac{1+2f\Lambda}{1-f\Lambda} \text{ with } \Lambda = \frac{\varepsilon_1(\omega)-\varepsilon_m}{\varepsilon_1(\omega)+2\varepsilon_m} \tag{2.2}$$

So we can now express the condition for a resonance at frequency ω_{SPR} in equation 2.3.

$$\varepsilon_1(\omega_{SPR})(1-f) + \varepsilon_m(2+f) = 0 \tag{2.3}$$

Indeed, this relation yields the usual Mie condition $\varepsilon_1 + 2\varepsilon_m = 0$ for nanoparticles in solution i.e. $f = 0$. The assumptions made, have been successfully used for a wide range of 2D nanoparticle arrays[10, 23]. From equation 2.3 we see that the wavelength at which the resonance takes place is dependent on the filling factor i.e. on the particle size. Most importantly, the resonant wavelength is dependent on the permittivity of the medium. The dependence on the permittivity of the medium is a key feature in our experiments as we will see later on.

The experimental setup to probe the surface plasmon resonance of the printed networks is basically composed of a light source (deuterium-halogen) and a spectrometer. The network is printed on a quartz substrate (transparent to UV) that is placed between the light source and the spectrometer, see figure 2.13. All the parts are connected by optic fibers. The apparatus is interfaced by a computer and a dedicated software. The wavelengths scanned lie between 300 nm and 800 nm, while the maximum absorption of the SPR for 10 nm gold nanoparticles is found in the range of 560 to 620 nm. In figure 2.13 B we show the absorption spectrum for a network of gold nanoparticles (10 nm in diameter) on a quartz substrate. As we have seen above the SPR peak is dependent on the surrounding medium permittivity, which makes this technique well suited for monitoring the changes in the molecular species surrounding the NP's, as we will explore below.

[2] note that the function $\varepsilon_1(\omega)$ is negative and linear in this range of wavelengths

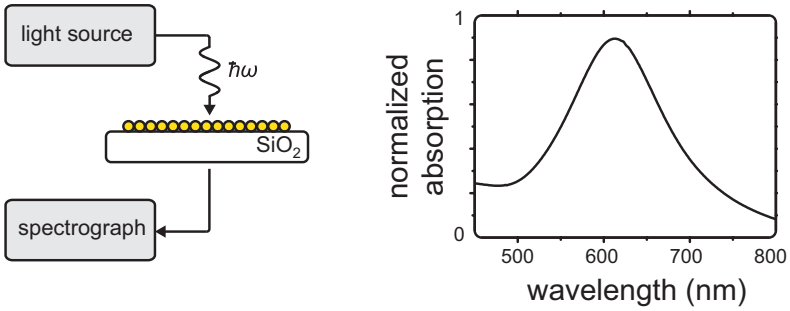

FIGURE 2.13: **Schematic view of the spectroscopy experimental setup and typical result.A** The measurements are done in transmission i.e. the sample is illuminated at one side and the spectrograph is scanning the signal going through the sample at the other side. **B** A typical absorption curve for a printed network on quartz. The array is solely composed of octanethiol covered gold nanoparticles.

2.3 MOLECULAR EXCHANGE

Once we have a network composed of ordered alkanethiol protected gold nanoparticles which is fully characterized electronically and optically we can insert the molecules we are actually interested in. We can tune roughly the inter-particle distance by choosing the appropriate alkanethiol to cap the NP's [10]. Indeed increasing the length of the alkanes increases the interparticle distance. For the organic molecules we intend to insert in the arrays, octanethiol is the best candidate to fix the interparticle distance. In figure 2.14 we show the chemical structure of the three molecules investigated in this work, oligophenylethynylene with 3 rings and dithiolated (OPE3DT), anthraquinonedithiol (AQDT) and anthracenedithiol (ACDT). The OPE3 molecule is a logical molecule to probe in order to test our technique as it is a conjugated 'fruit-fly' for molecular electronics that has been widely studied [7, 10, 24–28]. In contrast, the AQDT and ACDT are designed and synthesized to study the influence of cross-conjugation on the charge transport properties of molecules[29]. The ACDT molecule is expected to have a good conductance, similar to the OPE3 molecule as it is a fully conjugated molecule. The AQDT molecule, however, is expected to have a much lower conductance than ACDT although they have almost the same structure. The only difference is that the conjugation is broken in the case of AQDT. This lower conductance has been predicted theoretically and attributed to quantum interferences[30] (for more information see chapter 6). Additionally a molecule has been synthesized that can switch between the high conducting configuration (ACDT) and the low conducting configuration (AQDT) by a redox reaction [29]. All molecules are dithiolated i.e. they are terminated at both ends with a sulfur atom, making a covalent bound with the gold nanoparticles possible. So the insertion of a dithiolated molecule between two nanoparticles forms a conducting bridge, transforming the tunnel junction formed by two NP's into a metal-molecule-metal junction. With this technique we compare the resistance of the network before the insertion of the network and the resistance after insertion. In addition we can follow the change in SPR by spectroscopy as the inserted molecules modify the medium permittivity, ε_m. Similarly we can do the reverse reaction by replacing the inserted molecules by octanethiols, this step is called the back-exchange. The resistance values and SPR peak position returns to their original values.

2.3.1 EXPERIMENTAL DETAILS

To start with, we use a freshly made device, as described above, to measure its original resistance and SPR peak values. To prevent the observed time dependence we only start measuring after at least two hours. Next the devices

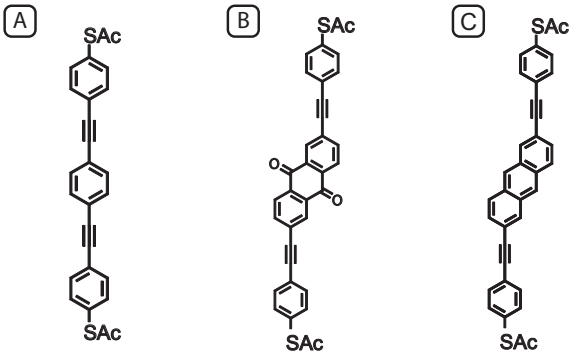

FIGURE 2.14: **Chemical structure of OPE3DT, AQDT and ACDT. A** we show OPE3DT, dithiolated oligophenylethynylene with 3 rings **B** AQDT, dithiolated anthraquinone **C** ACDT, dithiolated anthracene based wire. Those molecules where synthesized by Hennie Valkenier at the Groningen university.

are transfered to a glove-box with protected atmosphere (dry N_2) and are immersed in a 0.5 mM solution of molecules (OPE3DT, AQDT or ACDT) in THF. Prior to the immersion of the devices, the molecules in solution are deprotected i.e a protection group covering the sulfur atom is chemically removed by adding amonium hydroxide (for OPE3DT) or triethylamine (for ACDT and AQDT)[25]. The devices are left in solution for 24 hours and prior to use are rinsed in clean THF and blown dry with nitrogen. After this cleaning step we assume only the molecules attached to the gold NP's remain. Following this protected atmosphere step, the devices are electronically and optically characterized in air. After this measurement step we perform the back-exchange in the same manner as described for the exchange only using octanethiol instead of OPE3DT or ACDT. Again the devices are probed in the same fashion as described above.

2.3.2 RESISTANCE AND SPR SHIFTS

In figure 2.15 we show the measured resistance values for a device prior and after molecular exchange with OPE3DT. We also show the resistance values after back-exchange. We observe a decrease in resistance of roughly a factor 30 between the bare network and the network with inserted OPE3DT molecules. The reverse reaction yields a similar change in resistance. We measure sheet resistances ranging from 0.1 GΩ to 1 GΩ for networks where OPE3DT has been inserted (average value 0.35 ± 0.2 GΩ), similar values have been found for previous work on OPE3DT in nanoparticle networks [7, 10, 24]. Moreover sin-

gle molecule experiments (STM and MCBJ) presented resistances for OPE3DT ranging from 0.5 GΩ to 0.07 GΩ [26, 27, 31, 32], so all in all quite in agreement with our measurements. In chapter 5 using conducting AFM we measure the resistance of a self-assembled monolayer of OPE3DT, when corrected for the approximate number of molecules contacted, the resistance for a single molecule is in the order of a GΩ. The exchange reaction can be monitored not only by

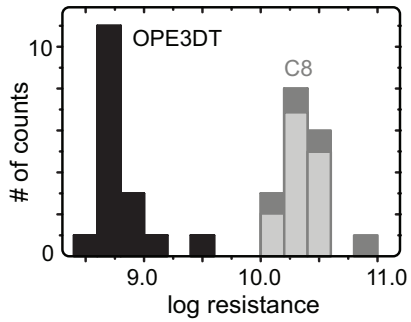

FIGURE 2.15: **Resistance shift after OPE3DT exchange and back-exchange.** Measured (log) resistance (in Ω) for different devices on the same sample. The logarithm of the resistance is linearly binned to construct the histogram. In gray the bare network, solely consisting of Au nanoparticles covered with octanethiol. In black the same network with the OPE3DT molecules inserted. In light-grey the resistance measured after back-exchange.

measuring the change in resistance of the device but also, as we have seen above, by measuring the shift in SPR with UV-vis spectroscopy. In figure 2.16 we show the absorption spectra for a bare network before the exchange, after the exchange and after the back-exchange.

A shift of about 22 nm in wavelength is observed when the OPE3DT molecules are inserted, moreover after back-exchange the SPR peak shifts back to its original value. Qualitatively this red-shift for the insertion of OE3DT is expected. Indeed the OPE3DT is a conjugated molecule and has a larger permittivity than the saturated chain of octanethiol ($\varepsilon_{OPE} = 3.1-3.9$ [33] and $\varepsilon_{C8} = 1.9-2.2$ [34]). As we can see in equation 2.3 an increase in ε_m results in an increase of the resonance wavelength $1/\omega_{SPR}$. Quantitatively the red-shift is expected to be larger for a complete molecular exchange. As the ratio of exchanged molecules

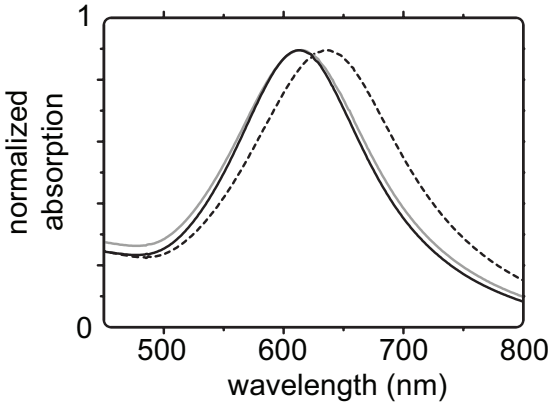

FIGURE 2.16: **SPR peak shift after OPE3DT exchange.** The normalized absorption is plotted on the y-axis and the wavelength on the x-axis. The black line is for the bare network, the dotted black line for the network after OPE3DT exchange and the grey line is for the network after back-exchange.

is not known precisely it is difficult to make a quantitative prediction of the SPR red-shift.

The results for the insertion of ACDT are presented in figure 2.17 although here no back-exchange reaction has been performed. Here we observe a change in resistance of about a factor 50 for ACDT, similar to OPE3DT. Indeed ACDT is also a linear conjugated molecule, though a bit longer than OPE3DT (2 nm for OPE3DT and 2.4 nm for ACDT). The averaged sheet resistance value for ACDT is 0.13 $(+0.2/-0.06)$ GΩ which is quite in agreement with values found with single molecule experiments (STM and MCBJ): 0.6 GΩ in a MCBJ [3], 0.27 GΩ in a STM break junction and 0.51 GΩ in a MCBJ [35][4]. Additionally similar values (0.45 GΩ) are found with conducting AFM measurements as shown in chapter 6. ACDT has successfully been inserted in 2D nanoparticle networks, reproducing resistance values found with different measurement techniques [36]. We note here that the molecular exchange of AQDT, expected to have a resistance 2 orders of magnitude higher than ACDT (see chapter 6), was only performed once and did not present conclusive results.

[3] Measured in Delft by Mickael Perrin at the MED-group
[4] STM and MCBJ both measured in the group of Thomas Wandlowski

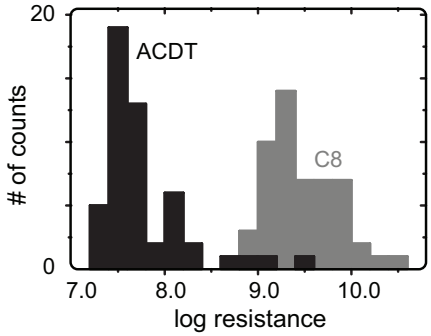

FIGURE 2.17: **Resistance shift after ACDT exchange.** Measured (log) resistance values (in Ω) for different devices on the same sample. The logarithm of the resistance is linearly binned to construct the histogram. In gray the bare network, solely consisting of Au nanoparticles covered with octanethiol. In black the same network with the ACDT molecules inserted.

In summary, we performed molecular exchange in NP networks with OPE3DT as a reference molecule to validate this novel measurement technique. The obtained resistance values are consistent with the literature. Moreover the measured shift in SPR is comparable to earlier experiments on nanoparticle networks [10] and is consistent with theory. Additionally we also successfully inserted the ACDT molecules in the arrays which resulted in a similar resistance shift. These results are in agreement with our expectations. All in all we have a strong indication that the inserted molecules do indeed bridge the nanoparticles in the array, although a solid proof is still lacking. In the last part of this chapter we elaborate more on this subject.

2.4 GATING THE NANOPARTICLE NETWORKS

To modulate charge transport in molecular devices, the use of a third electrode, a gate, is useful. This is an essential addition to two terminal molecular junctions to study thoroughly molecular charge transport. Here we present the first measurements on gated nanoparticle arrays. Although gates are widely used for macromolecules like carbon nanotubes [37, 38] it is still a challenge for smaller organic molecules in electromigrated junctions [2, 39, 40] or in me-

chanically controlled break junctions[41]. The advantages of a NP's network in combination with a gate, make the study of gated molecular charge transport possible even at room temperature. The electric field created by a positive gate voltage pulls the molecular energy levels to a lower energy, while a negative gate voltage shifts the levels to higher energies as shown schematically in figure 2.18-A. So by simultaneously measuring the resistance we obtain information on the position of the levels as we may shift them so far that they enter the bias window resulting in resonant tunneling[42]. In figure 2.18-B we show the calculated transmission function for ACDT for zero, positive and negative gate voltage. We see that at the Fermi energy the transmission is higher for negative gate voltages and lower for positive voltages, so the corresponding zero bias conductances will be ranked in the same order. In this case the shift in the transmission function is not large enough to make resonant tunnelling possible, nonetheless we can distinguish between HOMO or LUMO mediated transport by monitoring the sign of the gate voltage dependence of the resistance. In fact, as we will show in chapter 6, the position of the Fermi energy relative to the molecular levels is difficult to predict theoretically. So gated measurements on molecular junctions can make the determination of E_F relative to the HOMO or LUMO possible.

2.4.1 Experimental details

First of all let us discuss shortly the experimental details of applying a gate voltage to a self-assembled network of nanoparticles. Here we fabricate our devices in the same way as described above except we use a heavily doped silicon wafer as substrate. We here make a so-called back-gate by contacting the doped silicon, that is separated from the network and the electrodes by a 250 nm thermally grown oxide layer (see figure 2.19). In figure 2.20 we show the resistance when the gate voltage is changed discontinuously from 0 to -100 V. In the same way as in regular two terminal measurements we observe a time dependence of the measured resistance (see figure 2.10). We showed that the resistance gets constant after a few tens of minutes. The origin of this dependence is unknown but we expect it is probably due to the movement of trapped charges under the influence of the high gate voltages in the oxide layer. Note that the time constant of the time dependence of the resistance is too large to be due to charging or discharging of the Nps. In the next set of measurements, shown below, we plot the resistance versus the applied gate voltage. We vary the gate voltage in small steps of 10 V and wait at least 20 minutes before the next step to avoid the time dependence.

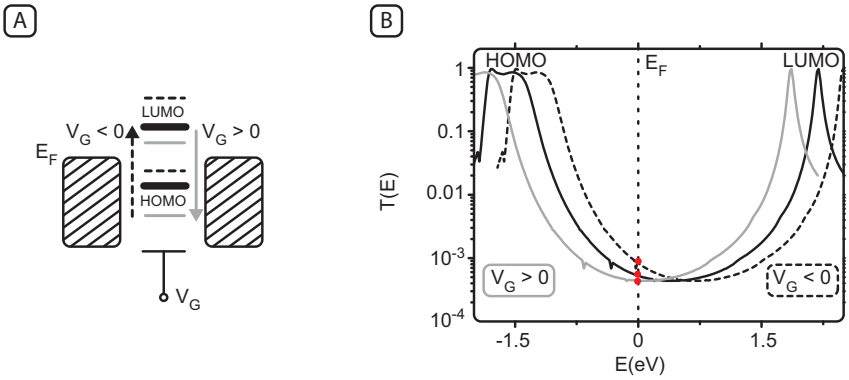

FIGURE 2.18: **Effect of a gate voltage on molecular conductance. A** Schematic energy diagram of a molecular junction with a gate voltage applied (zero bias). **B** Energy dependent transmission function for ACDT. The transmission function is calculated by Troels Markussen (DTU, Denmark)[43]. Here we can distinguish the HOMO and the LUMO peaks. The Fermi level is set at 0 eV. We show the shift of the transmission curve due to the gate voltage applied. The curve shifts to lower energies for positive gate voltages (grey line) and to higher energies for negative gate voltages (dashed black line). The dots indicate the cross-section of the transmission curve and the Fermi energy.

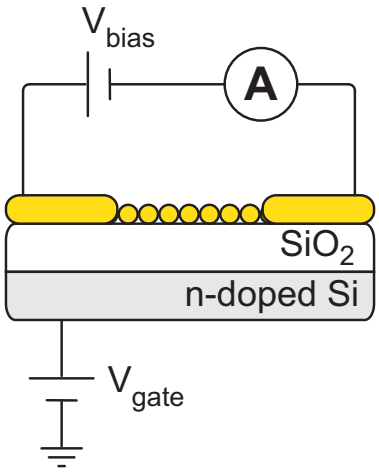

FIGURE 2.19: **Gating the nanoparticle network.** Schematic view of the device.

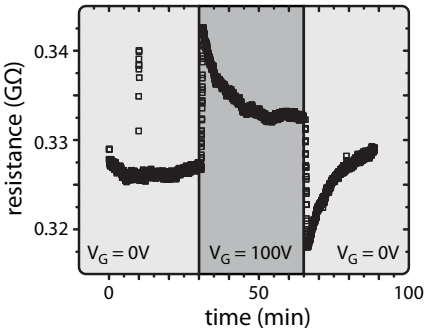

FIGURE 2.20: **Time dependence of the resistance when applying a gate voltage.** Here we show the measured resistance in GΩ for a bare (octanethiol) NP network for different gate voltages. In light gray we show the periods with 0V gate voltage and in dark gray the period with 100 V gate voltage applied.

2.4.2 GATE DEPENDENCE OF THE MEASURED RESISTANCE

We performed gated measurements on devices before molecular exchange (bare networks) and after molecular exchange (ACDT), the results of this experiment are shown in figure 2.21. Here we plot the normalized resistance change $(\Delta R/R = (R_{(gate)} - R_{(V_G=0V)})/R_{(V_G=0)})$ for each gate voltage for both cases. To study the influence of the gate potential on the resistance, $\Delta R/R$ is a relevant parameter. Indeed in the transmission picture (see figure 2.18-B) $\Delta R/R$ is equivalent to $-\Delta G/G$ which on its turn is proportional to $-\Delta T(E_F)/T(E_F) \propto \Delta(\ln(T(E_F)))$ for the zero-bias regime. To illustrate this, in figure 2.18-B we show with red dots the transmission at the Fermi energy, $T(E_F)$ for no gate voltage as well as for positive and negative voltages. As the $T(E)$ is plotted on a logarithmic scale $\Delta R/R$ is proportional to the distance between the red dots in figure 2.18-B. The gate coupling parameter, quantifying the extent to which the levels are going up or down, is not known for our devices, but is expected to be in the order of 10^{-3} [39]. So we can expect the shifts in transmission to be small enough to consider the transmission function linear for this small interval. For HOMO (LUMO) mediated transport we expect a linear resistance dependence on the gate voltage with a positive (negative) slope.

The first observation we make is that the gate dependence of the resistance for the bare network is less than the one for the network with inserted ACDT's indeed the slope for ACDT is $2.5 \times 10^{-4} \pm 5 \times 10^{-6}\ V^{-1}$ and the slope for C8 is $9.2 \times 10^{-5} \pm 3 \times 10^{-6}\ V^{-1}$. Besides we also notice that both slopes are positive. First let us discuss the case of ACDT. The positive slope measured indicates, as

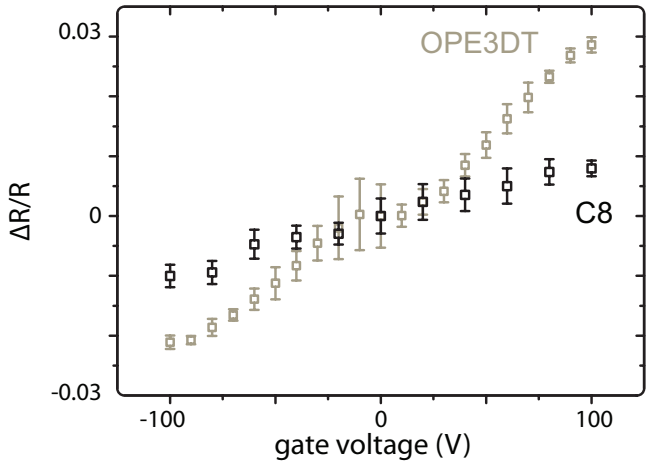

FIGURE 2.21: **Gate dependence of the network resistance for a bare network and after exchange with ACDT.** In this figure we show the relative change in resistance in function of the gate voltage. In black the trace for the bare network, in gray the trace for the same network after ACDT exchange. All data points are averages of multiple gating cycles, the error bar shows the standard deviation.

discussed above, HOMO mediated transport, this is consistent with literature [44–46]. To get a more quantitative look at our results we need to know the gate coupling parameter α relating the extent the molecular level shift with regard to the applied gate potential. One way to determine α is to compare the gate dependence measured with the calculated transmission function for ACDT. For this we need to assume that the position of the Fermi level relative to the molecular levels is well predicted by the calculations. Finally we find a gate coupling $\alpha = 2.6 \times 10^{-4}$ which is an order of magnitude lower than the gate coupling calculated for similar back-gate experiments (250 nm oxide layer, $\approx$ 2 nm gap), though on single molecule junctions [39]. In our case we look at a network of molecules connected to each other by gold nanoparticles, acting as miniature electrodes. Very likely the electrostatic potential on the nanoparticles is shifted too by the gate potential. This will obviously result in a lower effective gate

coupling, α.

Another plausible explanation for the lower α can also be found in the geometry of our devices, indeed we are not studying single junctions but 2D arrays of junctions. As a matter of fact the gate should have effect on all the junctions of the conducting paths to have a noticeable gate effect. So possibly due to percolation, inhomogeneities in the inserted molecules, inhomogeneities in the gate electrode and defects in the network a lower gate coupling is achieved.

Now let us turn to the octanethiol (bare network) results. Here the gate dependence of the resistance is lower than for ACDT (see figure 2.21). Naively we can ascribe this to a shallower transmission function of the octanethiol around E_F which is indeed the case [47]. Nevertheless the situation is more complicated as the octanethiols are only bound to one nanoparticle as they are monothiolated. Still, if we consider the octanethiol DOS at each electrode, the gate voltage can influence the distribution of the DOS relative to the Fermi level and so influence the resistance of the junction.

As a final remark, we demonstrated here that the use of a back-gate on a 2D nanoparticle network device looks promising. Although only a low gate coupling is obtained we still can distinguish between HOMO or LUMO mediated transport. Here we showed for ACDT that the charge transport is HOMO mediated, confirming the prediction that E_F is at the HOMO side of the transmission curve.

2.5 Evaluation of the technique

All the results mentioned above are based on the assumption we can insert dithiolated molecules in the network that bind at both sides to the gold nanoparticles. In this section we have a critical look at the technique we just presented and discuss whether or not we can claim that the molecules of interest do really bridge the nanoparticles.

First of all there is a discrepancy between the length of the molecules to insert and the interparticle distance. Indeed the molecules are shorter (1.9 nm for the OPE3DT) than the space between two nanoparticles (2.6 $\pm$ 1.4 nm for octanethiol spacer molecule, see ref[7]). Of course the inter-particle distance is not constant, 2.6 nm is only the mean value, there is a broad distribution of inter-particle distances (see ref[7]). Unfortunately it is impossible for us to reduce the inter-particle distance by using shorter spacer molecules like hexanethiol for example. Indeed shorter spacer molecules do not counter the attractive NP's van der Waals forces[48], leading to an unstable network where aggregation of the NP takes place.

In order to measure a change in the resistance of a 2D network, after molec-

ular exchange, at least one conducting path must form from one electrode to the other[49]. This means that an undisrupted chain of NP-bridging molecule-NP must form between the electrodes. The probability that such a path exists is directly related to the bridging ratio. The probability for a conducting path across a network to exist reaches 1 when the bridging ratio is at the percolation threshold. The percolation threshold for a triangular lattice is 0.35 for an infinitely extending array[50]. This means that when about 35% of the possible junctions are bridged, the probabilty that a conducting path exists is approaching 1. So at least 35% of the junctions should have a width similar or smaller than the molecular bridge length, corresponding to region 1 in the schematic reprezentation of the interparticle distance distribution of figure 2.22. This results in a high probability that a majority of the junctions will not be fully bridged by a molecule as shown schematically in figure 2.23-B and -C. Still one or more conducting paths of inserted molecules are possible depending on the precise morphology of the network.

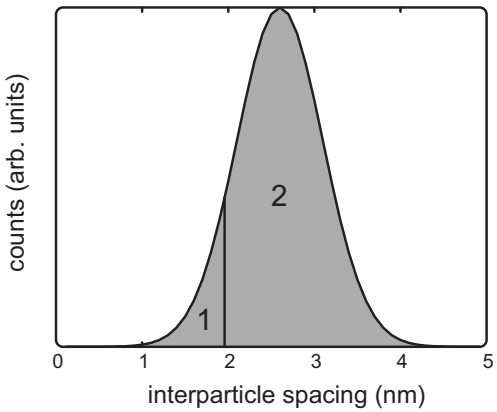

FIGURE 2.22: **Schematic distribution for junction widths for octanethiol gold NP networks.** In region 1 we show the range of NP-NP distances suited for an OPE3DT molecule to bridge them, corresponding to figure 2.24-A. In region 2 we show the range of NP-NP distances that are longer than the OPE3DT length, corresponding to figure 2.24-B and C. The distribution is based on the measured interparticle distance, d = 2.6 ± 1.4 nm, from reference [7].

We may wonder what the effect is of molecular exchange on the percolation properties of the networks. Does the correlation of the resistance measurements before and after exchange depend on the configuration of the inserted

molecules? In figure 2.23-A we highlighted the relation between consecutive measurements on different junctions by drawing lines (grey) between the data points. We indeed notice that this relation is found back in the measurements after molecular exchange. We illustrate this correlation in figure 2.23-B by plotting the resistance before exchange vs the resistance after exchange. In this particular series of measurements we clearly observe a correlation between the measurements prior to and after molecular exchange. This correlation is also found in other experiments performed on 2D nanoparticle networks[7, 10, 24].

The molecules can be inserted between the nanoparticles in three possible manners as shown in figure 2.24. The molecule can bridge the nanoparticles as in figure 2.24-A and so form a NP-molecule-NP network. If enough junctions have the appropriate length, a conducting path of molecules will form. Hence all the measured junctions will have approximately the same change in resistance leading to the correlation found in figure 2.23. In figure 2.24-B and C the inserted molecules do not fully bridge the junctions, they only form one S-Au bond i.e. they only surround the NPs. In the scenario shown in figure 2.24-B the molecules undergo π - π stacking which results in a situation similar to the one sketched in figure 2.24-A, though with a higher resistance. Thus we can as well expect in such a π - π stacking configuration a correlation of the measured resistances. Finally for the case the molecules only bind at one side to the gold nanoparticles without the formation of π - π stacks (figure 2.24-C), we can describe the situation best as a tunnel junction. In this case the tunnel junctions formed by alkanethiols before molecular exchange lower their apparent barrier height as both sides of the junction are now populated by conjugated molecules. Also here we expect a correlation between the resistances prior and after exchange. We note that the last two situations are relevant when too many NP-NP junctions have a length that is too big to be bridged by the inserted molecules. We see here that based on the resistance measurements and the correlation between them it is difficult to pin point a particular configuration of the molecules in the junctions. A more realistic picture is off course that all the configurations are present, but still one should be dominant. To deduce the dominant configuration of the dithiolated molecules in the network we need complementary measurements. We describe below the use of UV-Vis spectroscopy in combination with resistance measurements.

We have seen that the combination of charge transport measurements and UV-vis spectroscopy is a powerful tool for molecular electronics as we can check for the presence of the dithiolated molecules with two independent techniques. Nevertheless it remains difficult to prove to what extent bridging takes place. The basic difference between the two techniques is the type of molecular configuration that is probed. Indeed for charge transport only the molecules present

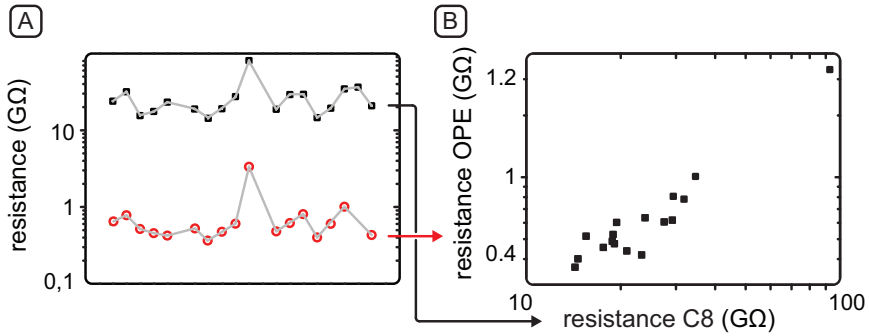

FIGURE 2.23: **Correlation of the resistance measurements after molecular exchange A** Measured resistance before molecular exchange (squares) and after OPE3DT insertion (dots) for different samples. The gray line shows the correlation of the data before and after molecular exchange. **B** Plot of the resistance of the samples before exchange (x-axis) versus the resistance after exchange (y-axis) showing the correlation of the data plotted in **A** in a different way.

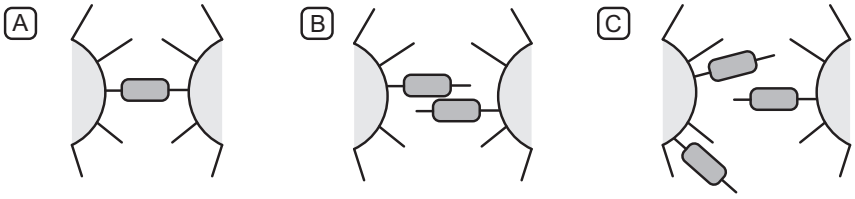

FIGURE 2.24: **Different configurations for molecules inserted between two nanoparticle.A** the inserted molecule is fully bridging the junction. **B**π-π stacking of the inserted molecules in a junction larger than the molecular length.**C)** same condition as in B but without the π-π stacking.

in the space between two NP's are contributing to the transport. In this space they can be bridging the junction or just attached to one of the two NP's. While for the absorption experiments one probes the change in permittivity of the medium (ε_m) due to the presence of the OPE molecules all around the NP's. So here we see that the spectroscopy measurements only can tell whether or not the molecules have exchanged their places on the NP's. Measuring the SPR shift can not make the distinction between molecules bridging the NP-NP junctions and the ones only surrounding the NPs.

To finish our discussion on the insertion of molecular species into a 2D nanoparticle network let us summarize our findings. From charge transport measurements we can prove that the insertion of molecular species into the network is successful. The debate is still open for the precise configuration of the molecules in the junctions. Probably we are measuring a combination of intra- and inter-molecular charge transport. A possible way out is to make use of monothiolated ligands molecules capable of forming a complex molecule around a single ion like iron, making the formation of bridges certain [51].

2.6 Conclusions

In this chapter we have demonstrated a technique to contact molecules through self-assembly processes. The use of 2D nanoparticle networks for molecular electronics presents numerous advantages. They are stable platforms to study charge transport even at room temperature. They offer the possibility of performing three-terminal transport measurements although more work is needed to pin point the actual effect of a gate on the transport properties. We can couple optical investigation methods to the transport measurements in order to confirm the molecular exchange reaction although we can only measure the presence of the molecules around the nanoparticles rather than confirming the formation of molecular bridges between NP's. Moreover the obtained resistance values with this technique are in good agreement with other measurements techniques (see chapter 5) and the single-molecule-measurements literature. To circumvent the doubt of not having a molecule bridging the NP's after molecular exchange we also turn to a complementary method for measuring the conductance of organic molecules: conducting AFM on self-assembled monolayers, as we will show in the following chapters (chapter 5 and 6).

References

[1] C. A. Martin, D. Ding, H. S. J. van der Zant, and J. M. van Ruitenbeek, *Lithographic mechanical break junctions for single-molecule measure-*

ments in vacuum: possibilities and limitations, New Journal of Physics **10**, 065008 (2008).

[2] E. A. Osorio, K. O'Neill, M. Wegewijs, N. Stuhr-Hansen, J. Paaske, T. Bjornholm, and H. S. J. van der Zant, *Electronic excitations of a single molecule contacted in a three-terminal configuration*, Nano Letters **7**, 3336 (2007).

[3] R. H. M. Smit, Y. Noat, C. Untiedt, N. D. Lang, M. C. van Hemert, and J. M. van Ruitenbeek, *Measurement of the conductance of a hydrogen molecule*, Nature **419**, 906 (2002).

[4] S. Kubatkin, A. Danilov, M. Hjort, J. Cornil, J. L. Bredas, N. Stuhr-Hansen, P. Hedegard, and T. Bjornholm, *Single-electron transistor of a single organic molecule with access to several redox states*, Nature **425**, 698 (2003).

[5] H. B. Akkerman, P. W. M. Blom, D. M. de Leeuw, and B. de Boer, *Towards molecular electronics with large-area molecular junctions*, Nature **441**, 69 (2006).

[6] D. J. Wold and C. D. Frisbie, *Fabrication and characterization of metal-molecule-metal junctions by conducting probe atomic force microscopy*, Journal of the American Chemical Society **123**, 5549 (2001).

[7] J. H. Liao, L. Bernard, M. Langer, C. Schönenberger, and M. Calame, *Reversible formation of molecular junctions in two-dimensional nanoparticle arrays (vol 18, pg 2444, 2006)*, Advanced Materials **18**, 2803 (2006).

[8] R. P. Andres, J. D. Bielefeld, J. I. Henderson, D. B. Janes, V. R. Kolagunta, C. P. Kubiak, W. J. Mahoney, and R. G. Osifchin, *Self-assembly of a two-dimensional superlattice of molecularly linked metal clusters*, Science **273**, 1690 (1996).

[9] S. J. van der Molen, J. H. Liao, T. Kudernac, J. S. Agustsson, L. Bernard, M. Calame, B. J. van Wees, B. L. Feringa, and C. Schönenberger, *Light-Controlled Conductance Switching of Ordered Metal-Molecule-Metal Devices*, Nano Letters **9**, 76 (2009).

[10] L. Bernard, Y. Kamdzhilov, M. Calame, S. J. van der Molen, J. Liao, and C. Schönenberger, *Spectroscopy of Molecular Junction Networks Obtained by Place Exchange in 2D Nanoparticle Arrays*, Journal Of Physical Chemistry C **111**, 18445 (2007).

[11] M. A. Mangold, C. Weiss, M. Calame, and A. W. Holleitner, *Surface plasmon enhanced photoconductance of gold nanoparticle arrays with incorporated alkane linkers*, Applied Physics Letters **94** (2009).

[12] J. Slot and H. Geuze, *A new method for preparing gold probes for multiple labeling cytochemistry*, European Journal of cell biology **38**, 87 (1985).

[13] R. D. Deegan, O. Bakajin, T. F. Dupont, G. Huber, S. R. Nagel, and T. A. Witten, *Capillary flow as the cause of ring stains from dried liquid drops*, Nature **389**, 827 (1997).

[14] T. Bigioni, X. Lin, T. Nguyen, E. Corwin, T. Witten, and H. Jaeger, *Kinetically driven self assembly of highly ordered nanoparticle monolayers*, Nature Materials **5**, 265 (2006).

[15] J. Tang, G. Ge, and L. E. Brus, *Gas to liquid and solid phase transition model for two-dimensional nanocrystal self-assembly on graphite*, The Journal of Physical Chemistry B **106**, 5653 (2002).

[16] X. Lin, H. Jaeger, C. Sorensen, and K. Klabunde, *Formation of long-range-ordered nanocrystal superlattices on silicon nitride substrates*, Journal of Physical Chemistry B **105**, 3353 (2001).

[17] R. Pool, P. Schapotschnikow, and T. J. H. Vlugt, *Solvent effects in the adsorption of alkyl thiols on gold structures: A molecular simulation study*, Journal Of Physical Chemistry C **111**, 10201 (2007).

[18] P. Schapotschnikow and T. J. H. Vlugt, *Understanding interactions between capped nanocrystals: Three-body and chain packing effects*, Journal Of Chemical Physics **131** (2009).

[19] Y. N. Xia and G. M. Whitesides, *Soft lithography*, Annual Review Of Materials Science **28**, 153 (1998).

[20] G. Mie, *Beitrage zur Optik traber Medien, speziell kolloidaler Metallasungen*, Annalen der Physik **330**, 377 (1908).

[21] J. C. M. Garnett, *Colours in Metal Glasses and in Metallic Films*, Philosophical Transactions of the Royal Society of London **203**, 385 (1904).

[22] R. W. Cohen, G. D. Cody, M. D. Coutts, and B. Abeles, *Optical Properties of Granular Silver and Gold Films*, Physical Review B **8**, 3689 (1973).

[23] H. Wang, C. S. Levin, and N. J. Halas, *Nanosphere arrays with controlled sub-10-nm gaps as surface-enhanced Raman spectroscopy substrates*, Journal Of The American Chemical Society **127**, 14992 (2005).

[24] J. Liao, M. A. Mangold, S. Grunder, M. Mayor, C. Schönenberger, and M. Calame, *Interlinking Au nanoparticles in 2D arrays via conjugated dithiolated molecules*, New Journal of Physics **10**, 065019 (2008).

[25] H. Valkenier, E. H. Huisman, P. A. van Hal, D. M. de Leeuw, R. C. Chiechi, and J. C. Hummelen, *Formation of High-Quality Self-Assembled Monolayers of Conjugated Dithiols on Gold: Base Matters*, Journal of the American Chemical Society **133**, 4930 (2011).

[26] X. Y. Xiao, L. A. Nagahara, A. M. Rawlett, and N. J. Tao, *Electrochemical gate-controlled conductance of single oligo(phenylene ethynylene)s*, Journal Of The American Chemical Society **127**, 9235 (2005).

[27] Y. Xing, T.-H. Park, R. Venkatramani, S. Keinan, D. N. Beratan, M. J. Therien, and E. Borguet, *Optimizing Single-Molecule Conductivity of Conjugated Organic Oligomers with Carbodithioate Linkers*, Journal of the American Chemical Society **132**, 7946 (2010).

[28] S. M. Wu, M. T. Gonzalez, R. Huber, S. Grunder, M. Mayor, C. Schonenberger, and M. Calame, *Molecular junctions based on aromatic coupling*, Nature Nanotechnology **3**, 569 (2008).

[29] E. H. van Dijk, D. J. T. Myles, M. H. van der Veen, and J. C. Hummelen, *Synthesis and properties of an anthraquinone-based redox switch for molecular electronics*, Organic Letters **8**, 2333 (2006).

[30] T. Markussen, J. Schiotz, and K. S. Thygesen, *Electrochemical control of quantum interference in anthraquinone-based molecular switches*, Journal of Chemical Physics **132**, 224104 (pages 6) (2010).

[31] R. Huber, M. T. González, S. Wu, M. Langer, S. Grunder, V. Horhoiu, M. Mayor, M. R. Bryce, C. Wang, R. Jitchati, et al., *Electrical Conductance of Conjugated Oligomers at the Single Molecule Level*, Journal of the American Chemical Society **130**, 1080 (2008).

[32] K. Liu, G. R. Li, X. H. Wang, and F. S. Wang, *Length dependence of electron conduction for oligo(1,4-phenylene ethynylene)s: A conductive probe-atomic force microscopy investigation*, Journal of Physical Chemistry C **112**, 4342 (2008).

[33] J. J. Stapleton, P. Harder, T. A. Daniel, M. D. Reinard, Y. Yao, D. W. Price, J. M. Tour, and D. L. Allara, *Self-Assembled Oligo(phenylene-ethynylene) Molecular Electronic Switch Monolayers on Gold: Structures and Chemical Stability*, Langmuir **19**, 8245 (2003).

[34] J. Israelachvili, *Intermolecular and surface forces* (Academic Press, 1985).

[35] W. Hong, H. Valkenier, G. Mészáros, D. Z. Manrique, A. Mishchenko, A. Putz, P. M. García, C. J. Lambert, J. C. Hummelen, and T. Wandlowski, *An MCBJ case study: The influence of π-conjugation on the single-molecule conductance at a solid/liquid interface*, Beilstein Journal of Nanotechnology **2**, 699 (2011).

[36] H. Valkenier, Ph.D. thesis, Groningen University (2011).

[37] S. Sapmaz, P. Jarillo-Herrero, J. Kong, C. Dekker, L. P. Kouwenhoven, and H. S. J. van der Zant, *Electronic excitation spectrum of metallic carbon nanotubes*, Physical Review B **71**, 153402 (2005).

[38] S. Tans, M. Devoret, H. Dai, A. Thess, R. Smalley, L. Geerligs, and C. Dekker, *Individual single-wall carbon nanotubes as quantum wires*, Nature **386**, 474 (1997).

[39] H. S. J. van der Zant, Y. V. Kervennic, M. Poot, K. O'Neill, Z. de Groot, J. M. Thijssen, H. B. Heersche, N. Stuhr-Hansen, T. Bjornholm, D. Vanmaekelbergh, et al., *Molecular three-terminal devices: fabrication and measurements*, Faraday Discussions **131**, 347 (2006).

[40] M. Poot, E. Osorio, K. O'Neill, J. M. Thijssen, D. Vanmaekelbergh, C. A. van Walree, L. W. Jenneskens, and H. S. J. van der Zant, *Temperature Dependence of Three-Terminal Molecular Junctions with Sulfur End-Functionalized Tercyclohexylidenes*, Nano Letters **6**, 1031 (2006).

[41] C. A. Martin, R. H. M. Smit, H. S. J. van der Zant, and J. M. van Ruitenbeek, *A Nanoelectromechanical Single-Atom Switch*, Nano Letters **9**, 2940 (2009).

[42] J. M. Thijssen and H. S. J. Van der Zant, *Charge transport and single-electron effects in nanoscale systems*, Physica Status Solidi B-Basic Solid State Physics **245**, 1455 (2008).

[43] J. Enkovaara, C. Rostgaard, J. J. Mortensen, J. Chen, M. Dulak, L. Ferrighi, J. Gavnholt, C. Glinsvad, V. Haikola, H. A. Hansen, et al., *Electronic*

structure calculations with GPAW: a real-space implementation of the projector augmented-wave method, J. Phys Condens. Matter **22** (2010).

[44] J. A. Malen, P. Doak, K. Baheti, T. D. Tilley, R. A. Segalman, and A. Majumdar, *Identifying the Length Dependence of Orbital Alignment and Contact Coupling in Molecular Heterojunctions*, Nano Letters **9**, 1164 (2009).

[45] V. Engelkes, J. Beebe, and C. Frisbie, *Length-dependent transport in molecular junctions based on SAMs of alkanethiols and alkanedithiols: Effect of metal work function and applied bias on tunneling efficiency and contact resistance*, Journal Of The American Chemical Society **126**, 14287 (2004).

[46] J. M. Beebe, B. Kim, C. D. Frisbie, and J. G. Kushmerick, *Measuring relative barrier heights in molecular electronic junctions with transition voltage spectroscopy*, ACS Nano **2**, 827 (2008).

[47] C. Li, I. Pobelov, T. Wandlowski, A. Bagrets, A. Arnold, and F. Evers, *Charge transport in single Au/alkanedithiol/Au junctions: coordination geometries and conformational degrees of freedom.*, Journal of the American Chemical Society **130**, 318 (2008).

[48] P. Schapotschnikow, R. Pool, and T. J. H. Vlugt, *Coarse-grained model for gold nanocrystals with an organic capping layer*, Molecular Physics **106**, 963 (2008).

[49] S. Kirkpatrick, *Percolation and Conduction*, Reviews of Modern Physics **45**, 574 (1973).

[50] J. C. Wierman, *Bond percolation critical probability bounds for three Archimedean lattices*, Random Structures & Algorithms **20**, 507 (2002).

[51] R. Chandrasekar, F. Schramm, O. Fuhr, and M. Ruben, *An Iron(II) spin-transition compound with thiol anchoring groups*, European Journal Of Inorganic Chemistry pp. 2649–2653 (2008).

3

Nanoparticle array based strain sensor

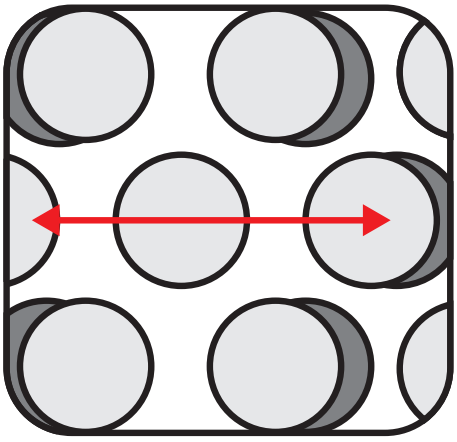

The results presented in this chapter have been published as:

C. M. Guédon, J. Zonneveld, H. Valkenier, J. C. Hummelen and S. J. van der Molen, *Controlling the interparticle distance in a 2D molecule-nanoparticle network*, **Nanotechnology**, **22**, 125205 (2011)

3.1 Introduction

Research in molecular electronics is strongly inspired by the possibility to encode a well-defined functionality, such as switchability, into a single molecule [1, 2]. On the road towards nanoscale functional devices, various fundamental questions arise. Many of these have to do with the details of the connection between a molecule and two electrodes. For example, the distance between the electrodes defines if and how a molecule can be connected between two metals. Moreover, a molecule that exhibits a significant length change upon switching is likely to lose its functionality in a rigid junction. Interestingly, the inverse may also be true, a possible example being spin transition molecules [3]. Since the length of such a molecule is larger in its high-spin than in its low-spin state, straining it may actually induce a spin transition.

Here, we aim for a stable molecular device structure which allows one to vary the inter-electrode distance on the sub-Ångstrom scale. For this, we combine two techniques which have proven their use in molecular transport studies: mechanically controllable break junctions (MCBJ) [4, 5], and 2D nanoparticle-molecule networks[6–9]. MCBJs are widely used to study single molecule conductance and allow for tuning of the inter-electrode distance with great accuracy. However, they lack stability at room temperature. Devices based on molecule-nanoparticle networks, on the other hand, offer great stability even at 293 K. One reason for this is that a nanoparticle-molecule-nanoparticle junction has a tiny mechanical loop. The other reason is that a conductance measurement forms a statistical average over a full array. Hence, fluctuations (molecular bond breaking and re-attachment) on the single junction level average out. Here, we combine the advantages of both techniques to create a 2D molecule-nanoparticle network in which the interparticle distance can be varied.

3.2 Experimental details

We start with the synthesis of gold nanoparticles (NP's) following the Slot and Geuze method [10]. In this way we obtain NP's that are 10 ± 1nm in diameter and charge stabilized in water. Next a solvent exchange step is performed (water to ethanol) to self-assemble alkanemonothiols, in this case octanethiols, on the NP's to prevent aggregation. After another solvent exchange step (ethanol to chloroform) the NP's are self-assembled into a 2D network on a convex air-water interface due to the evaporation of the solvent. This is followed by a microcontact printing step, i.e., the network is transfered from the water surface to the substrate using a polydimethylsyloxane (PDMS) stamp. Note that the self-assembled alkanethiols define the initial inter-particle distance[7]. As a bendable substrate, we use phosphor bronze which needs to be electroni-

cally isolated from the NP's. The insulating layer applied will also need to transmit the substrate deformation and to offer good adhesion to the NP network. We tested four different materials (PMMA, N-1410, SU-8 and poly-imide) spin coated on our substrates. Poly-imide, already used for MCBJ substrates [4, 11], shows the best adhesion properties for the NP's. Finally gold contacts are deposited by shadow mask evaporation, the electrodes being 160 μm apart. In this way, a network is created in which a unit junction comprises two nanoparticles separated by a tunnel barrier that consists of two monolayers of alkanemonothiols. From here it is also possible to create a 2D network of metal-molecule-metal junctions using a place exchange step[6–9]. This results in the formation of one or a few molecular junctions as discussed below (see also chapter 2). Interestingly, the network's sheet resistance can be directly related to the average resistance of a single junction [7](chapter 2).

For our experiments, we mount a substrate onto a MCBJ set-up, as illustrated in figure 3.1-A. A pushing rod, capable of bending the substrate in a three-point geometry, is driven by a motor that can be operated continuously or stepwise. The network on the substrate is connected via spring-loaded contacts to an IV-converter and a data acquisition card. A bias voltage of 2V is typically applied to the network, resulting in a voltage drop of a few mV for each junction. The resistance is recorded while bending. All the measurements are done at room temperature and in a low vacuum chamber at a pressure of about 10^{-3} mbar.

3.3 Results: bending the network

Let us first anticipate what happens when we bend a network with alkanemonothiols only, i.e. without dithiolated molecular bridges. When displacing the pushing rod by a distance Δy, as shown in figure 3.1A, the upper surface of the phosphor bronze substrate is elongated. Its deformation is transmitted by the poly-imide layer to the NP network (figure 3.1B), resulting in lateral strain on the network. To get a picture of the resulting resistance behavior of our structure, we note that a unit junction formed by two NP's is basically a tunnel junction. Its barrier height, φ, is defined by the work function of gold covered by alkanemonothiols. The barrier width is the distance d between the edge of two NP's as shown in figure 3.1C. For reasons becoming clear later, we also define u, the distance between the centers of the two nanospheres. The junction resistance can be written in the form: $R \propto e^{2\kappa d}$ where $\kappa = \frac{1}{\hbar}\sqrt{2m\varphi}$ with m the electron mass and $\hbar$ the reduced Planck constant. The change in resistance when elongating the junction with Δd is thus

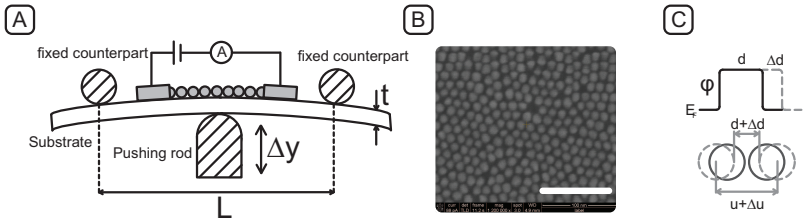

FIGURE 3.1: **Overview of the experimental details. A** Schematic cross-section of the measurement set-up. By bending a phosphor-bronze substrate in a three-point geometry, a 2D nanoparticle-molecule network is stretched. **B** Scanning electron micrograph of an octanemonothiol protected gold NP network; the scale bar shown is 100 nm. **C** Schematic view of the tunnel barrier when the distance between the surface of two nanoparticles is increased from d to d+Δd. We define u as the distance between the centers of the nanoparticles. Note that $\Delta u = \Delta d$. The height of the energy barrier equals φ.

expected to follow: $ln(R(\Delta d)/R(0)) = 2\kappa\Delta d$, where $R(0) \equiv R(\Delta d = 0)$. In the linear regime we can simplify this relation to: $(R(\Delta d) - R(0))/R(0) = 2\kappa\Delta d$. Hence, we can accurately monitor the displacement between the nanoparticles by measuring the network's resistance response.

In a typical experiment the substrate is bent back and forth by moving the pushing rod in steps of $\Delta y = 0.043$ mm. After each step the resistance change is probed. Figure 3.2 shows the result for a sample with octanemonothiol tunnel junctions with an initial resistance of 176 $M\Omega$. The data are plotted both linearly, showing $(R(\Delta d) - R(0))/R(0)$ vs Δy, and semi-logarithmically, displaying $\ln(R(\Delta d)/R(0))$ (see inset). Two experiments are shown; in the first case (black squares) the sample was bent less than in the second case (grey diamonds, also later in time). Figure 3.2 exhibits a plateau for small displacements. This has a trivial reason, as it corresponds to the situation where the pushing rod is not yet touching the substrate (see right bottom cartoon in figure 3.2). Once the substrate is actually bent, however, the resistance increases significantly, as anticipated above. For larger displacements, the curves deviate from linearity as indeed expected. Upon plotting $R(\Delta d)/R(0)$ semi-logarithmically, the curves become straighter. However a small deviation at high Δy is still present, probably due to plastic deformation (see below). As also can be seen on the other measurements in the supporting information we remain generally within the linear regime. The relative change in resistance $(R(\Delta d) - R(0))/R(0)$ per mm

pushing rod displacement for this sample is found to be 0.34 ± 0.02 mm^{-1} (from the black squares). We investigated five such samples and $(R(\Delta d) - R(0))/R(0)$ varied from 0.20 to 0.36 per mm pushing rod displacement, with an average of 0.30 mm^{-1}.

Let us now have a closer look at figure 3.2 and focus on the second experiment shown (grey diamonds) where the substrate is bent further than before, i.e. to Δy = 1.25 mm. In this case, the retracting trace does not come back to its original value. In fact, the plateau for small Δy, discussed above, is located at a higher resistance value and spans to higher Δy than before. This discrepancy is related to plastic deformation, i.e. permanent bending of the substrate as indicated in the left cartoon in figure 3.2. Hence, the pushing rod needs to move further up, to larger Δy, before additional bending is possible. All these observations demonstrate that the resistance change is due to network elongation, which itself results from deformation of the substrate. Hence, our device opens the road towards a strain sensor (or bending sensor) based on tunneling transport. In addition, we can deduce that the networks are more or less homogeneously deformed, i.e., deformation does not lead to fractures in the structure. Indeed, if fractures were formed, they would lead to large tunnel gaps and resistance increases much beyond our experimental results (see below). Furthermore, scanning electron microscopy (SEM) characterization after the bending experiment shows no evidence of fracture formation. We note that similar networks have been shown to be elastically deformable, with a Young's modulus of several GPa [12].

3.4 Analysis: How does the network deform?

Let us now have a more quantitative look at the deformation of the NP network and the resulting resistance changes. For this, we can rely on previous deformation calculations performed for MCBJs [4, 11]. When displacing the pushing rod by a distance Δy, the network will elongate by a distance ΔU, measured from electrode to electrode, as given by:

$$\Delta U = \frac{6tU\Delta y}{L^2}\zeta \tag{3.1}$$

Here L is the distance between the two fixed counterparts (20 mm in our case), t the thickness of the substrate (3 mm) and U the distance between the two evaporated electrodes (see figure 3.1) [4].

The correction factor ζ has been introduced by Vrouwe *et al.* to compensate for device-specific features such as undercut as well as stacking order of the different materials used [11]. In the ideal case where the deformation of the

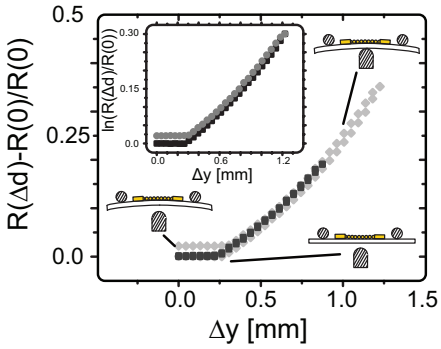

FIGURE 3.2: Relative resistance change as a function of pushing rod displacement, Δy. A schematic view of the substrate is shown next to the curve to illustrate: (i) the plateau for low displacements before the pushing rod touches the substrate, (ii) the case when the substrate is fully bent and (iii) hysteresis due to plastic deformation of the substrate. In the inset the same data is plotted in a semi-logarithmic way.

substrate is exactly transferred to the structure on top of it (MCBJ or network) $\zeta = 1$. In the case of lithographically defined MCBJ's the undercut amplifies the deformation of the substrate which results in $\zeta > 1$ [11].

The conductance through a NP network can be described from a simple unit cell as shown in figure 3.3 (see also chapter 2). Such a unit cell may be deformed in two ways. On the one hand, we consider the case where the NP's are well attached to the underlying layer. Then, the network will be deformed uniaxially as shown schematically in figure 3.3-A. On the other hand in figure 3.3-B we show the case where the NP's are loosely connected to the substrate. Then the network, when elongated in one direction, will be compressed in the perpendicular direction to keep its total surface constant; the so called Poisson effect. Let us define $N = U/u$ as the average number of nanoparticles between the electrodes in the $\hat{x}$ (or $\hat{u}$) direction. Consequently, for a network lattice direction lined up with the $\hat{x}$ direction $\Delta U = N\Delta u = N\Delta d$ (see figure 3.3). We can also calculate the length changes of the junctions in the other lattice directions, for both 2D-models, using simple trigonometry. With this we can obtain values for 2κ from the data for both 2D models. Let us first assume ideal transfer of deformation, i.e., $\zeta = 1$. The apparent 2κ values thus obtained in our experiments are 0.15 Å^{-1} for well attached NP's and 0.21 Å^{-1} for loosely connected NP's. These should be compared to a 2κ value of 0.87 Å^{-1} as experimentally found for alkanemonothiols in similar junctions [13]. We relate the discrepancy

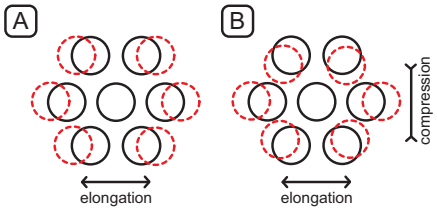

FIGURE 3.3: Schematic view of a basic lattice unit unstretched (black lines) and stretched (dotted lines). **A** The deformation is unidirectional as the NP's are well attached to the substrate. **B** As a consequence of the loosely attached NP's to the substrate the Poisson effect induces a compression in the direction perpendicular to the deformation.

to the incomplete translation of the substrate elongation to the network, i.e. to ζ being smaller than unity. Demanding that $2\kappa = 0.87\text{Å}^{-1}$ for our junctions as well, we find $\zeta = 0.18$ for uniaxially deformed networks and $\zeta = 0.24$ for Poisson deformed networks (full Poisson effect). There are several factors that may lead to a value $\zeta < 1$. Possibly, the polyimide layer takes up part of the deformation (unlike in MCBJ's there are no undercuts in our networks). However, our 2D NP array is also not perfect. It consist of many 2D-grains with a distribution of lattice directions. We tested our 2D-models for unit cells with different orientations, but found only small variations in ζ (up to 15 %). However, the grain boundaries may take up some of the strain. We note nevertheless that it is unlikely that the grain boundaries incorporate all elongation, since then a gap much larger than Δd would open. That would induce much larger resistance changes than we observe, due to the exponential nature of tunneling.

3.5 BENDING WITH BRIDGE-MOLECULES

As we have seen that a NP network can be controllably stretched, we can insert conjugated molecular bridges into it and study the response to deformation. For this, we choose acetyl protected dithiolated oligo-phenylene ethynylene molecules with three phenyl rings, i.e. OPE3. These are conjugated rod-like molecules (see lower inset of figure 3.4) that have been studied by several groups [7, 14]. The alkanemonothiol-protected gold NP networks are immersed in a 0.5 mM OPE3 solution, deprotected by triethylamine in tetrahydrofurane (THF), for 24 hours[15]. This allows the dithiolated OPE3 molecules to form bridges between two neighboring NPs, as indicated in the inset of figure 3.4 [7, 8]. (However, as we discussed in chapter 2, there is no conclusive proof of the

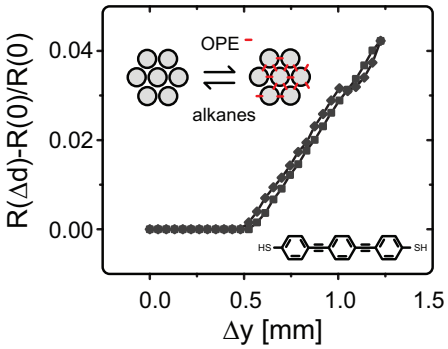

FIGURE 3.4: **Bending a network with OPE3-bridges.** Relative resistance change as a function of pushing rod displacement for a network with OPE3-bridges. The pushing trace is represented by squares and the backward trace features diamonds. In the upper inset the molecular exchange reaction is schematically depicted and in the lower inset the chemical structure of OPE3 is shown. Note the kink in the back trace around 1 mm, which is due to slipping of the driving motor

molecules fully bridging the nanoparticles.) After this procedure, the resistance of the network in figure 3.2 has dropped to 34 MΩ, as compared to 175 MΩ for the original alkanemonothiol network. The resistance change due to molecular exchange is considarably lower than found by Liao et al.[7], but close to the values found by the same group in ref. [8]. This discrepancy is probably due to an incomplete exchange reaction in our case. Nevertheless, the resistance change is large enough to conclude that transport is dominated by the OPE molecules. Figure 3.4 shows a bending experiment for an OPE-substituted sample, similar to the one in figure 3.2. We find that the network's resistance responds linearly to changes in Δy in the regime probed. The absolute resistance changes found are much smaller than for the alkanemonothiol networks. Moreover, also the relative resistance change $(R(\Delta d) - R(0))/R(0)$ has dropped significantly, from 0.34 ± 0.02 mm^{-1} for the initial network to 0.06 ± 0.01 mm^{-1} for the OPE-bridged sample. Since, apart from molecular insertion, the network itself is unchanged, we expect that $\Delta U/\Delta y$ and thus $\Delta d/\Delta y$ have the same values as for the original alkanemonothiol network (see equation 3.1). Hence, it is reasonable to state that the quantity $(\Delta R/R)/(\Delta d/d)$, i.e. the resistance response to strain, has dropped by a factor 0.34/0.06. In other words, the insertion of OPE-bridges has significantly changed the properties of our junctions, both in absolute resistance and in strain sensitivity. It is tempting to relate $(R(\Delta d) - R(0))/R(0)$ to the exponential factor 2κ, or more exactly, to the quantity β for the OPE-series. This

β-value is defined as the decay factor of conductance with molecular length L, for a series of oligomers [13, 16, 17]. However, we do not view this as the correct interpretation, since the OPE's are quite rigid rods compared to the relatively soft gold particles. It is more likely that the position of the molecule-Au connection changes upon straining the junction. For example, if the Au-thiol bond is initially near a step edge on the gold nanoparticle, it may jump over this edge to the upper gold layer upon pulling. Recently, Martin *et al.* argued that the latter configuration yields a higher resistance value [18].We note that the change of $(R(\Delta d) - R(0))/R(0)$ upon straining should then be seen as a statistical effect, i.e. as a result of shifting distributions in molecular anchoring. However we can also describe the results by assuming that the OPE3DT molecules do not bridge the NP's (see chapter 2). Indeed then the tunnel barrier is lowered by the presence of the OPE3 molecules.

We anticipate, however, that the situation will be very different for less rigid molecules. Especially spin transition molecules [19] are good candidates for future experiments, as they can be switched from a low-spin to a high-spin state when stretched[3]. In addition such molecules increase the certainty of the bridging (see chapter 2). Such measurements may be supported by surface enhanced Raman spectroscopy (SERS) studies, which would allow one to follow molecular vibrations as the junctions are strained.

3.6 Conclusions

In summary, we present a new method to statistically study molecular transport as a function of inter-electrode distance. Our platform combines the stability of 2D-molecular networks with the control of mechanically controllable break junctions with a maximal variation around 50 pm per junction. We demonstrate that both the absolute and relative resistance response depend on the molecular species present in the junctions. Hence, this study paves the road towards future experiments on strain-sensitive molecules. Moreover, using this technique, a strain sensor with tunable sensitivity can be considered.

References

[1] R. M. Metzger, *Unimolecular electronics*, Journal of Materials Chemistry **18**, 4364 (2008).

[2] S. J. van der Molen and P. Liljeroth, *Charge transport through molecular switches*, Journal Of Physics-Condensed Matter **22**, 133001 (2010).

[3] J. J. Parks, A. R. Champagne, T. A. Costi, W. W. Shum, A. N. Pasupathy, E. Neuscamman, S. Flores-Torres, P. S. Cornaglia, A. A. Aligia, C. A. Bal-

seiro, et al., *Mechanical Control of Spin States in Spin-1 Molecules and the Underscreened Kondo Effect*, Science **328**, 1370 (2010).

[4] N. Agrait, A. L. Yeyati, and J. M. van Ruitenbeek, *Quantum properties of atomic-sized conductors*, Physics Reports-Review Section Of Physics Letters **377**, 81 (2003).

[5] R. H. M. Smit, Y. Noat, C. Untiedt, N. D. Lang, M. C. van Hemert, and J. M. van Ruitenbeek, *Measurement of the conductance of a hydrogen molecule*, Nature **419**, 906 (2002).

[6] R. P. Andres, J. D. Bielefeld, J. I. Henderson, D. B. Janes, V. R. Kolagunta, C. P. Kubiak, W. J. Mahoney, and R. G. Osifchin, *Self-assembly of a two-dimensional superlattice of molecularly linked metal clusters*, Science **273**, 1690 (1996).

[7] J. H. Liao, L. Bernard, M. Langer, C. Schönenberger, and M. Calame, *Reversible formation of molecular junctions in two-dimensional nanoparticle arrays (vol 18, pg 2444, 2006)*, Advanced Materials **18**, 2803 (2006).

[8] L. Bernard, Y. Kamdzhilov, M. Calame, S. J. van der Molen, J. Liao, and C. Schönenberger, *Spectroscopy of Molecular Junction Networks Obtained by Place Exchange in 2D Nanoparticle Arrays*, journal of physical chemistry C **111**, 18445 (2007).

[9] S. J. van der Molen, J. H. Liao, T. Kudernac, J. S. Agustsson, L. Bernard, M. Calame, B. J. van Wees, B. L. Feringa, and C. Schönenberger, *Light-Controlled Conductance Switching of Ordered Metal-Molecule-Metal Devices*, Nano Letters **9**, 76 (2009).

[10] J. Slot and H. Geuze, *A new method for preparing gold probes for multiple labeling cytochemistry*, European Journal of cell biology **38**, 87 (1985).

[11] S. A. G. Vrouwe, E. van der Giessen, S. J. van der Molen, D. Dulic, M. L. Trouwborst, and B. J. van Wees, *Mechanics of lithographically defined break junctions*, Physical Review B **71** (2005).

[12] K. E. Mueggenburg, X. M. Lin, R. H. Goldsmith, and H. M. Jaeger, *Elastic membranes of close-packed nanoparticle arrays*, Nature Materials **6**, 656 (2007).

[13] H. B. Akkerman and B. de Boer, *Electrical conduction through single molecules and self-assembled monolayers*, Journal Of Physics-Condensed Matter **20** (2008).

[14] X. Y. Xiao, L. A. Nagahara, A. M. Rawlett, and N. J. Tao, *Electrochemical gate-controlled conductance of single oligo(phenylene ethynylene)s*, Journal Of The American Chemical Society **127**, 9235 (2005).

[15] H. Valkenier, E. H. Huisman, P. A. van Hal, D. M. de Leeuw, R. C. Chiechi, and J. C. Hummelen, *Formation of High-Quality Self-Assembled Monolayers of Conjugated Dithiols on Gold: Base Matters*, J. Am. Chem. Soc. **133**, 4930 (2011).

[16] N. J. Tao, *Electron transport in molecular junctions*, Nature Nanotech. **1**, 173 (2006).

[17] E. H. Huisman, C. M. Guedon, B. J. van Wees, and S. J. van der Molen, *Interpretation of Transition Voltage Spectroscopy*, Nano Letters **9**, 3909 (2009).

[18] M. N. Martin, J. I. Basham, P. Chando, and S. K. Eah, *Charged Gold Nanoparticles in Non-Polar Solvents: 10-min Synthesis and 2D Self-Assembly*, Langmuir **26**, 7410 (2010).

[19] R. Chandrasekar, F. Schramm, O. Fuhr, and M. Ruben, *An Iron(II) spin-transition compound with thiol anchoring groups*, European Journal Of Inorganic Chemistry pp. 2649–2653 (2008).

4

Interpretation of transition voltage spectroscopy

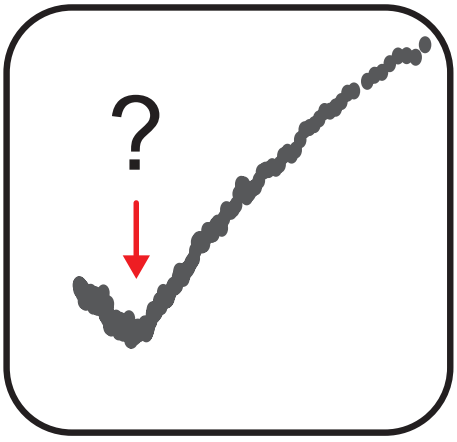

The results presented in this chapter have been published as:

E. H. Huisman, C. M. Guédon, B. J. van Wees and S. J. van der Molen, *Interpretation of Transition Voltage Spectroscopy*, **Nano Letters**, **9**, 3909 (2009)

and

M. L. Trouwborst, C. A. Martin, R. H. M. Smit, C. M. Guédon, T. A. Baart, S. J. van der Molen and J. M. van Ruitenbeek, *Transition Voltage Spectroscopy and the Nature of Vacuum Tunneling*, **Nano Letters**, **11**, 614 (2011)

The promise of 'transition voltage spectroscopy' (TVS) is that molecular level positions can be determined in molecular devices without applying extreme voltages. Here, we consider the physics behind TVS in more detail. Remarkably, we find that the Simmons model employed thus far is inconsistent with experimental data. Moreover we perform experiments on vacuum tunnel junctions to compare to molecular junctions and theory. We show that the promise of TVS is difficult to achieve.

4.1 TRANSITION VOLTAGE SPECTROSCOPY

Over the last decade, several methods have been developed to fundamentally study charge transport in metal-molecule-metal junctions [1–4]. Nevertheless, much of the physics behind molecular transport is still under debate. In fact, simple questions such as "Where does the voltage drop in a molecular junction?" and "Where are the molecular levels with respect to the electrodes' Fermi levels?" have not found general solutions yet. The latter question, for example, is hard to answer experimentally due to the limited voltage a two-terminal molecular junction can withstand. In a molecular device, the Fermi level (E_F) of the metal electrodes is typically a few eV away from the closest molecular level (see figure 4.1-A,E). Therefore, a bias voltage up to several volts is required before electrons from the metal can resonantly flow through a molecular level ('resonant tunnelling'). Generally, such voltages result in huge electric fields, $> 10^9$ V/m, causing breakdown before the molecular level is actually accessed. Recently, Beebe *et al.* found a creative way out of this dilemma [5, 6]. They state that the position of the nearest molecular level in a two-terminal device can be derived from I-V (current-voltage) measurements, even if the bias voltage is moderate and resonance is not yet reached. All that is needed is to replot of the I-V data in a form that is based on the physics of field emission. Due to its simplicity and elegance, this method, coined 'transition voltage spectroscopy' (TVS), is becoming a very popular tool in molecular electronics [7–11]. However, a basic justification is still lacking. This chapter is therefore devoted to the physical interpretation of TVS. Beebe *et al.* employ the Simmons model for tunnelling to interpret their data and justify TVS [12]. Surprisingly, we find that the experimental results they present are not at all in agreement with this model. We show that a coherent molecular transport model, however, does justify their approach. Additionally we perform measurements on vacuum tunnel junctions to validate our predictions experimentally. Finally we critically evaluate this technique as a spectroscopic tool.

To introduce TVS, we initially follow the approach by Beebe *et al.*. They

make the analogy between molecular charge transport and electron tunneling through a rectangular barrier, as described by Simmons (see figure 4.1A-D) [12, 13]. Within this framework, the height of the tunnel barrier, ϕ, equals the energy offset between E_F and the nearest molecular orbital. For thiol-terminated molecules, the nearest level is commonly the highest occupied molecular orbital (HOMO, with energy E_{HOMO}), so that $\phi = E_F - E_{HOMO}$ (hole transport) [5, 6, 14]. The barrier width, d, is set equal to the length of the molecule. Simmons showed that for bias voltages $V < \phi/e$ with e the electron charge, the effective tunnel barrier is lowered to $\phi - eV/2$ (see figure 4.1C). However, for high biases, $V > \phi/e$, the barrier shape becomes triangular and part of the barrier becomes classically available. This case is generally referred to as Fowler-Nordheim tunnelling (FN) or field emission [15]. Figure 4.1D illustrates the transition between both regimes, at $V = \phi/e$. In the FN-regime, I is related to V by $I \propto V^2 exp(c/V)$, where $c < 0$ depends on the thickness and height of the barrier. Hence, plots of $ln(I/V^2)$ versus 1/V (FN-plots) yield a straight line with a negative slope, provided $V > \phi/e$. Beebe *et al.* took the approach to extend this way of plotting I-V data to low V. Interestingly, such FN-plots yield a well-defined minimum, at a voltage V_m. Intuitively, the existence of this minimum is easily understood. Since $I \propto V$ at low biases ($V \ll \phi/e$), an FN-plot of $ln(I/V^2) \propto ln(1/V)$ vs $1/V$ must yield a positive slope at low V (high $1/V$). At high biases, in the field emission regime, the slope is negative and thus a minimum appears in between. In fact, any I(V)-curve that evolves from linear to more than quadratic will have a minimum in a FN plot. Actually this is true for all the representations of the I-V characteristics of the form: $ln(I/V^\alpha)$ vs $1/V$ with $\alpha > 1$ [16]. Indeed for every α a minimum can be found, nevertheless we will concentrate in this chapter on the $\alpha = 2$ case.

Referring to the Simmons model, Beebe *et al.* suggest that: (i) V_m scales linearly with $\phi = E_F - E_{HOMO}$ (or $E_{LUMO} - E_F$, whichever level is closest); (ii) V_m is independent of molecular length d for constant ϕ; (iii) V_m equals the voltage at which there is a transition to the FN regime (hence 'transition voltage', see figure 4.1D) [5, 6]. Their striking experimental results substantiate these propositions. Measurements on self-assembled monolayers (SAMs) of a variety of conjugated molecules show that $V_m \propto E_F - E_{HOMO}$, where the latter difference is determined by photoelectron spectroscopy. Furthermore, they find V_m to be independent of molecular length, d, for alkanethiols. This is consistent with the fact that the HOMO-LUMO gap of these molecules is virtually length independent [6]. All these important observations make a strong case for TVS to become a general technique in molecular electronics.

We therefore start our study by investigating the Simmons model, put forward by Beebe *et al.*, in detail. Surprisingly, we find that it is in strong dis-

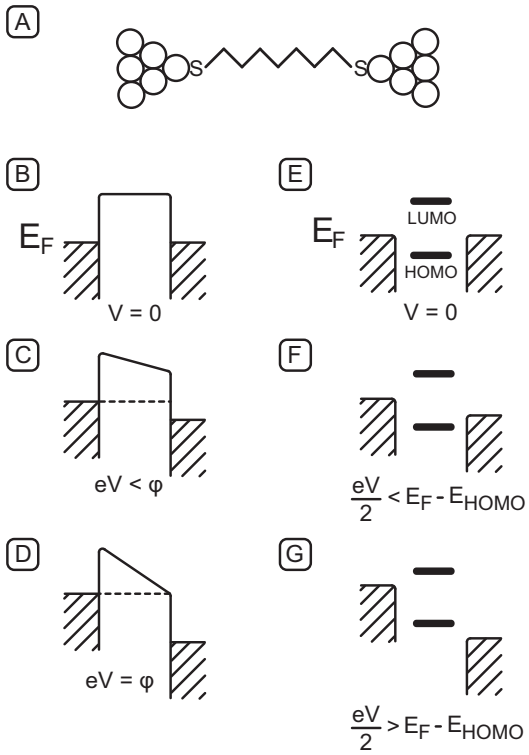

FIGURE 4.1: **Modeling a molecular junction. A** Molecular junction (thiol bonds). **B-D** Simmons model. Here, a molecule is depicted as a tunnel barrier of height ϕ and length d (**B**, for clarity we picture electron tunnelling only). Upon applying a bias voltage, the barrier is tilted (**C**). When $eV \geq \phi$, the barrier becomes triangular and electrons tunnel by field emission (**D**). **E-G**: resonant molecular model. Here, the molecular levels are broadened by the interaction with the electrodes (**E**). At elevated biases, the left and right chemical potentials open a window for transport of size eV (**F**). The current increases dramatically when a level is within the bias window (**G**, resonant tunnelling).

agreement with the experimental data in Refs. [5, 6]. To demonstrate this, we first make use of a simple, but rather accurate analytical model for tunnelling. This has the advantage that we can obtain a simple analytical expression for V_m. Subsequently, we confirm this result by using the full Simmons model numerically.

4.2 The Simmons model

To describe electron tunnelling in an elegant manner, we use a reformulation of Stratton's formula for direct tunnelling [17, 18]. This gives I(V)-curves of the form:

$$I \propto sinh(\frac{eV\tau}{\hbar}) \tag{4.1}$$

Here, $\tau = d\sqrt{m/2\phi}$ is the tunnel traversal time and m is the electron mass. Previously, a comparison between Simmons and Stratton was made by Hartman [19]. Due to the simple form of eq. 4.1, it is straightforward to determine an analytical expression for V_m. To find V_m, we put the derivative in a Fowler-Nordheim plot to zero. Substituting $y = 1/V$, we require:

$$\frac{dln(I/V^2)}{d1/V} = \frac{d}{dy}(ln(sinh(\frac{e\tau}{y\hbar})) + 2ln(y)) \tag{4.2}$$

$$= \frac{2}{y} - \frac{e\tau}{\hbar}\frac{1}{y^2}coth(\frac{e\tau}{\hbar y}) = 0. \tag{4.3}$$

Thus:

$$y_m = \frac{e\tau}{2\hbar}coth(\frac{e\tau}{\hbar y_m}) \tag{4.4}$$

By re-substituting $y_m = 1/V_m$, equation 4.5 is obtained.

$$\frac{1}{V_m} = \frac{e\tau}{2\hbar}coth(\frac{eV_m\tau}{\hbar}) \tag{4.5}$$

It is very instructive to discuss an approximate solution to eq. 4.5. For this, let us assume that $eV_m >> \hbar/\tau$, such that $coth(eV_m\tau/\hbar) = 1$. Then:

$$V_m \approx \frac{2\hbar}{e\tau} = \frac{2\hbar}{e\sqrt{m}}\frac{\sqrt{2\phi}}{d} \tag{4.6}$$

Before we discuss eq. 4.6, we check its validity by substituting it back into eq. 4.5. This yields $coth(e\tau V_m/\hbar) = coth(2) = 1.037$, so that eq. 4.6 is accurate within a few per cent.

Equation 4.6 is remarkably different from the results Beebe *et al.* obtained: (i) V_m is not proportional to the barrier height, but to its square root; (ii) V_m is not independent of the molecular length d, but inversely proportional to it; (iii) there is no general correspondence between V_m and the transition voltage at which a tunnel barrier becomes triangular (depicted in figure 4.1D). The latter voltage equals ϕ/e, independent of d, whereas eq. 4.6 yields $V_m \propto 1/d$.
Clearly, the Stratton approach is only an approximation. Nevertheless, eq. 4.6 turns out to have more general validity. To show this, we turn to the actual Simmons model. In our calculations, we include the integrals that are neglected in Ref. [12] itself. This prevents unphysical results for short and low barriers, a common problem in tunneling analysis (see appendix B). We proceed our discussion in the light of the most elaborate and convincing result Beebe *et al.* present. They perform TVS on a series of alkanethiol molecules with lengths ranging from 9 to 24 Å and find V_m = 1.2 V, almost independent of molecular length. Since alkanes have become a benchmark system in experimental transport studies, they form a perfect test bed for our present study as well [2, 3, 6, 13, 14, 20–24]. There is general agreement that $\phi = E_F - E_{HOMO}$ hardly changes with alkane length. However, for its precise value different numbers can be found in literature, even in the well-studied case of Au-S coupling [3, 13, 14]. In the following, we use ϕ = 4 eV [13]. For generality, however, all calculations presented below have also been performed for values, ϕ = 2.14 eV, taken from Ref. [14], and ϕ = 3 eV (see appendix B). The inset of Fig. 4.2a shows an I(V)-curve for a rectangular barrier with ϕ = 4 eV and d=10 Å, computed by the Simmons expression for the intermediate regime ($eV < \phi$). The corresponding FN-plot (main panel in figure 4.2a), exhibits a clear minimum around V_m = 1.5 V< ϕ/e. Thus, we have the tools at hand to test eq. 4.6 for the Simmons model. In figure 4.2b, we show V_m vs. $\sqrt{\phi}$ for a virtual series of ϕ-values, assuming constant length d = 10 Å. As anticipated above, we see that $V_m \propto \sqrt{\phi}$. Next, we plot V_m for a series of lengths d, with ϕ = 4 eV (see Fig. 4.2-C, blue line). Indeed, we find that $V_m \propto 1/d$. In fact, the Simmons result deviates very little from the line obtained using the Stratton approach (black in figure 4.2-C). We conclude that eq. 4.6 approximately holds for the Simmons model as well. Most importantly, however, these calculations confirm that there is a large discrepancy between data and model, as presented for TVS thus far [5, 6]. Hence, a new interpretation of TVS is due. Two different approaches can be considered for this. The first is to extend the Simmons model to include the image potential. The influence of the latter is that the effective barrier height ϕ decreases considerably [12, 13]. Since this effect is larger for shorter molecules, this may locally cancel the length dependence in eq. 4.6. Alternatively, we will consider a coherent transport picture based on molecular levels, Lorentz-

broadened by coupling to the leads. In that case, the voltage is assumed to drop fully at both metal-molecule contacts. This is in strong contrast with any type of tunnelling model, where the voltage drops evenly over the junction (see figure 4.1).

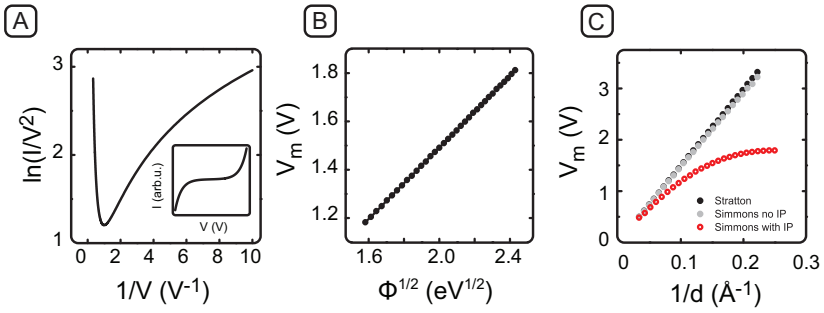

FIGURE 4.2: **Calculations on the length dependence of V_m according to Simmons.A**: Fowler-Nordheim plot for a barrier with ϕ=4eV and d= 10 Å, as predicted by the Simmons model. V_m is determined from the minimum of the graph. Inset: corresponding I(V)-curve on a linear scale. **B**: V_m versus $\sqrt{\phi}$ for the Simmons model (d=10 Å). The linear relation is consistent with eq. 4.6. **C**: V_m versus 1/d for $\phi = 4$ eV, using various tunnel models. Black: Stratton model (eq. 4.6). Light-gray: full Simmons model without image potential. Open circles: full Simmons model including image potential ($\epsilon_r = 2.1$). Clearly, V_m depends strongly on d in all cases.

For the calculations including the image potential, we used the full formulation of Simmons and eq. 35 of reference [12] with the correction of ref. [25] to calculate $\bar{\phi}$:

$$\bar{\phi} = \frac{1}{\Delta s}\int_{s_1}^{s_2}\{\phi_0 - \frac{eVx}{s} - \frac{1.15\lambda s^2}{x(s-x)}\}dx. \tag{4.7}$$

Here, $\lambda = e^2 ln2/8\pi\epsilon_r s$. For the local dielectric constant, we take $\epsilon_r = 2.1$ [26, 27]. s_1 and s_2 are the positions where the barrier is equal to the Fermi energy of the metal and were found numerically. Figure 4.2-C shows V_m as a function of $1/d$ (red line). For large d (small $1/d$), this result deviates little from the bare Simmons result. For smaller d, however, it differs considerably. In fact, a maximum in $V_m(d)$ is seen for larger values of $1/d$ than shown in figure 4.2-C, which indeed results from a decrease of the barrier height as the electrodes come closer to each other. Nevertheless, for the length scales that Beebe *et al.*

investigated (9 to 24 Å), V_m is still strongly dependent on d. Hence, we cannot explain the experimental data by including the image potential in a Simmons model. We note here that the Simmons model only presents a limited picture of tunnel barriers as pointed out in reference [28]. Besides we elaborated on the Simmons model to follow the reasoning of Beebe *et al.* and conclude that the model they present does not match their experimental results at all.

4.3 A COHERENT, MOLECULAR LEVEL MODEL

Let us therefore consider a more common picture of a molecular junction, as sketched in Fig. 4.1-E-G [29–33]. The molecular levels are located below (occupied) and above (empty) the Fermi energy of the metal contacts. Within the coherent Landauer approach, transport through such a junction is described by a transmission function T(E) that depends explicitly on energy. This function is peaked around the molecular levels. In fact, it has been extensively shown that a Lorentzian provides a good description for the transmission around a single molecular level [29, 30, 33]. Resonant tunneling can be achieved by applying the proper gate voltage in three-terminal junctions. In two-terminal devices, however, resonant tunneling is only possible by opening a voltage window eV high enough for the molecular level to fall in between the left and right chemical potentials (see figure 4.1-G). As discussed above, a device typically breaks down before this point is reached. Here, we will assume that one molecular level (HOMO) dominates transport, as is often the case in molecular junctions [5, 6, 14]. Thus our model captures the most relevant physics needed for an analysis of TVS. For T(E), this yields:

$$T(E) = \frac{\eta(1-\eta)\Gamma^2}{\Gamma^2/4 + (E-\varepsilon)^2} \tag{4.8}$$

where $\varepsilon = E_{HOMO}$ (we set $E_F = 0$). Furthermore, $\Gamma = \Gamma_1 + \Gamma_2$ denotes the total energy broadening due to the coupling between metal and electrodes. Specifically, $\Gamma_1 = \eta\Gamma$ and $\Gamma_2 = (1-\eta)\Gamma$ describe the overlap between the molecule and the left and right electrode, respectively. The parameter η denotes the asymmetry of the coupling. Symmetric coupling corresponds to $\eta = 0.5$. In that case, an applied voltage drops symmetrically at the left and right contacts (compare figures 4.1-D and 4.1-G). The I(V)-relationship can be calculated from the Landauer formula:

$$I = \frac{2e}{h}\int_{-\infty}^{\infty} T(E)[f_1(E) - f_2(E)]dE \tag{4.9}$$

Here, $f_{1,2}(E) = (exp((E-\mu_{1,2})/kT)+1)^{-1}$ is the Fermi function for a temperature T, at the left ($\mu_1 = eV/2$) and right ($\mu_2 = -eV/2$) electrode, respectively.

There is overwhelming experimental evidence that the zero-bias conductance of alkanes, as well as of many conjugated molecules, decreases exponentially with molecular length d. In general, one finds $dI/dV(V=0) \propto exp(-\beta d)$ where the decay constant β depends on the molecular series considered; β is highest for saturated molecules [1, 3, 34]. Interestingly, this result implies that also $T(E=E_F) \propto exp(-\beta d)$ (see eq.4.9). Indeed, several theory groups have confirmed such a relationship, using tight binding models in combination with (non-equilibrium) Green's function methods [31–33]. In our model, two free parameters exist, Γ and ε. In principle, both can depend on d. However, for longer alkanes, ε is known to be basically independent of d [13, 35]. Therefore, the length dependence must be in Γ. This has the immediate consequence that $\Gamma(d) \approx \frac{(E_F-\varepsilon)}{\sqrt{\eta(1-\eta)}} exp(-\beta d/2)$, using the fact that $E_F - \varepsilon >> \Gamma$ for longer alkanes. This relationship is consistent with extensive calculations by Samanta *et al.* for a series of oligophenyl molecules [33]. We note furthermore that Malen *et al.* applied a similar expression for $\Gamma(d)$ to successfully describe their experimental data [34]. Upon substituting $\Gamma(d)$ in eq. 4.8, a length dependent transmission function is obtained:

$$T(E,d) = \frac{1}{\frac{1}{4\eta(1-\eta)} + (\frac{E-\varepsilon}{E_F-\varepsilon})^2 exp(\beta d)} \tag{4.10}$$

Combining eqs. 4.9 and 4.10, we can calculate I(V)-curves for a series of molecular lengths and determine V_m. To compare to experimental data on alkanethiols, we take T= 300 K, $\varepsilon = -4$ eV and $\beta = 0.74$ Å^{-1} from extended literature [3]. Figure 4.3-A shows T(E) for several alkane lengths, whereas the inset of Fig. 4.3-B displays the corresponding FN plots. The length dependence of V_m is given in the main panel of Fig. 4.3-B. Remarkably, V_m is independent of molecular length for $d > 8$ Å. This is fully in agreement with the data of Beebe *et al.*, who find V_m to be independent of length for alkanes longer than 9 Å [6]. We note in addition that we find $V_m \propto \phi$ for a range of realistic values of ϕ (see figure 4.4).

We come to the important conclusion that TVS does indeed give us direct information on the molecular levels, as Beebe *et al.* have suggested. However, the interpretation of TVS only works within the framework of a coherent molecular transport model. Simmons-like pictures are inconsistent with experiments on molecular junctions.

4.4 Tunnel barrier or molecular levels?

Before we discuss further consequences of this conclusion, we take a critical look at figure 4.3. Despite the qualitative agreement, the value of V_m

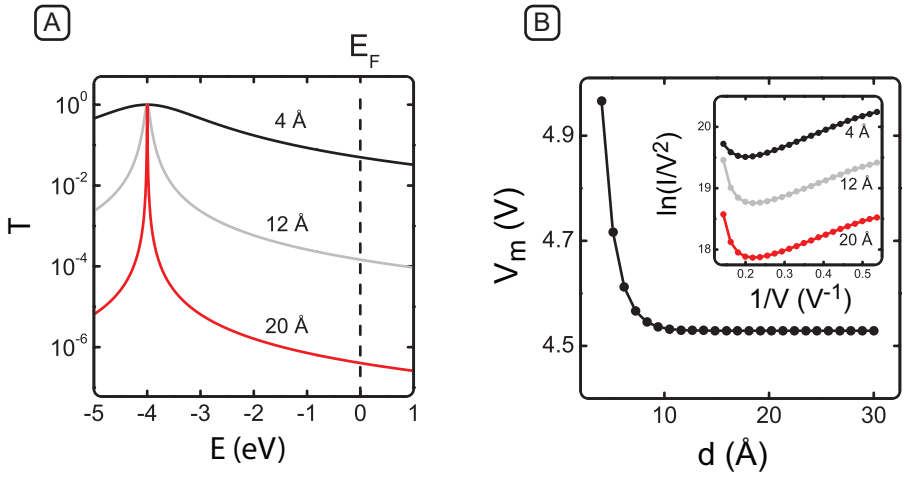

FIGURE 4.3: **Resonant molecular transport model applied to alkane junctions. A** Transmission function for three different lengths ($\varepsilon = -4$ eV, $T = 300$ K and $\beta = 0.74$Å [3]). **B** V_m versus molecular length d. V_m becomes length independent for $d > 8$ Å, consistent with the experiments by Beebe *et al.* [5, 6]. Inset: FN plots for the junctions in **A**.

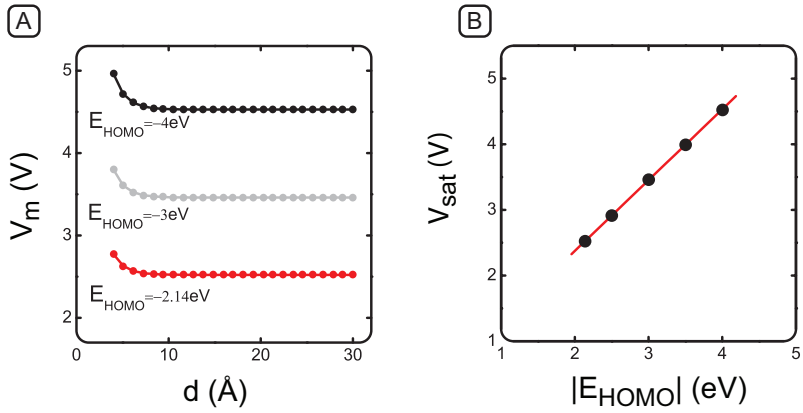

FIGURE 4.4: **Calculations on the length dependence of V_m for different E_{HOMO} values.A** V_m calculated using our coherent level model for several positions of the HOMO. For $d > 9$Å, V_m saturates to a value V_{sat} **B** Plot demonstrating that V_{sat} scales linearly with the position of the molecular HOMO level.

predicted by the model is much higher than found in experiment (though much lower than the resonant value $V = 2\phi/e$). This can have several reasons. First, $E_F - E_{HOMO}$ may be considerably smaller than 4 eV. As discussed above, there is quite some spread in the literature. Furthermore, the influence of image charges on molecular energy levels needs to be considered again. Just like in the Simmons case, the image force may yield a much lower level spacing for doubly contacted molecules as compared to free molecules. This phenomenon has recently attracted considerable theoretical attention [36–39]. Finally, although our Lorentzian model does capture the basic physics behind molecular transport, more detailed transport calculations will be needed to fully interpret TVS. Such studies should include the geometrical and electronic details of the molecular junction. For example, it was shown that the exact adsorption geometry of the molecule on the electrode has a pronounced effect on the shape of the transmission spectrum [14]. Recently, Mirjani *et al.* as well as Chen *et al.* presented in ref. [16, 40] a more detailed theoretical approach to the problem. Through their extended calculations they show, among other things, that our simple approach captures the essential physics involved. We will discuss this work in more details below.

To finalize our discussion, let us return to Figures 4.2 and 4.3. Clearly, the results for a coherent molecular model are radically different from those obtained for various Simmons models. There are two reasons for this. First, of course, the mathematics behind both models is not the same. Second, and perhaps more fundamental, the voltage profile is radically different. In the Simmons model, the potential decreases linearly with distance, whereas in the 'molecular' model, the voltage drops at the contacts only (see figure 4.1). It is easily visualized that the latter will result in a negligible length dependence of the shape of the I(V)-curves and thus in V_m being virtually independent of d. Interestingly, the very different properties of both models provide a fascinating perspective: TVS may allow us to distinguish molecular junctions (V_m independent of d) from tunnel junctions without molecules ($V_m \propto \frac{1}{d}$). Perhaps surprisingly, such a tool is still generally lacking in (two-terminal) molecular transport. As shown above, the data by Beebe *et al.* can only be understood within a 'molecular' model. Inversely, this can also be seen as evidence for the fact that they did indeed probe a molecular system. We note that such a distinction is not possible within the framework Beebe *et al.* present. If TVS in molecular junctions is explained by the Simmons model, there is no difference in the length dependence between a molecular junction with $E_F - E_{HOMO} = 4$ eV and a vacuum barrier with $\phi = 4$ eV, except in the image force via ϵ_r. Clearly, a tunnel junction without molecules will obey Simmons characteristics, resulting in $V_m(d, \phi)$ relations like in figure 4.2. To test this proposition, we performed a

series of experiments to consistently compare molecular junctions with tunnel junction for various lengths.

4.5 EXPERIMENTS ON VACUUM TUNNEL JUNCTIONS AND ORGANIC MOLECULES

Here we present extensive TVS measurements on: i) metal-vacuum-metal junctions[1] and ii) molecular junctions (more details in chapter 5) to test experimentally the propositions made above. Moreover we also include the results on molecular junctions from the literature.
In order to reveal the basic properties of TVS we need the possibility to accurately vary the tunnel gap between the electrodes. For a full characterization of TVS on a metal-vacuum-metal junction, voltages up to 3 V are to be applied over vacuum gaps as small as ≈0.3 nm. Such high electric fields (and high field gradients) may cause instabilities in the tunnel junctions. Hence, junctions are needed which are stable in time and kept in a clean environment. For this reason we used notched-wire mechanically controllable break junctions in cryogenic vacuum (T≈ 5 K) [41]. The electrodes are made of gold, the archetypical electrode metal for molecular junctions. In addition, the junctions were first optimized by a "training" procedure, i.e. by repeatedly opening and closing the electrodes [42]. We expect that this organizes the apex atoms into their strongest bond configuration and enhances their stability in high electric fields. The high stability and repeatability of the conductance evolution is illustrated by the tunnel curve in figure 4.5-A. Upon closing, the tunnel current increases exponentially until the electrodes snap to contact [42, 43]. Note that the conductance jumps to a value close to 1 G_0 ($1G_0 = 2e^2/h$), indicating a clean single-atom contact. After the training procedure, the electrodes are separated such that a vacuum gap is created with a zero bias conductance of ≈0.01 G_0. This is the starting point for the TVS measurements. Subsequently, the vacuum gap is increased stepwise, and an I-V curve over the range ±2-3 V is recorded for each position.

A typical example of such an I-V curve is plotted in figure 4.5-B. Clearly, the current displays a transition from a linear dependence at low voltages to a strongly nonlinear behavior for voltages $> 1.5V$. As stated earlier, this transition can be quantified by scaling the data in a Fowler-Nordheim representation. This is shown in figure 4.5-C, here for positive bias voltage only. Let us first discuss the upper curve. This curve is measured for a small tunnel gap with a

[1] The MCBJ vacuum tunnelling experiments have been performed by Marius Trouwborst and Tim Baart

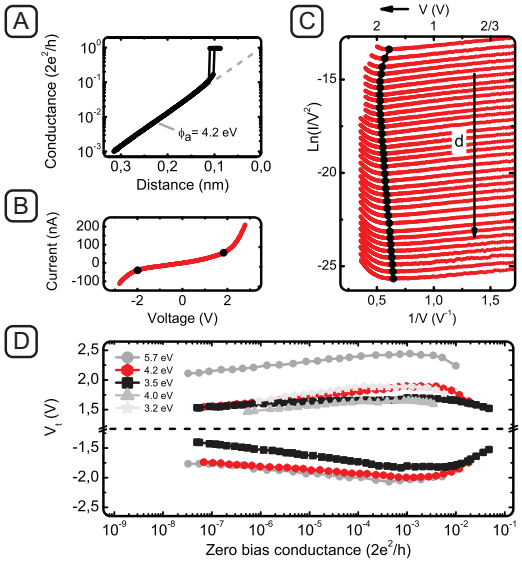

FIGURE 4.5: **Electrical characteristics of clean gold junctions at T≈ 5 K. A** Conductance versus width of the vacuum gap of a trained junction at a bias voltage of V = 100 mV. From the exponential decay at large distance, an apparent barrier height is deduced of 4.2 ± 1.0 eV (eq. 4.1) [44, 45]. **B** Typical I-V curve in the tunneling regime. Here, V_m is -1.99 V for negative voltage and 1.84 V for positive voltage (black dots), as obtained from: **C** Fowler-Nordheim plot of the I-V characteristics for 34 different positions. After each curve the electrode separation is increased by 0.02 nm, resulting in a lower current (no offset is used). The black dots represent the minima, or V_m. Remarkably, V_m decreases with distance for wide tunnel barriers while it increases for short tunnel barriers. **D** V_m versus zero bias conductance for different contacts, measured on 3 different samples. Note the break in the scale between -1.2 V and +1.2V. The two curves marked by triangles and stars are measured on the same sample, but the latter was obtained after modifying the electrodes. The same holds for the two curves marked by squares and hexagons. For each contact, the apparent barrier height was measured and its value is given next to the data points ($\pm$ 1 eV).

zero bias conductance of ≈0.02 G_0. It has a well-defined minimum at 1.64 V that determines V_m. In total, 34 curves are plotted, corresponding to 34 different electrode separations (equally spaced by ≈0.02 nm). When we increase the electrode separation, a shift in V_m can be observed. The transition voltage first increases with distance and is at a maximum after stretching by ≈0.1 nm (fifth curve). V_m has now increased to 1.9 V. For even larger gaps V_m decreases again to a value of 1.55 V after stretching by ≈0.6 nm. In order to directly compare our measurements to the predictions of eq. 4.6, we need to plot the data as a function of $1/d$. For this purpose, the origin in the position ($d = 0$) was defined by extrapolating the exponential part of figure 4.5-A (dashed line) to a conductance of $2e^2/h$. The crossing point is then set as the origin. As a result we obtain figure 4.6. There is a striking difference when comparing the experimental data and the straight line expected from eq. 4.6: our data are not proportional to $1/d$. Instead, only a modest variation with d is found, with a maximum at ≈ 3 nm^{-1}. Clearly, the square barrier model (with a constant height ϕ) does not give an accurate description of the data. Qualitatively, the curves are very similar to the Simmons curves with image potential included, as shown in figure 4.2-C. However, we have to be careful not to apply this model quantitatively, since experimentally, we have atomically sharp electrodes. The Simmons model assumes two parallel plates. Let us first discuss the implications of our data for

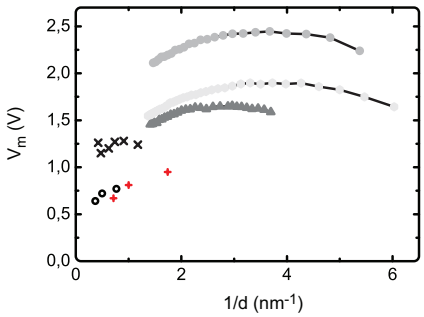

FIGURE 4.6: **Variation of the transition voltage with electrode distance.** Filled symbols: measurements of V_m vs $1/d$ for 3 different gold samples in vacuum. "×" and "+": data from large-area molecular junctions as reported by Beebe *et al.* "×": Alkane series, C_{18}-SH, C_{16}-SH, C_{12}-SH, C_{10}-SH, C_8-SH, and C_6-SH. "+": phenyl series, TP-SH, BP-SH, and Ph-SH [6]. "o": data presented in chapter 5 for OPEs of different length (OPE2DT, OPE3DT and OPE4DT) measured with C-AFM.

the interpretation of TVS. As described before, we want to make a comparison between the distance dependence of V_m for vacuum junctions and molecular

junctions. For this purpose, we also include three data sets measured by Beebe *et al.* and in chapter 5 in figure 4.6 [6]. The upper data set ("×"), corresponding to alkanethiols of different lengths, has a negligible variation in V_m. This was ascribed to an almost constant HOMO-LUMO gap for different alkane lengths. The lower data set ("+" and "o") corresponds to $\pi-$conjugated phenylene (from reference [6]) and phenylethynylene molecules (chapter 5) respectively. Compared to the alkanethiols, these molecules have a stronger dependence of V_m on d. This was attributed to a variation in the HOMO-LUMO gap, which is expected to decrease with increasing molecule length. Let us now compare the measurements. The two types of data (molecular junctions and vacuum junctions) have been measured at slightly different distances. In contrast to our MCBJ measurements, the experiments of Beebe *et al.* were carried out on large-area junctions, in which many molecules are probed in parallel. In addition, the distance between the Fermi level and the nearest molecular level is lower than the work function of the electrodes. As a result, the conductance is larger for the large-area molecular junctions which makes it possible to measure at larger distances or smaller values of $1/d$, respectively. Nevertheless, we find that the distance dependence of V_m for the molecular data does not differ significantly from that observed in our vacuum measurements. This is an important conclusion of this chapter. Taking into account (i) the measurement accuracy of the molecular data of approximately $\pm$100 mV and (ii) the limited variation of V_m with d for the vacuum data, it is not possible to distinguish molecular junctions from vacuum junctions just by measuring the distance dependence of V_m. However, considering the absolute values of V_m for conjugated molecules there is a clear difference with the vacuum data. For conjugated molecules, the reported values for V_m are much lower (0.6 V to 1 V) than the values found for the vacuum junctions (> 1.4 V) [16].

4.6 Does TVS have a future?

We mentioned in this chapter the possibility to use the distance dependence of V_m to discern molecular junctions from empty tunnel barrier junctions. Indeed we predict a $1/d$ dependence for a tunnel junction and a much shallower dependence for organic molecules. In contrast we show in our measurements on a tunnel barrier with a varying size, a length dependence that is strongly deviating from the predicted $1/d$ relation. The relation between V_m and the electrode separation d is somewhat similar for a tunnel barrier and a molecular junction. Hence it is difficult to make a distinction between those two types of junctions based on $V_m(d)$. What is striking here is the lack of agreement to describe a simple tunnel junction, although on the nanometer scale, with

standard models for tunnel barriers. Although, the Simmons model including images charges can describe the observed relation ($V_m(d)$) qualitatively, its intended use is for tunneling between two parallel plates and not for two sharp atomic sized electrodes. Here lies still a challenge for theoreticians.
In this chapter we identified several possible applications for TVS. Its original purpose is to access molecular levels without the need for the high voltages required for resonant tunneling. We show in this chapter that first of all TVS for molecular junctions can not be described by a tunnel barrier model like the Simmons model, as originally proposed by Beebe *et al.*. Nonetheless we can qualitatively reproduce the experimental results from reference [6] based on a simple resonant transport model. In this case it appears that indeed V_m is proportional to the position of the molecular level (HOMO or LUMO). Although this is confirmed by more elaborated calculations [16, 46, 47], this is the specific case of alkanethiols, where the HOMO/LUMO position is independent on the molecular length [3, 13, 14]. Unfortunately this approach is too simplistic for π-conjugated molecules, where the HOMO-LUMO gap decreases with molecular length [31, 33, 47]. So, to make a quantitative analysis of the molecular level positions, we need to take into account more parameters like the junction (a)symmetry, the number of levels involved and most importantly the potential profile of the junction[16, 47]. In our simple Lorentzian model we place the voltage drop at the contacts only and thus no voltage drop over the molecule itself is taking place, logically resulting in the distance independence observed. Mirjani *et al.* demonstrate with a more elaborated model [40] that the voltage drop over the molecule is crucial [47]. Their main result is presented in figure 4.7 where the value $\chi = |E_F - E_{level}|/V_m$ is plotted as a function of molecular length for the voltage dropping over the molecule and no voltage drop at all. The parameter χ is better suited than V_m to appreciate the performance of TVS. Indeed $E_F - E_{level}$ is dependent on the molecular length, χ circumvents this dependence. Here, in figure 4.7, we consider the two extreme cases, in reality the voltage drop is lying somewhere in between. i) When no voltage is dropping over the molecule, χ is rather constant. ii) When the voltage is dropping entirely over the molecule, we observe a clear dependence of χ on d. Though this is theoretically easily tuned, experimentally determining the exact potential profile over such a junction is quite challenging.

Moreover in order to explore the HOMO or LUMO level with TVS one must consider two unknowns, χ and the (a)symmetry [16, 47, 48]. The (a)symmetry can be determined experimentally out of the I(V) characteristics (see chapter 5). However χ remains experimentally difficult to access. Hence, TVS alone is not enough to explore the molecular energy levels without extra knowledge on the studied junction.

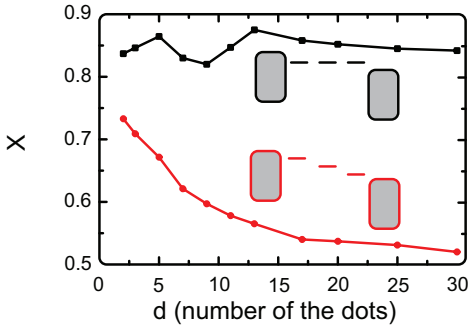

FIGURE 4.7: $\chi = |E_F - E_{level}|/V_m$ **versus the length of the molecule.** The calculations are done for the case where the voltage drop is only at the contacts (black squares) like schematically depicted in the higher inset and for the case the voltage drop is entirely over the molecule (circles) like shown in the lower inset. Taken from reference [47].

4.7 CONCLUSIONS

In this chapter we discussed a novel method for the analysis of current-voltage characteristics. Indeed transition voltage spectroscopy (TVS) held the promise of accessing molecular levels without the high voltages required just by replotting the I(V) curves as $ln(I/V^2)$ vs $1/V$ that will yield a minimum V_m. So V_m indicates the transition from a linear I(V) relation to a more than quadratic one, reducing the I(V) to a single number V_m.

We showed in this chapter that it is experimentally very challenging to extract information on the position of the molecular levels from TVS measurements. Indeed exact knowledge of both the junction symmetry and its potential profile are needed to relate the value of V_m to the energy of the HOMO (or LUMO). Experimentally we can deduce the symmetry of the junction from the I(V) curves, whereas determining the potential profile over a junction is still a challenge. At best a qualitative study of the molecular levels can be accomplished with TVS.

Moreover we demonstrated experimentally that V_m for a nanometer scale

tunnel junction behaves similarly to V_m for a molecular junction when varying the length of the junction. Nonetheless, the absolute value of V_m is lower for lower barriers or conjugated molecules. So it is not possible to unambiguously decide whether a junction is empty or populated by molecules, based on the value of V_m or its behaviour with length $V_m(d)$.

All in all, despite the appealing promises, TVS appears not to be an easily applicable tool for molecular electronics. Nonetheless it is still a potential system to test more advanced tunnel barrier models [28].

References

[1] N. J. Tao, *Electron transport in molecular junctions*, Nature Nanotechnology **1**, 173 (2006).

[2] S. Lindsay and M. Ratner, *Molecular Transport Junctions: Clearing Mists*, Advanced Materials **19**, 23 (2007).

[3] H. B. Akkerman and B. de Boer, *Electrical conduction through single molecules and self-assembled monolayers*, Journal Of Physics-Condensed Matter **20** (2008).

[4] M. S. Hybertsen, L. Venkataraman, J. E. Klare, A. CWhalley, M. L. Steigerwald, and C. Nuckolls, *Amine-linked single-molecule circuits: systematic trends across molecular families*, Journal Of Physics-Condensed Matter **20** (2008).

[5] J. M. Beebe, B. Kim, J. W. Gadzuk, C. D. Frisbie, and J. G. Kushmerick, *Transition from direct tunneling to field emission in metal-molecule-metal junctions*, Physical Review Letters **97** (2006).

[6] J. M. Beebe, B. Kim, C. D. Frisbie, and J. G. Kushmerick, *Measuring relative barrier heights in molecular electronic junctions with transition voltage spectroscopy*, ACS Nano **2**, 827 (2008).

[7] L. H. Yu, N. Gergel-Hackett, C. D. Zangmeister, C. A. Hacker, C. A. Richter, and J. G. Kushmerick, *Molecule-induced interface states dominate charge transport in Si-alkyl-metal junctions*, Journal of Physics: Condensed Matter **20**, 374114 (2008).

[8] K. Liu, G. R. Li, X. H. Wang, and F. S. Wang, *Length dependence of electron conduction for oligo(1,4-phenylene ethynylene)s: A conductive probe-atomic force microscopy investigation*, Journal of Physical Chemistry C **112**, 4342 (2008).

[9] B. F. C. Choi, S.H.; Kim, *Electrical Resistance of Long Conjugated Molecular Wires*, science **320**, 1482 (2008).

[10] G. Wang, T.-W. Kim, G. Jo, and T. Lee, *Enhancement of Field Emission Transport by Molecular Tilt Configuration in Metal-Molecule-Metal Junctions*, Journal of the American Chemical Society **131**, 5980 (2009).

[11] S. A. DiBenedetto, A. Facchetti, M. A. Ratner, and T. J. Marks, *Charge Conduction and Breakdown Mechanisms in Self-Assembled Nanodielectrics*, Journal of the American Chemical Society **131**, 7158 (2009).

[12] J. G. Simmons, *Generalized Formula For Electric Tunnel Effect Between Similar Electrodes Separated By A Thin Insulating Film*, Journal Of Applied Physics **34**, 1793 (1963).

[13] H. B. Akkerman, R. C. G. Naber, B. Jongbloed, P. A. van Hal, P. W. M. Blom, D. M. de Leeuw, and B. de Boer, *Electron tunneling through alkanedithiol self-assembled monolayers in large-area molecular junctions*, Proceedings Of The National Academy Of Sciences Of The United States Of America **104**, 11161 (2007).

[14] C. Li, I. Pobelov, T. Wandlowski, A. Bagrets, A. Arnold, and F. Evers, *Charge transport in single Au/alkanedithiol/Au junctions: coordination geometries and conformational degrees of freedom.*, Journal of the American Chemical Society **130**, 318 (2008).

[15] L. Fowler, R. H.; Nordheim, Proc. Roy. Soc. **119**, 173 (1928).

[16] J. Z. Chen, T. Markussen, and K. S. Thygesen, *Quantifying transition voltage spectroscopy of molecular junctions: Ab initio calculations*, Physical Review B **82**, 121412 (2010).

[17] R. Stratton, *Volt-current Characteristics For Tunneling Through Insulating Films*, Journal of Physics and Chemistry of Solids **23**, 1177 (1962).

[18] A. Bezryadin, C. Dekker, and G. Schmid, *Electrostatic trapping of single conducting nanoparticles between nanoelectrodes*, Applied Physics Letters **71**, 1273 (1997).

[19] T. Hartman, *Tunneling through asymmetric barriers*, Journal of Applied Physics **35**, 3283 (1964).

[20] W. Haiss, S. Martin, L. E. Scullion, L. Bouffier, S. J. Higgins, and R. J. Nichols, *Anomalous length and voltage dependence of single molecule conductance*, Physical Chemistry Chemical Physics **11**, 10831 (2009).

[21] L. Venkataraman, J. E. Klare, C. Nuckolls, M. S. Hybertsen, and M. L. Steigerwald, *Dependence of single-molecule junction conductance on molecular conformation*, Nature **442**, 904 (2006).

[22] M. T. Gonzalez, S. M. Wu, R. Huber, S. J. van der Molen, C. Schonenberger, and M. Calame, *Electrical conductance of molecular junctions by a robust statistical analysis*, Nano Letters **6**, 2238 (2006).

[23] C. A. Martin, D. Ding, H. S. J. van der Zant, and J. M. van Ruitenbeek, *Lithographic mechanical break junctions for single-molecule measurements in vacuum: possibilities and limitations*, New Journal of Physics **10**, 065008 (2008).

[24] E. H. Huisman, M. L. Trouwborst, F. L. Bakker, B. de Boer, B. J. van Wees, and S. J. van der Molen, *Stabilizing Single Atom Contacts by Molecular Bridge Formation*, Nano Letters **8**, 3381 (2008).

[25] J. G. Simmons, *Potential Barriers and EmissionLimited Current Flow Between Closely Spaced Parallel Metal Electrodes*, Journal Of Applied Physics **34**, 2472 (1964).

[26] B. de Boer, H. Meng, D. F. Perepichka, J. Zheng, M. M. Frank, Y. J. Chabal, and Z. Bao, *Synthesis and Characterization of Conjugated Mono- and Dithiol Oligomers and Characterization of Their Self-Assembled Monolayers*, Langmuir **19**, 4272 (2003).

[27] L. Bernard, Y. Kamdzhilov, M. Calame, S. J. van der Molen, J. Liao, and C. Schönenberger, *Spectroscopy of Molecular Junction Networks Obtained by Place Exchange in 2D Nanoparticle Arrays*, journal of physical chemistry C **111**, 18445 (2007).

[28] I. Baldea and H. Koppel, *Transition voltage spectroscopy: a challenge for vacuum tunneling models at nanoscale*, arXiv:1107.3501v1 [cond-mat.mes-hall] (2011).

[29] M. Paulsson and S. Datta, *Thermoelectric effect in molecular electronics*, Physical Review B **67**, 241403 (2003).

[30] J. M. Thijssen and H. S. J. Van der Zant, *Charge transport and single-electron effects in nanoscale systems*, Physica Status Solidi B-Basic Solid State Physics **245**, 1455 (2008).

[31] M. R. M. Mujica, V.; Kemp, *Electron conduction in molecular wires. II. application to scanning tunneling microscopy*, J. Chem. Phys. **101**, 6856 (1994).

[32] C. Joachim and J. F. Vinuesa, *Length dependence of the electronic transparence (conductance) of a molecular wire*, Europhysics Letters **33**, 635 (1996).

[33] M. P. Samanta, W. Tian, S. Datta, J. I. Henderson, and C. P. Kubiak, *Electronic conduction through organic molecules*, Physical Review B **53**, R7626 (1996).

[34] J. A. Malen, P. Doak, K. Baheti, T. D. Tilley, R. A. Segalman, and A. Majumdar, *Identifying the Length Dependence of Orbital Alignment and Contact Coupling in Molecular Heterojunctions*, Nano Letters **9**, 1164 (2009).

[35] D. M. Alloway, M. Hofmann, D. L. Smith, N. E. Gruhn, A. L. Graham, R. Colorado, V. H. Wysocki, T. R. Lee, P. A. Lee, and N. R. Armstrong, *Interface Dipoles Arising from Self-Assembled Monolayers on Gold UV Photoemission Studies of Alkanethiols and Partially Fluorinated Alkanethiols*, The Journal of Physical Chemistry B **107**, 11690 (2003).

[36] K. Kaasbjerg and K. Flensberg, *Strong Polarization-Induced Reduction of Addition Energies in Single-Molecule Nanojunctions*, Nano Letters **8**, 3809 (2008).

[37] J. D. Sau, J. B. Neaton, H. J. Choi, S. G. Louie, and M. L. Cohen, *Electronic energy levels of weakly coupled nanostructures C(60)-metal interfaces*, Physical Review Letters **101**, 026804 (2008).

[38] P. Hedegård and T. Bjørnholm, *Charge transport through image charged stabilized states in a single molecule single electron transistor device*, Chemical Physics **319**, 350 (2005).

[39] K. S. Thygesen and A. Rubio, *Renormalization of Molecular Quasiparticle Levels at Metal-Molecule Interfaces Trends across Binding Regimes*, Physical Review Letters **102**, 046802 (2009).

[40] F. Mirjani and J. M. Thijssen, *Density functional theory based many-body analysis of electron transport through molecules*, Physical Review B **83**, 035415 (2011).

[41] N. Agrait, A. L. Yeyati, and J. M. van Ruitenbeek, *Quantum properties of atomic-sized conductors*, Physics Reports-Review Section Of Physics Letters **377**, 81 (2003).

[42] M. L. Trouwborst, E. H. Huisman, F. L. Bakker, S. J. van der Molen, and B. J. van Wees, *Single Atom Adhesion in Optimized Gold Nanojunctions*, Physical Review Letters **100**, 175502 (2008).

[43] C. Untiedt, M. J. Caturla, M. R. Calvo, J. J. Palacios, R. C. Segers, and J. M. van Ruitenbeek, *Formation of a Metallic Contact: Jump to Contact Revisited*, Physical Review Letters **98**, 206801 (2007).

[44] A. Yanson, G. Rubio Bollinger, H. van den Brom, N. Agraït, and J. van Ruitenbeek, Nature **395**, 783 (1998).

[45] C. Untiedt, A. Yanson, R. Grande, G. Rubio-Bollinger, N. Agrait, S. Vieira, and J. van Ruitenbeek, *Calibration of the length of a chain of single gold atoms*, Physical Review B **66** (2002).

[46] M. Araidai and M. Tsukada, *Theoretical calculations of electron transport in molecular junctions: Inflection behavior in Fowler-Nordheim plot and its origin*, Physical Review B **81**, 235114 (2010).

[47] F. Mirjani, J. M. Thijssen, and S. J. van der Molen, *Advantages and limitations of transition voltage spectroscopy: A theoretical analysis*, Physical Review B **84**, 115402 (2011).

[48] T. Markussen, J. Chen, and K. S. Thygesen, *Improving transition voltage spectroscopy of molecular junctions*, Physical Review B **83**, 155407 (2011).

5

Conductance properties of a series of OPE molecules

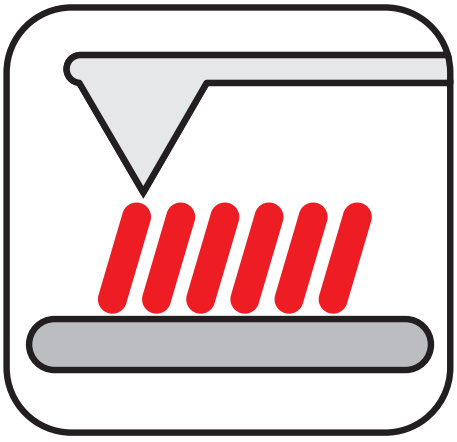

In this chapter we present charge transport measurements on a series of organic molecules with different lengths composed of identical building blocks. The synthesized oligo-phenyl-ethynylene (OPE) molecules are investigated both in their dithiolated and monothiolated form. We perform our experiments using a conducting probe atomic force microscope (C-AFM). Those measurements enable us to scrutinize two important concepts in molecular electronics. (i) The length dependence of molecular conductance. (ii)Transition voltage spectroscopy (TVS).

5.1 Introduction

The relation between chemical structure and charge transport properties is at the heart of molecular electronics. Hence, to understand the physics behind it, experiments have been conducted that vary the chemical structure of the molecules as well as the methodology to extract information from the obtained data. From the start, the length dependence of conductance has enjoyed large attention in field of molecular electronics[1, 2]. Indeed, quickly, the analogy with a tunnel junction was made, as the conductance was found to be exponentially dependent on length, resulting in the expression of this length dependence in the so called β-factor, the exponential decay constant. Furthermore this length dependence has been measured in a wide variety of devices resulting in a wide range of β-values[2]. Therefore it has become a popular benchmark to validate new measuring methods[3, 4]. Still the β-factor is an ill defined concept in molecular junctions as we will point out later on.

5.2 Experimental details

The chemical structure of the molecules, synthesized by Hennie Valkenier at Groningen university [5], used in this work are presented in figure 5.1. Self-Assembled Monolayers (SAMs) of the acetyl-protected mono- and dithiols were grown from solutions with triethylamine as deprotecting agent, which promotes the formation of high-quality and densely-packed SAMs[6]. These SAMs were grown from 0.5 mM solutions in THF (anhydrous) with 10% (v/v) triethylamine (Fisher, HPLC grade, degassed) added. All solutions and SAMs were prepared inside a glovebox filled with nitrogen (<5 ppm O_2)[1]. We used freshly prepared samples of 150 nm gold on mica for the ellipsometry and XPS studies, and freshly prepared samples of 5 nm chromium and 200 nm gold thermally deposited on a silicon wafer for the CP-AFM studies. Samples were immersed upside down for two nights in about 3 mL solution. After this immersion time,

[1]The SAM's are prepared by Hennie Valkenier at the University of Groningen

the samples were taken from solution, rinsed three times with clean THF, and dried under the nitrogen atmosphere in the glovebox. Conducting atomic force

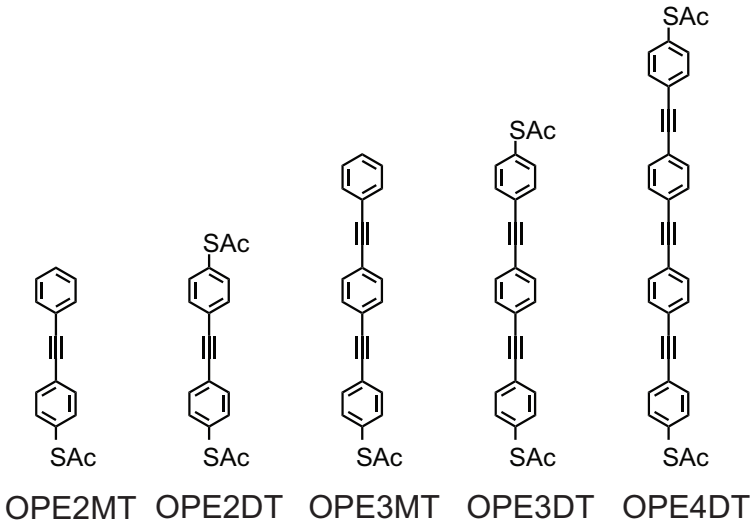

FIGURE 5.1: **Chemical structure of the molecules measured.** The oligo (phenylene ethynylene) (**OPE**) series here shown in which the length of the OPE molecules increases with one phenylene ethynylene unit per molecule (**2**,**3** and **4** rings). In addition to that each OPE is found in a dithiloated form (**DT**) and a monothiolated from (**MT**) both acetyl protected.

microscopy (C-AFM) is performed on a commercial AFM (Digital Instrument). A Multimode AFM base is used in combination with a Nanoscope IIIa controller and Nanoscope V6r13 software. The conductance measurements are performed in contact mode i.e. the feed-back is done on the deflection set point in order to apply a force of typically 2 nN on the SAM. During the conductance measurements the scanning is disabled. The AFM cantilevers used are NP-10 (Veeco) of type B ($f_0 = 14 - 26$ kHz and $k = 0.12N/m$). The SiN AFM tips are coated by sputtering with MoGe (4nm) as an attachment layer and subsequently with 80 nm of Au. A scanning electron micrograph of a typical cantilever is shown in figure 5.2 The electrical measurements are controlled by a labview program and interfaced by a 16 bit NI data acquisition card. The substrate carrying the SAM is biased while the tip is grounded. While the bias voltage is swept (typically from 0 V to -1 V to 1 V and back to 0 V) the current is recorded at a sampling rate of 10 kHz and 1000 points are taken per curve. To do so the current is amplified using a Femto DLPCA-200 variable gain current amplifier. For each

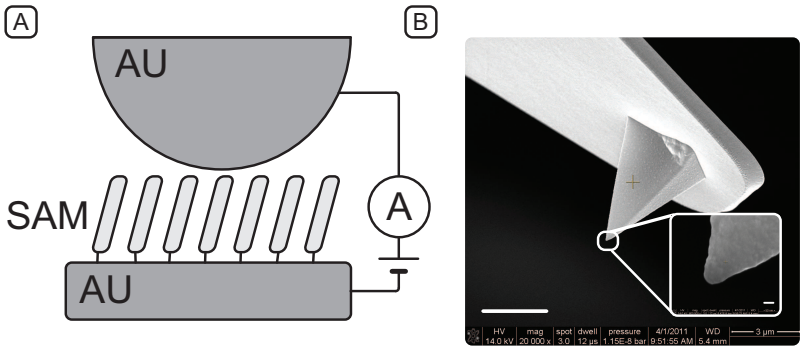

FIGURE 5.2: **SEM picture of a C-AFM cantilever.** SEM picture of a AFM cantilever coated with 4nm MoGe and 80 nm Au. The scale bar is 3μm and 50 nm for the inset.

measurement spot 100 to 1000 I(V)-curves are recorded, for each sample 2 to 8 spots are probed.

Subsequently the I(V) curves are smoothed with a local regression using weighted linear least squares and a 2nd degree polynomial model. Next we take a numerical derivative of the current relative to the voltage (dI/dV). Finally we construct a 2D histogram of these dI/dV values by logarithmically binning them for each bias voltage and plotting them next to each other. This will result in a 3D graph with on the x-axis the bias voltage, on the y-axis the log (dI/dV) and on the z-axis (in colour scale) the number of counts. Such a 2D histogram can be seen as a collection of traditional 1D conductance histograms for different bias voltages. In figure 5.3 we show such a 2D histogram with the related cross-section 1D histograms, taken at various bias voltages, to illustrate this method of plotting our data.

This representation enables us to distinguish general tendencies in dI/dV-curves from statistical variations in the conductance values themselves. In addition to that such plots represent the whole dataset ($\approx$ 2000 traces) at once without the need of data selection or further processing. Indeed this is a recurrent problem in molecular electronics, how to deal with the large variation conductance values? Selecting data [7–9], leads to a biased view of the results depending on the criteria used. Indeed the selection is not always based on

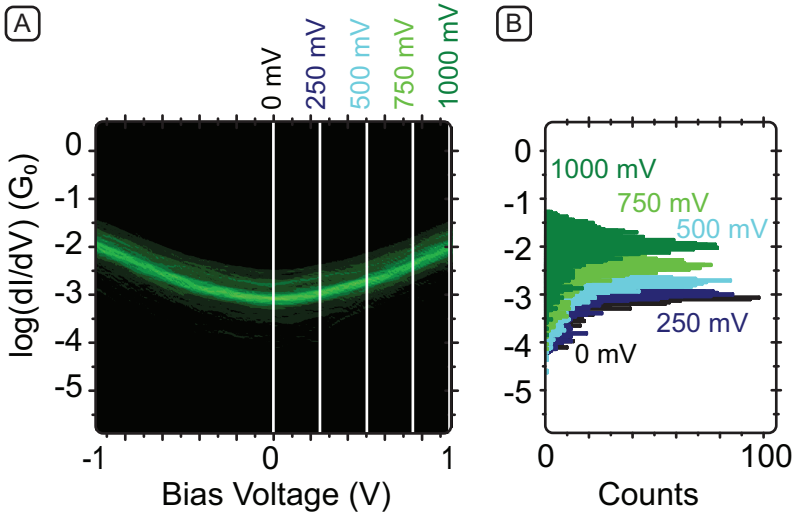

FIGURE 5.3: **2D histogram and its corresponding 1D histograms. A** 2D histogram for the OPE4DT molecule, the vertical lines denote the corresponding 1D histograms shown in **B** for 0, 250, 500, 750 and 1000 mV.

statistical principles which can alter the understanding of the experimental results [10]. Averaging data is a processing tool that is widely used [11–13] and presents the risk of over or under -expressing some values depending on the type of averaging e.g. linear or logarithmic averaging. In addition, averaging smears out information present in the data and removes the relevant intrinsic variations present in the data. Representing our data in the form of 2D histograms avoids the problems mentioned above. The data for OPE2MT were not reproducible as the conductance values varied too much and the tip crashed into the substrate regularly probably due to large defects in the SAMs.

5.3 CHARGE TRANSPORT MEASUREMENTS

In figure 5.4 A-C we show the 2D histograms for the dI/dV of OPE2DT, OPE3DT and OPE4DT. First let us discuss their similar shape. Indeed, the graphs show a symmetric valley-like shape for the whole range of bias voltage. Here we can clearly see the advantage of these histograms, the shape is easily distinguishable, independently of the conductance variations intrinsic to molecular charge transport. The observed symmetric parabola-like shape is expected for symmetric molecular junctions. As we have seen in chapter 1 we can relate

the transmission function T(E) of a junction to the current flowing through it when biased with a voltage eV using the Landauer formalism (equation 5.1).

$$I = \frac{2e}{h}\int_{-\infty}^{\infty} T(E,V)(f_R(E) - f_L(E))dE \tag{5.1}$$

With $f_{R,L}$ being the Fermi-Dirac function for the right and left electrodes with electrochemical potential $E_f - (1-\eta)eV$ and $E_f - \eta eV$ respectively and η being the parameter describing the symmetry of the voltage drop over the junction. For $T = 0$ K we can derive the expression for the first derivative of the current, dI/dV (equation 5.2).

$$\frac{dI}{dV} = \eta T(\eta eV) + (1-\eta)T((1-\eta)eV) \tag{5.2}$$

As an important consequence, symmetric dI/dV-curves are necessarily obtained for symmetrically coupled molecules, irrespective of the (a)symmetry of T(E) around the Fermi level E_F. This is easily seen by inserting $\eta = 0.5$ into the formula above, and interchanging $+V$ and $-V$. Consequently for any transmission function, $T(E)$, the resulting dI/dV curve is symmetric around zero bias and is an average of the $T(E)$ for positive and negative bias voltages. The transmission function for OPE's is, as can be seen in figure 5.5, a valley between the two peaks corresponding to the HOMO and the LUMO. Although it is not symmetric around the Fermi level, the resulting dI/dV does become symmetric for symmetric junctions by virtue of equation 5.2, similar to the measured curves in figure 5.4. In the case of monothiols, like OPE3MT, the junction is asymmetric resulting in an asymmetric voltage drop over the junction and thus in a parameter $\eta \neq 0.5$. It is clear from equation 5.2 that the resulting dI/dV will be asymmetric. Indeed in figure 5.4-D we observe an asymmetric dI/dV for OPE3MT.

5.3.1 Length dependence of the conductance

Let us now concentrate on the trends in the measured conductances for OPE2DT, OPE3DT and OPE4DT. In figure 5.3 we have shown how the 2D histograms are constructed. Of course we can also make a cross-section at each bias to extract a 1D conductance histogram. We therefore can extract the most probable conductance value for each molecule at each bias. The obtained 1D histogram also displays the associated variation in conductance as it is better suited than error bars to visualize the spread in measured values. In figure 5.7-A, the zero bias conductance values (black dots) are plotted as a function of molecular length on a semi-log scale[2]. Hence we notice a roughly exponential dependence of

[2]To determined the lengths the Hyperchem™software release 7.52 is used, the distance from S- to S-atom is calculated.

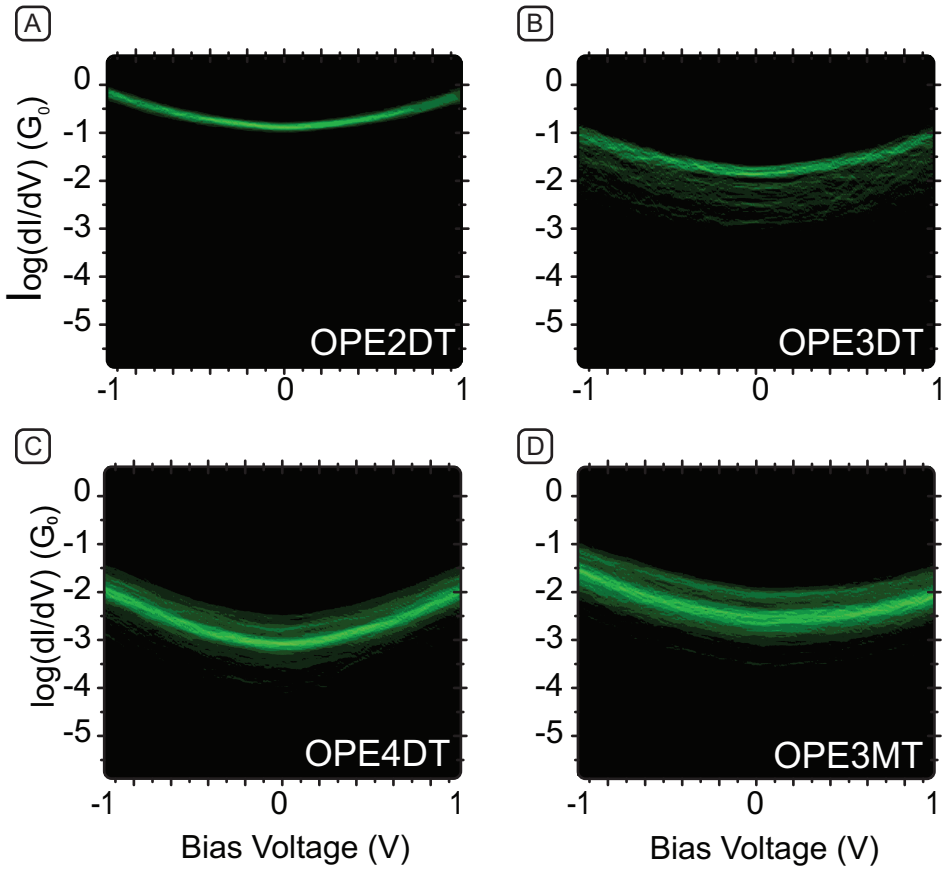

FIGURE 5.4: **Two-dimentional conductance histograms.A-D** show logarithmically binned 2D-histograms of dI/dV (in units of quantum conductance $G_0 = 2e^2/h$) vs. bias voltage V for OPE2DT (**A**), OPE3DT (**B**), OPE4DT (**C**) and OPE3MT (**D**). The colour scale indicates the number of counts and ranges from black (0 counts) to light green (more than 40 counts). The corresponding molecular structures can be found in figure 5.1.

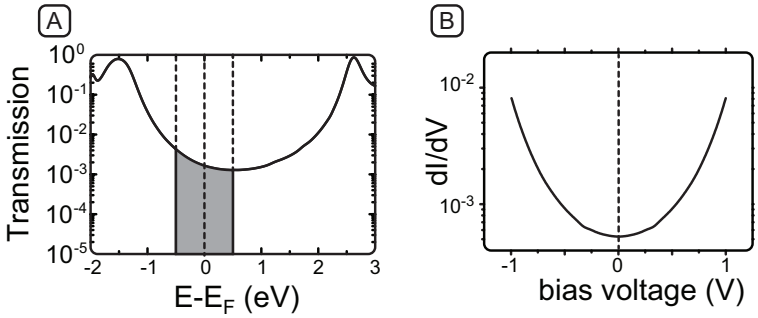

FIGURE 5.5: **Calculated transmission function for OPE3DT. A** Energy dependent transmission function for OPE3DT calculated by Troels Markussen (personal communication) using DFT-NEGF formalism. In gray we indicate the portion of the transmission curve integrated to calculate the current in the junction. **B** We calculate the resulting dI/dV for a symmetric junction with an applied potential V.

the conductance on the molecular length i.e. the conductance is increasing for decreasing lengths. Naively one can make here an analogy with a tunnel barrier and so determine the exponential decay factor β. We will discuss the validity of this analogy later on. Nonetheless, comparing our decay factor of $\beta_{OPE} = 0.35 \pm 0.01$ Å^{-1} with values obtained in the literature (for zero bias conductances) could confirm the validity of our measurement technique. The β values for both amine- and thiol terminated OPE's found in the group of Wang are lower, 0.20 Å^{-1} (STM) [14] and 0.21 Å^{-1} (C-AFM) [15] respectively. In reference [16], a value of 0.32 Å^{-1} is found for a series of shorter molecules (benzene dithiol, OPE2DT and OPE3DT) in a STM break-junction experiment. The group of Wandlowski found a similar value of 0.33 Å^{-1} with the same batch of molecules as ours in a STM break-junction experiment. The same batch of molecules is also used in large area molecular junctions and yields a much lower β value of 0.15 Å^{-1} ascribed to the different coupling to one of the electrodes due to an interface layer (PEDOT:PSS) [6]. So our measurement technique reproduces quite well the values found in literature for β in OPEs. Moreover we can compare our results individually with the reported values in the literature. In figure 5.6 we plot the conductance values found for OPE2DT, OPE3DT and OPE4DT in our measurements and the ones found for the same molecules in the group of Wandlowski (university of Bern). In addition we show the conductance values of OPE3DT found in the literature. We notice here that all the values are consistent with each other and our results. Hence, our experimentally found conductance values and decay constant do confirm the validity of our measurement technique.

A logical next step is to investigate the conductance at finite biases in a similar way. For this we take the cross-section of the 2D histogram at various biases (250, 500, 750 and 1000 mV) in the same fashion as shown in figure 5.3. Already in figure 5.4 we notice that the dI/dV parabolic curves are steeper as the molecules get longer. In figure 5.7-A we plot the conductance values versus the molecular length to study the length dependence with increasing biases in more detail. The conductance values are taken from the 1D histograms extracted from the 2D histograms of figure 5.4, in figure 5.7-B we show the 1D histograms for OPE4DT for various bias voltages. First of all we notice a rough, but not exact, exponential dependence on length for all the biases. Note that for high biases (1V) the dependence on length of the conductance deviates from exponential. Hence, we can also extract a β value for the selected biases which is shown in figure 5.7-C. Surprisingly we find a clear trend in β, for increasing biases the β factor decreases in a non-monotonous way. How can we describe this behaviour of β?

Let us first go back to the analogy between molecular charge transport and

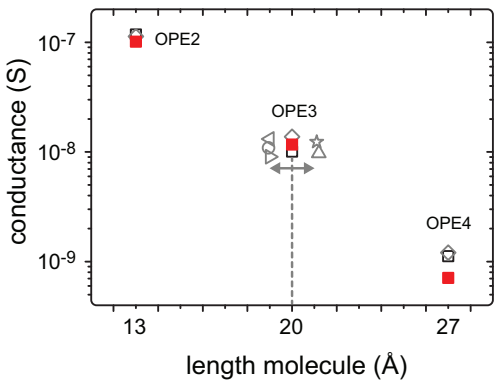

FIGURE 5.6: **Length dependence of the conductance compared to the literature values.** The filled squares are the zero bias conductances for our measurements. The open black squares are the values found by Wandlowski in liquid cell MCBJ. The gray open diamonds are from the same group but measured in a STM. For clarity we plotted the other literature values for OPE3DT with an artificial offset in the x direction (see arrows). (★) is from ref [17], (△) is from ref [18], (◁) is from ref [19], (▷) is from ref [20], (○) is from ref [16].

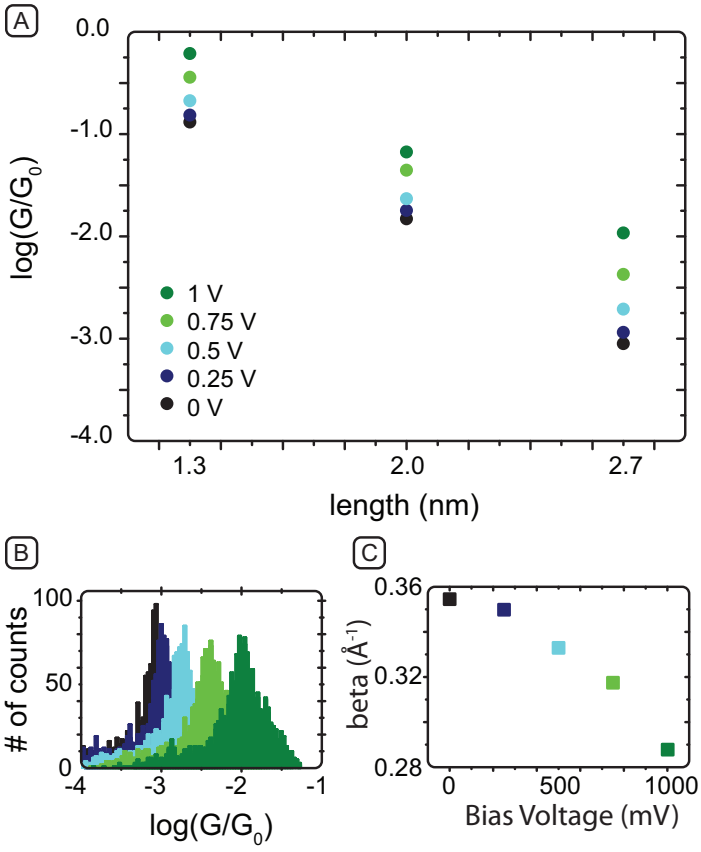

FIGURE 5.7: **Conductances for different bias voltages. A** Length dependence of the conduction for OPE2DT, OPE3DT and OPE4DT at different bias voltages. The conductance values are determined from the cross sections of the 2D histograms from figure 5.4 here shown for OPE4DT in **B C** Attenuation factor β for different bias voltages.

tunnel barriers in order to understand the obtained experimental results. The analogy made between molecular junctions and tunnel junctions rely on the experimental fact that the conductance is exponentially decreasing with increasing molecular length [1, 2, 21, 22]. We can describe a tunnel junction in a straight forward manner, shown in figure 5.8A and in equation 5.3. The resulting conductance G of a tunnel junction of width d, and height φ, the work function of the electrodes, can be expressed as follow:

$$G \propto \frac{2e^2}{h} \exp(-2\kappa d) \text{ where } \kappa = \sqrt{2m\varphi/\hbar} \tag{5.3}$$

Hence we see that the tunneling current is exponentially dependent on the distance and the square root of the work function of the electrodes. In a tunnel junction formed by STM or MCBJ one can continuously change the distance and measure the exponential current decay corresponding to this change [23]. Therefore measuring the current decay is a popular tool for the calibration of the distance in tunnel junctions e.g. STM or mechanically controlled break junctions (MCBJ) [24]. As we have seen in chapter 4, this is valid for low biases and not too small distances. Let us now have a critical look at the use and

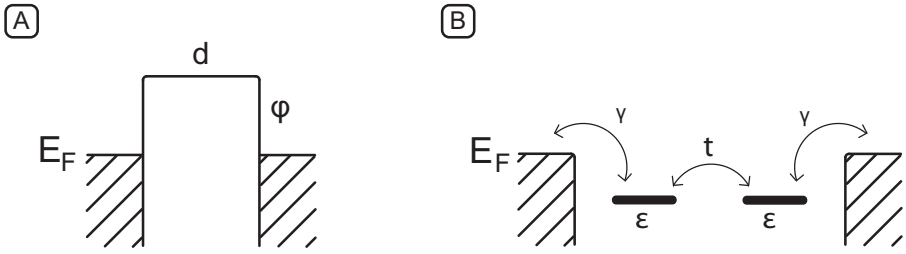

FIGURE 5.8: **Models for charge transport measurements. A** shows a rectangular tunnel barrier with heigth φ and length d. **B** shows a two site tight binding model with a hopping integral t between two site of energy ϵ and γ, the coupling to the leads. The leads are filled up to the Fermi energy E_F as indicated by the hatched lines.

meaning of the decay constant β for molecular charge transport. First we focus on the variation of the length. In contrast to tunnel junctions a molecular junction can not vary the inter-electrode distance continuously. Indeed the length of the different molecules used is changed by varying the number of sub-units e.g. pheny-ethynylene moieties in our case, so the inter-electrode distance is varying in discrete steps. Moreover in a tunnel junction, φ is defined by the work function of the electrodes and remains constant along the experiment. For a molecular junction this is less trivial. Indeed the height of the barrier is usually defined as the distance between the Fermi level and the closest molecular

orbital (HOMO or LUMO). As we will see later on, the position of the HOMO (or LUMO) is dependent on the molecular length, d for conjugated molecules. So in the tunnel barrier model, φ is dependent on d. The later makes it difficult to pin point a physical meaning to the experimentally measured exponential decay β as the barrier is changed for each measured molecule both in length and height. Moreover relating the measured β to a value for φ often results in unrealistic values or large discrepancies between experiment and fit [13, 25]. We should note here that the decay parameter β is poorly defined. However, our experimental findings can be understood in terms of molecular orbitals and resonant tunneling. Indeed a simple tight binding model (TB), introduced in chapter 1 and schematically depicted in figure 5.8-B, may provide a way to physically understand the length dependence of conductance in series of molecular junctions i.e. provide a more solid basis for the definition of β. Calculations of this type relate the rough chemical structure (number of repeating units) of a molecule to an energy dependent transmission function, T(E). Although more refined calculations take all the chemical structure factors into account[26–30], this simple model incorporates the basic physical concepts involved in molecular charge transport. The position of the HOMO (or LUMO) relative to the Fermi energy (E_F) is dependent on the number of hopping sites N and on the overlap integral t like described in equation 5.4 [26, 31].

$$E_{HOMO} = \varepsilon_0 - 2tcos(\frac{\pi}{N+1}) \tag{5.4}$$

Indeed by increasing the number N of sites i.e. the molecular length, we notice that the energy level closest to E_F moves towards E_F. In addition to that the coupling to the leads induces a broadening of the levels roughly exponentially decaying with length. This can easily be understood with simple arguments. The length dependence of the level broadening, $\Gamma(N)$ can be explained by the fact that the influence of the leads decays with increasing length, resulting in a smaller energy broadening. In addition, this broadening can be understood intuitively in terms of the uncertainty principle as the molecule gets longer, the residence time on it gets longer as well, resulting in a decrease of the broadening Γ [30].

Consequently we use this simple TB model to calculate a transmission function T(E) for toy molecules with increasing length i.e. the number of hopping sites. We can now investigate the implication of this more realistic model on the definition of β. In figure 5.9-A we present the calculated T(E) for molecules with a number of sites ranging from 1 to 5 sites. In this calculation the position of the Fermi level, E_F is arbitrary, in figure 5.9-A we show the Fermi level at three different positions. Note that the zero bias conductance is proportional to

the transmission function at the Fermi level. In figure 5.9-C we show the transmission values at the three positions of E_F (indicated in figure 5.9 by dashed lines) for the five toy molecules. First, we notice that when E_F is far away from the molecular levels (gray dashed line in figure 5.9-A) the transmission at the Fermi energy i.e. the zero bias conductance is exponentially dependent on the molecular length. Nevertheless for a Fermi energy closer to the levels we observe a deviation from the exponential behaviour. Moreover if the Fermi energy is found at or close to an energy where the transmission function cross, no or little length dependence will be observed[32].So the observation of an exponential length dependence of the conductance and the related β factor is strongly dependent on the position of the Fermi energy relative to the LUMO or HOMO.

In our experiment (figure 5.7 A and C) we observe a decrease in length dependence (β) for increasing bias voltage. So at higher voltages we integrate over a wider range, closer to the frontier molecular level, resulting in a shallower length dependence. Hence the toy model we use does reproduce qualitatively the trend observed in the experiments. In addition to that we have noticed in figure 5.9-D that for biases far from resonance the length dependence is exponential, while for bias windows reaching closer to the LUMO the length dependence deviates from exponential. This trend is of course more subtle to detect in our experiments due to the limited number of molecules (three different lengths) and the inherent spread of the conductance value as shown in the histograms. Still in figure 5.7-A we notice a slight deviation from exponential behaviour although more molecules are needed to make this point more solid. The range of biases we can apply, typically 1V, is not large enough to get closer to resonance and observe a clear deviation from exponential in the length dependence of conductance. Moreover the exponential length dependence of the conductance is observed when the Fermi level is far enough from the HOMO or LUMO. Oppositely, for a Fermi level closer to the HOMO or LUMO, the length dependence can be reduced or even disappear. More importantly this shows that the length dependence of the molecular conductance does not need to be exponential.

5.3.2 Looking at our measurements in the light of TVS

We discussed the limitations of transition voltage spectroscopy in chapter 4. To do so we first critically looked at TVS in the light of charge transport theory. This was followed by a comparison of measurements on vacuum tunnel barrier junctions and molecular junctions. Part of the results for the molecular junctions was taken from literature [33, 34] while the other part is taken from the

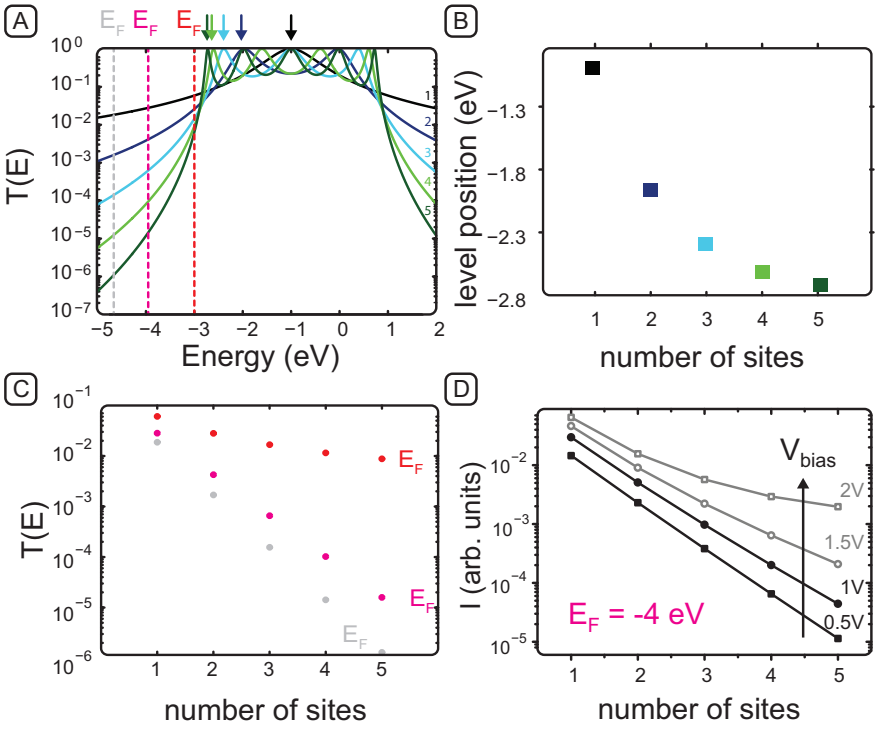

FIGURE 5.9: **Calculated T(E) at various energies for an increasing number of sites.** Calculations obtained with the simple toy model introduced in the main text. **A** Calculated energy dependent transmission functions for different molecular lengths. The parameters are: $t = 1$, $\varepsilon = -1$ and $\gamma_1 = \gamma_2 = 0.5$. **B** We show the position of the energy level closest to the Fermi energy as a function of the number of sites, the colours of the dots correspond to the colours of the transmission curves and the arrows indicating the levels in **A**. With the dashed lines we indicate three positions of the Fermi level. **C** Values of the transmission at the various Fermi energies as a function of the number of sites. The colours of the dots correspond to the colours of the dashed lines in **A**. **D** Calculated currents for different molecular length at increasing voltages.

measurements presented in this chapter on the OPEDT series. We describe here shortly the protocol used for the TVS results and the obtained results.

The basic idea of TVS is to plot the current-voltage characteristics on a Fowler-Nordheim plot i.e. $ln(I/V^2)$ vs $1/V$ which yields a minimum, V_m (see chapter 4). In figure 5.10-A we show one I(V) curve for OPE3DT and in figure 5.10-B the corresponding Fowler-Nordheim plot for positive bias voltages, we then clearly observe V_m.

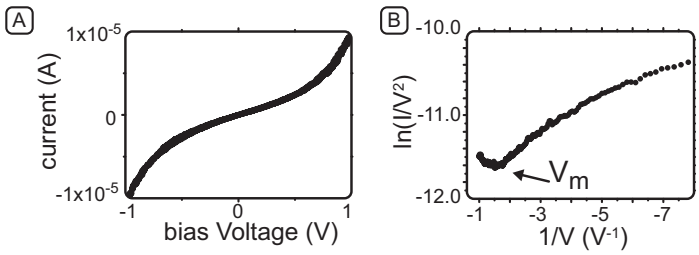

FIGURE 5.10: **How to make a Fowler-Nordheim plot. A** I(V) curve for OPE3DT. **B** corresponding Fowler-Nordheim plot for positive bias voltages.

For all the measurements presented above on OPE2DT, OPE3DT, OPE4DT and OPE3MT we computed the position of the minimum in the Fowler-Nordheim plot for both the negative bias, V_m^- and the positive bias, V_m^+. To represent the data in a statistical meaningful way, we choose to bin the V_m values and construct histograms for each molecule and bias polarity. In figure 5.11 we show the histograms for the four above mentioned molecules and show V_m^- and V_m^+ in two separate histograms.

The expectation of TVS is to relate the position of the closest level to the Fermi energy (HOMO or LUMO) with the position of V_m. Moreover we know from extended calculations[35] and optical measurements [35] that the HOMO is closer to E_F for longer molecules. So we expect to find a dependence of V_m with molecular length. However the nature of this relation is still unclear, as it has been showed by Mirjani et al. [31] and in chapter 4. More, experimentally challenging, ingredients are needed to extract information on the exact position of the molecular levels. Indeed we have seen in chapter 4 that knowledge on the junction's potential profile is essential for determining the position of molecular levels from V_m [31, 36]. In figure 5.11-A-C we do not observe the expected dependence of V_m on the length of the dithiolated molecules. Indeed for increasing molecular length it is not possible to distinguish any trends in the position of V_m. TVS is also limited by the intrinsic variation found in molecular junctions.

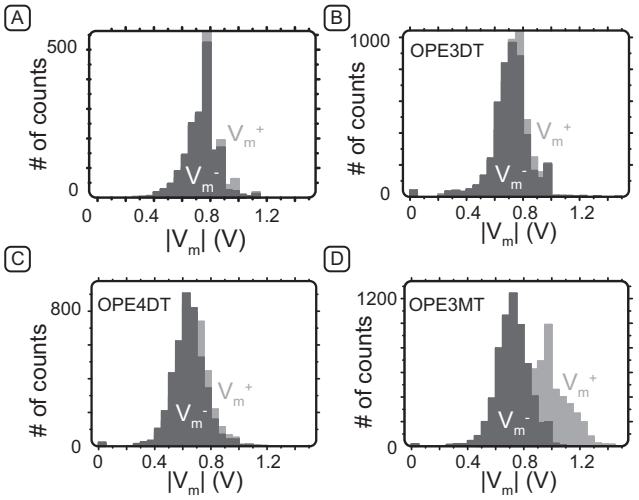

FIGURE 5.11: **Histograms for V_m^- and V_m^+ for OPE2DT A, OPE3DT B, OPE4DT C and OPE3MT D** Here the histograms for V_m^- and V_m^+ are presented. Note that we present here the absolute value of V_m.

5

Second we notice that for OPE2DT, OPE3DT and OPE4DT the values for V_m^- and V_m^+ are similar within the experimental error i.e. the histogram do fully overlap (figure 5.10-A-C). This is not true for OPE3MT as we can see on figure 5.10-D, indeed V_m^+ (0.92 V) is found at higher values than V_m^- (0.72 V). Let us discuss here the differences found between OPE3DT and OPE3MT. The dithiolated molecules (OPE2DT, OPE3DT and OPE4DT) have a sulfur atom at each extremities so that they can bind to both gold electrodes. In contrast monothiolated molecules, like OPE3MT, only posses one sulfur binding group to bind to the electrodes (in this case to the gold substrate when the SAM is formed). The junction symmetry determines the coupling, Γ, to the leads. The coupling Γ describes the extend to which the wave functions do overlap in a molecular junction. So for OPE3MT the overlap at one electrode is smaller than at the other one, reducing the total broadening (see chapter 1). Hence the conductances of the monothiolated species are lower than their dithiolated homologue (see figure 5.4). The symmetry in the binding groups do also influence the symmetry of the junction's potential profile, η (see chapter 1). So when $\eta = \frac{1}{2}$ the voltage drop is symmetric, while for $\eta = 0$ the voltage drop is completely asymmetric. Mirjani *et al.* demonstrated that we can relate η to V_m [31] as follow: $\frac{\eta}{1-\eta} = \frac{V_m^-}{V_m^+}$.

Hence, by comparing the histogram peaks found for V_m^+ and V_m^- in figure 5.11 for OPE2DT, OPE3DT, OPE4DT and OPE3MT we can calculate the parameter η for the four molecules: $\eta_{OPE2DT} = 0.49$, $\eta_{OPE3DT} = 0.5$, $\eta_{OPE4DT} = 0.5$ and $\eta_{OPE3MT} \approx 0.41$. The dithiolated molecules all have a $\eta \approx 1/2$ which is indeed expected for a symmetric junction. For OPE3MT, the junction is not completely asymmetric ($\eta = 0$) as still the molecule has some coupling to the electrodes at the side without thiol, resulting in a $\eta \neq 0$. Markussen *et al.* calculated for a similar junction a value for $\eta = 0.4$ which is quite in agreement with our experimentally found value for OPE3MT[37].

As a final remark, from the TVS on our measurements we can not determine the position of the molecular levels. nevertheless TVS can be useful for quantifying the (a)symmetry of molecular junctions.

5.4 Conclusions

To summarize, we present in this chapter C-AFM conductance measurements on a series of OPE molecules of various length. We introduced a new plotting method to present all the voltage dependent conductance data for each molecule at once in the form of a 2D histogram. Clearly, the measured zero-bias conductance values for OPE2DT, OPE3DT and OPE4DT are consistent with the literature, validating our C-AFM technique. Moreover we investigated the voltage dependence of the conductance and noticed a decrease in the "β" value for increasing biases. This voltage dependence of the conductance is consistent with simple calculations. Nonetheless we note that the length dependence of molecular conductance is not always exponential. Furthermore we probed the (a)symmetry of the molecular junctions (OPE3DT and OPE3MT) using TVS.

References

[1] B. Mann and H. Kuhn, *Tunneling through Fatty Acid Salt Monolayers*, Journal Of Applied Physics **42**, 4398 (1971).

[2] H. B. Akkerman and B. de Boer, *Electrical conduction through single molecules and self-assembled monolayers*, Journal Of Physics-Condensed Matter **20** (2008).

[3] H. B. Akkerman, P. W. M. Blom, D. M. de Leeuw, and B. de Boer, *Towards molecular electronics with large-area molecular junctions*, Nature **441**, 69 (2006).

[4] A. Salomon, D. Cahen, S. Lindsay, J. Tomfohr, V. B. Engelkes, and

C. D. Frisbie, *Comparison of electronic transport measurements on organic molecules*, Advanced Materials **15**, 1881 (2003).

[5] E. H. van Dijk, D. J. T. Myles, M. H. van der Veen, and J. C. Hummelen, *Synthesis and Properties of an Anthraquinone-Based Redox Switch for Molecular Electronics*, Organic Letters **8**, 2333 (2006).

[6] H. Valkenier, E. H. Huisman, P. A. van Hal, D. M. de Leeuw, R. C. Chiechi, and J. C. Hummelen, *Formation of High-Quality Self-Assembled Monolayers of Conjugated Dithiols on Gold: Base Matters*, Journal of the American Chemical Society **133**, 4930 (2011).

[7] X. Y. Xiao, B. Q. Xu, and N. J. Tao, *Measurement of single molecule conductance: Benzenedithiol and benzenedimethanethiol*, Nano Letters **4**, 267 (2004).

[8] X. Li, J. He, J. Hihath, B. Xu, S. M. Lindsay, and N. Tao, *Conductance of Single Alkanedithiols: Conduction Mechanism and Effect of Molecule-Electrode Contacts*, Journal of the American Chemical Society **128**, 2135 (2006).

[9] W. Haiss, R. J. Nichols, H. van Zalinge, S. J. Higgins, D. Bethell, and D. J. Schiffrin, *Measurement of single molecule conductivity using the spontaneous formation of molecular wires*, Physical Chemistry Chemical Physics **6**, 4330 (2004).

[10] M. T. Gonzalez, S. M. Wu, R. Huber, S. J. van der Molen, C. Schonenberger, and M. Calame, *Electrical conductance of molecular junctions by a robust statistical analysis*, Nano Letters **6**, 2238 (2006).

[11] V. B. Engelkes, J. M. Beebe, and C. D. Frisbie, *Analysis of the causes of variance in resistance measurements on metal-molecule-metal junctions formed by conducting-probe atomic force microscopy*, Journal Of Physical Chemistry B **109**, 16801 (2005).

[12] D. Fracasso, H. Valkenier, J. C. Hummelen, G. C. Solomon, and R. C. Chiechi, *Evidence for Quantum Interference in SAMs of Arylethynylene Thiolates in Tunneling Junctions with Eutectic GaIn (EGaIn) Top-Contacts*, Journal of the American Chemical Society **133**, 9556 (2011).

[13] H. B. Akkerman, R. C. G. Naber, B. Jongbloed, P. A. van Hal, P. W. M. Blom, D. M. de Leeuw, and B. de Boer, *Electron tunneling through alkanedithiol self-assembled monolayers in large-area molecular junctions*, Proceedings

Of The National Academy Of Sciences Of The United States Of America **104**, 11161 (2007).

[14] Q. Lu, K. Liu, H. Zhang, Z. Du, X. Wang, and F. Wang, *From Tunneling to Hopping: A Comprehensive Investigation of Charge Transport Mechanism in Molecular Junctions Based on Oligo(p-phenylene ethynylene)s*, ACS Nano **3**, 3861 (2009).

[15] K. Liu, G. R. Li, X. H. Wang, and F. S. Wang, *Length dependence of electron conduction for oligo(1,4-phenylene ethynylene)s: A conductive probe-atomic force microscopy investigation*, Journal of Physical Chemistry C **112**, 4342 (2008).

[16] Y. Xing, T.-H. Park, R. Venkatramani, S. Keinan, D. N. Beratan, M. J. Therien, and E. Borguet, *Optimizing Single-Molecule Conductivity of Conjugated Organic Oligomers with Carbodithioate Linkers*, Journal of the American Chemical Society **132**, 7946 (2010).

[17] J. Liao, M. A. Mangold, S. Grunder, M. Mayor, C. Schönenberger, and M. Calame, *Interlinking Au nanoparticles in 2D arrays via conjugated dithiolated molecules*, New Journal of Physics **10**, 065019 (2008).

[18] S. M. Wu, M. T. Gonzalez, R. Huber, S. Grunder, M. Mayor, C. Schonenberger, and M. Calame, *Molecular junctions based on aromatic coupling*, Nature Nanotechnology **3**, 569 (2008).

[19] X. Y. Xiao, L. A. Nagahara, A. M. Rawlett, and N. J. Tao, *Electrochemical gate-controlled conductance of single oligo(phenylene ethynylene)s*, Journal Of The American Chemical Society **127**, 9235 (2005).

[20] R. Huber, M. T. González, S. Wu, M. Langer, S. Grunder, V. Horhoiu, M. Mayor, M. R. Bryce, C. Wang, R. Jitchati, et al., *Electrical Conductance of Conjugated Oligomers at the Single Molecule Level*, Journal of the American Chemical Society **130**, 1080 (2008).

[21] C. D. Bain and G. M. Whitesides, *Attenuation Lengths of Photoelectrons in Hydrocarbon Films*, Journal of Physical Chemistry **93**, 1670 (1989).

[22] W. Wang, T. Lee, and M. A. Reed, *Mechanism of electron conduction in self-assembled alkanethiol monolayer devices*, Physical Review B **68**, 035416 (2003).

[23] G. Binnig, H. Rohrer, C. Gerber, and E. Weibel, *Surface Studies by Scanning Tunneling Microscopy*, Physical Review Letters **49**, 57 (1982).

[24] M. L. Trouwborst, C. A. Martin, R. H. M. Smit, C. M. Guedon, T. A. Baart, S. J. van der Molen, and J. M. van Ruitenbeek, *Transition Voltage Spectroscopy and the Nature of Vacuum Tunneling*, Nano Letters **11**, 614 (2011).

[25] W. Haiss, S. Martin, L. E. Scullion, L. Bouffier, S. J. Higgins, and R. J. Nichols, *Anomalous length and voltage dependence of single molecule conductance*, Physical Chemistry Chemical Physics **11**, 10831 (2009).

[26] F. Mirjani and J. M. Thijssen, *Density functional theory based many-body analysis of electron transport through molecules*, Physical Review B **83**, 035415 (2011).

[27] T. Markussen, R. Stadler, and K. S. Thygesen, *The Relation between Structure and Quantum Interference in Single Molecule Junctions*, Nano Letters **10**, 4260 (2010).

[28] M. P. Samanta, W. Tian, S. Datta, J. I. Henderson, and C. P. Kubiak, *Electronic conduction through organic molecules*, Physical Review B **53**, R7626 (1996).

[29] C. Joachim and M. A. Ratner, *Molecular electronics: Some views on transport junctions and beyond*, Proceedings Of The National Academy Of Sciences Of The United States Of America **102**, 8801 (2005).

[30] S. Datta, *Electrical resistance: an atomistic view*, nanotechnology **15**, S433 (2004).

[31] F. Mirjani, J. M. Thijssen, and S. J. van der Molen, *Advantages and limitations of transition voltage spectroscopy: A theoretical analysis*, Physical Review B **84**, 115402 (2011).

[32] G. Sedghi, V. M. Garcia-Suarez, L. J. Esdaile, H. L. Anderson, C. J. Lambert, S. Martin, D. Bethell, S. J. Higgins, M. Elliott, N. Bennett, et al., *Long-range electron tunnelling in oligo-porphyrin molecular wires*, Nature Nanotechnology **6**, 517 (2011).

[33] J. M. Beebe, B. Kim, C. D. Frisbie, and J. G. Kushmerick, *Measuring relative barrier heights in molecular electronic junctions with transition voltage spectroscopy*, Acs Nano **2**, 827 (2008).

[34] J. M. Beebe, B. Kim, J. W. Gadzuk, C. D. Frisbie, and J. G. Kushmerick, *Transition from direct tunneling to field emission in metal-molecule-metal junctions*, Physical Review Letters **97** (2006).

[35] H. Valkenier, Ph.D. thesis, Groningen University (2011).

[36] J. Z. Chen, T. Markussen, and K. S. Thygesen, *Quantifying transition voltage spectroscopy of molecular junctions: Ab initio calculations*, Physical Review B **82**, 121412 (2010).

[37] T. Markussen, J. Chen, and K. S. Thygesen, *Improving transition voltage spectroscopy of molecular junctions*, Physical Review B **83**, 155407 (2011).

6

Evidence for quantum interference in molecular charge transport

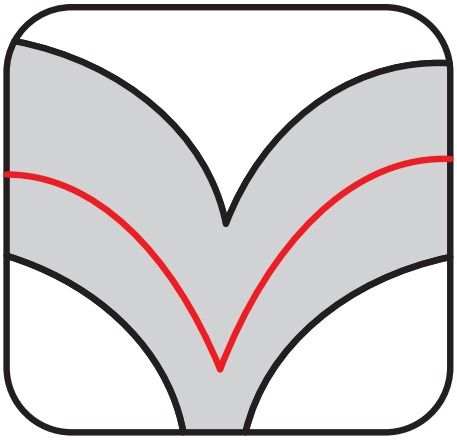

The results presented in this chapter have been published as:

C. M. Guédon, H. Valkenier, T. Markussen, K. S. Thygesen, J. C. Hummelen and S. J. van der Molen, *Observation of quantum interference in molecular charge transport*, **Nature Nanotechnology**, **7**, 305 (2012)

6.1 INTRODUCTION

As the dimensions of a conductor approach the nano-scale, quantum effects will begin to dominate its behavior. This entails the exciting possibility of controlling the conductance of a device by direct manipulation of the electron wave function. Such control has been most clearly demonstrated in mesoscopic semiconductor structures at low temperatures. Indeed, the Aharanov-Bohm effect[1], conductance quantization [2, 3] and universal conductance fluctuations [4] are direct manifestations of the electron wave nature. However, an extension of this concept to more practical temperatures has not been achieved so far. As molecules are nano-scale objects with typical energy level spacings (~ eV) much larger than the thermal energy at 300 K (≈ 25 meV), they are natural candidates to enable such a break-through [5–11]. Fascinating phenomena including giant magnetoresistance, Kondo effects and conductance switching, have previously been demonstrated at the molecular level[12–18]. Here, we report direct evidence for destructive quantum interference in charge transport through two-terminal molecular junctions at room temperature. Furthermore, we show that the degree of interference can be controlled by simple chemical modifications of the molecule. Not only does this provide the experimental demonstration of a new phenomenon in quantum charge transport, it also opens the road for a new type of molecular devices based on chemical or electrostatic control of quantum interference.

The wave nature of electrons is fundamental to our understanding of almost all of chemistry. In fact, the very existence of molecular orbitals is a direct result of spatial confinement of electron waves. This in turn leads to pronounced reactivity variation at different sites of molecules. The electron wave character also plays a key role in mesoscopic physics, which studies quantum phenomena in charge transport. For example, the conductance properties of mesoscopic ring structures at low temperatures are dominated by quantum interference. If the partial waves through both branches of the ring add up destructively (constructively) a suppression (enhancement) of the conductance is observed. For certain classes of molecular junctions, a similar effect is expected [6–11]. However, in that case the picture of interference resulting from distinct spatial paths is no longer valid. Instead, interference in a molecule must be described in terms of electron propagation via paths of orbitals, differing not only in space, but also in energy. Since the properties of molecular orbitals can be manipulated by chemical design, quantum interference promises control over the conductance of molecular devices at the wave function level. In fact, conductance tuning over orders of magnitude at ambient temperatures comes within reach. Although

variations in charge transfer rates within donor-bridge-acceptor molecules can be explained in terms of interference [19, 20], only indirect indications for interference have been found in molecular conductance experiments [21, 22]. Here, we provide unambiguous evidence for destructive quantum interference in two-terminal molecular junctions.

6.2 EXPERIMENTAL DETAILS

To investigate the influence of quantum interference on molecular conductance properties, five rigid π-conjugated molecular wires are synthesized [1] (see capter 2). The first two molecules (AQ-MT and AQ-DT, left in figure 6.1 A) contain an anthraquinone-unit. This makes them cross-conjugated , note that linear conjugation refers to a sequence of alternating single and double bonds between both ends of an organic molecule [23, 24]. Cross-conjugation, however, implies that the sequence of alternating single and double bonds between both ends of the molecule is broken, although all C-atoms have formed double or triple bonds, i.e. all C-atoms are sp^2 or sp hybridized. The AQ-MT molecule is terminated by a protected thiol group at one side only (monothiolated: MT), whereas AQ-DT is dithiolated (DT). The third molecular wire (AC-DT) contains a central anthracene-unit and is linearly conjugated. Otherwise it is very similar to AQ-DT, e.g. both have a length of 24.5 Å. Finally, two linearly conjugated reference compounds, oligo(phenylene-ethynylene)-monothiol and -dithiol (OPE3-MT and OPE3-DT), are studied (see chapter 5). We stress that apart from the thiols, all five molecules have the same phenylene-ethynylene endgroups.

To measure transport, we first create self-assembled monolayers (SAMs) of each molecule on thin Au layers (200 nm, Si-substrates). To obtain high-quality, densely packed SAMs, we use a procedure established recently (Chapter 5) [25]. Next, a conducting atomic force microscopy (AFM) probe is brought in close contact to a SAM. In this way, we can perform charge transport experiments through the molecular layer, using the Au-covered substrate and the AFM-tip as electrodes (figure 6.1B). We typically connect to a few hundred molecules, while measuring current, I, versus bias voltage V [26]. However, the exact number does vary. For this reason, we present our results in two-dimensional (2D) histograms. Figure 6.1 C shows such a 2D-histogram for AC-DT. To construct this plot, we have logarithmically binned the dI/dV-values (determined numerically) for each bias applied (see chapter 5). This effectively results in a

[1] The molecules and the SAM are made by Hennie Valkenier and Kees Hummelen at the University of Groningen

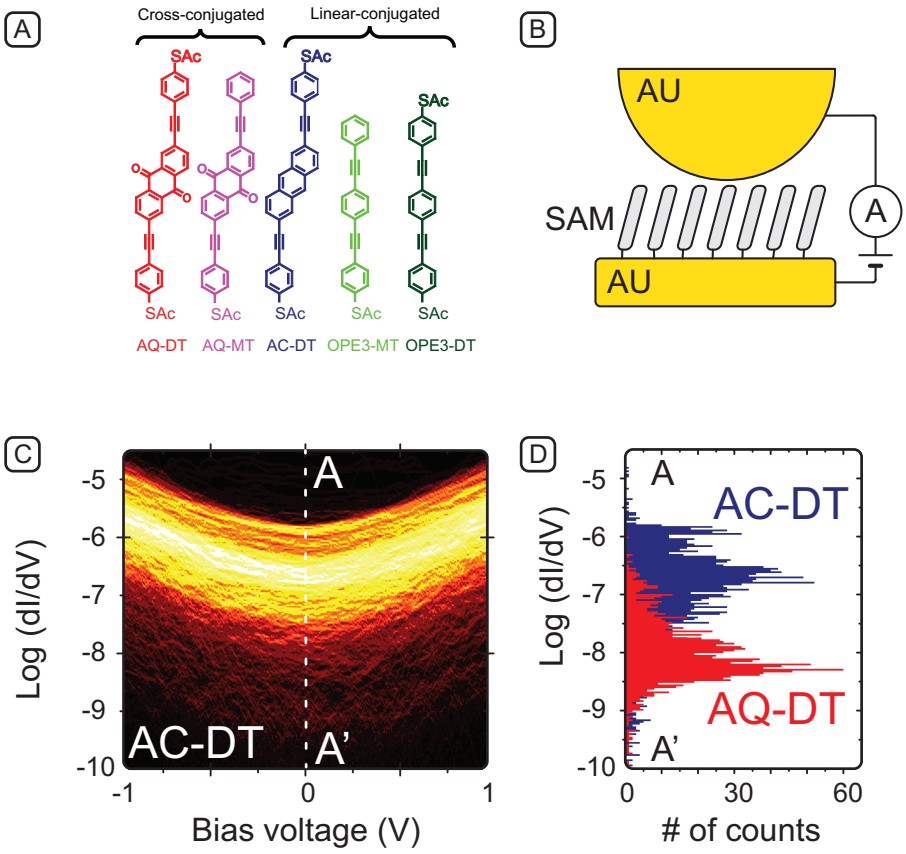

FIGURE 6.1: **Conductance measurements on molecular wires**. **A**, chemical structure of the molecules used. AQ-DT and AQ-MT are both cross-conjugated, whereas AC-DT, OPE3-DT and OPE3-MT are linearly conjugated. AQ-DT, AC-DT and OPE3-DT are dithiolated and thus symmetric; AQ-MT and OPE3-MT are monothiolated. The colour code is also used in the following figures. **B**, schematic view of the junction formed by the molecules self-assembled on a conducting substrate (Au) and the conducting AFM tip (Au), **C**, logarithmically binned 2D-histogram for the dI/dV-values vs. bias voltage V for AC-DT in Ω^{-1}, the colour scale indicates the number of counts (black: no counts; white: more than 40 counts) **D**, cross-section of the 2D-histogram shown in **C** along the line AA' (zero-bias conductance) resulting in a 1D-histogram (blue). Shown in red is the 1D-histogram for AQ-MT taken from Fig. 3a.

sequence of 1D-histograms, plotted for each V. To illustrate this, figure 6.1 D shows a cross-section of figure 6.1 C at $V = 0$ V (blue histogram; see dashed line in figure 6.1 C). This is the zero-bias 1D-histogram for AC-DT [27]. Representing our data in 2D-histograms has two major advantages. First, it allows us to show a full data set in one plot, without a need for either determining an average curve or for data selection [27]. For completeness: I(V)-curves that were either flat (no contact) or that showed direct contact are excluded from figure 6.1 and 6.3. However, such curves represent a small minority of our data ($\approx 5\%$). Second, it enables us to distinguish general tendencies in dI/dV-curves from statistical variations in the conductance values themselves. The latter are inherent to molecular transport studies [26, 27]. Figure 6.1-C clearly illustrates this advantage: a symmetric valley-like shape is seen for the full data range. This shape is virtually independent of the conductance values, which do scatter indeed (figure 6.1-D).

6.3 Indirect evidence for interferences

Figure 6.1-D compares the zero-bias conductance histograms for both AQ-DT (red) and AC-DT (blue). Interestingly, AQ-DT exhibits conductance values that are almost two orders of magnitude lower than those of AC-DT. This is quite remarkable, since the energy difference between the HOMO and LUMO levels is very similar for these molecules (HOMO: highest occupied molecular orbital; LUMO: lowest unoccupied molecular orbital). From UV-Vis measurements, we find an optical HOMO-LUMO gap of 2.88 eV for AQ-DT and 2.90 eV for AC-DT. Our calculations yield fundamental HOMO-LUMO gaps of 4.23 eV and 4.61 eV, respectively [2]. Note that the optical gap and the fundamental gap differ by the electron-hole interaction. Furthermore, figure 6.1-D cannot be trivially explained from a weaker coupling of AQ-DT to the AFM-tip, since the endgroups of both molecules are exactly the same. As we shall elaborate on below, the large difference in conductance is instead indicative of destructive interference in the AQ-DT junctions. In figure 6.2-A we present calculations of the energy-dependent transmission function, $T(E)$, for junctions containing AC-DT, AQ-DT, and AQ-MT. This function describes the quantum mechanical probability that an electron with energy E traverses the molecular junction. Once $T(E)$ is known, the $I(V)$-curves can be calculated using Landauer's formula (Appendix C). In particular, the low bias conductance is given by $dI/dV(V = 0) = 2e^2/h \cdot T(E = E_F)$. For a molecular junction, $T(E)$ typically ex-

[2] The calculations are performed by Troels Markussen and Kristian Thygesen at the Danish Technical University in Copenhagen

hibits peaks around the orbital energies, where electrons can tunnel resonantly. In the energy gaps, $T(E)$ is normally rather featureless, as exemplified by AC-DT in figure 6.2-A. However, for AQ-DT and AQ-MT, $T(E)$ exhibits a strong dip or 'anti-resonance'. This feature is a result of a Fano-like [28, 29] destructive interference [6–11]. To reveal the origin of the anti-resonance, we transform the frontier molecular orbitals into an equivalent set of maximally localized molecular orbitals (LMOs)[9]. The upper part of figure 6.2-D shows the three relevant LMOs obtained for AQ-DT. Two are localized on the left and right parts of AQ-DT, respectively. These LMOs have the same energy and correspond essentially to the sum and difference of the almost degenerate HOMO and HOMO-1 (figure 6.2-A). The LMO localized in the center of AQ-DT is essentially the LUMO and has a higher energy. It is now clear that an electron with an energy, E, lying inside the HOMO-LUMO gap can traverse the molecule via two distinct paths: either directly from the left to the right LMO or by going via the energetically higher LMO (arrows in figure 6.2-D). It can be shown that the upper and lower routes yield a phase difference of π within the HOMO-LUMO gap, i.e., the partial waves interfere destructively (Appendix C). Consequently, $T(E)$ shows a strong minimum at the energy where the partial waves have equal weight. Figure 6.2-C illustrates this, by showing $T(E)$ calculated for the lower and upper routes separately, as well as for the combined three-site model. Note the similarity to figure 6.2-A. For AC-DT, the HOMO is well separated from the HOMO-1. Hence, a transformation to LMOs leads to only two, left and right localized, orbitals (figure 6.2-B). As there is only a single path available, no interference effects occur for AC-DT.

Note that quantum interference is only possible if the processes are phase coherent,so one may wonder if it is possible to observe this phenomenon at room temperature? First of all it is known in organic chemistry that the para- and meta- substitutions are responsible for different reactivities for reactions at room temperature, which is related to interferences. This is also found in room temperature transport measurements with molecules including para or meta connections on a phenyl ring [21, 30]. Moreover calculations predict that decoherence effects induced by electron-phonon interaction due to the finite temperature do not destroy the destructive interference in model cross-conjugated systems at room temperature [31–33]. One intuitive explanation is that we are in the strong coupling regime (see chapter 1) meaning that the electron residence time on the electronic levels is too short to interact with the phonons. Alternatively the distance needed over which the electron should be phase coherent is limited to the central part of the quinone moiety (or the phenyl ring in the para/meta case).

We now compare the calculations with the experiments in figure 6.1-D. In

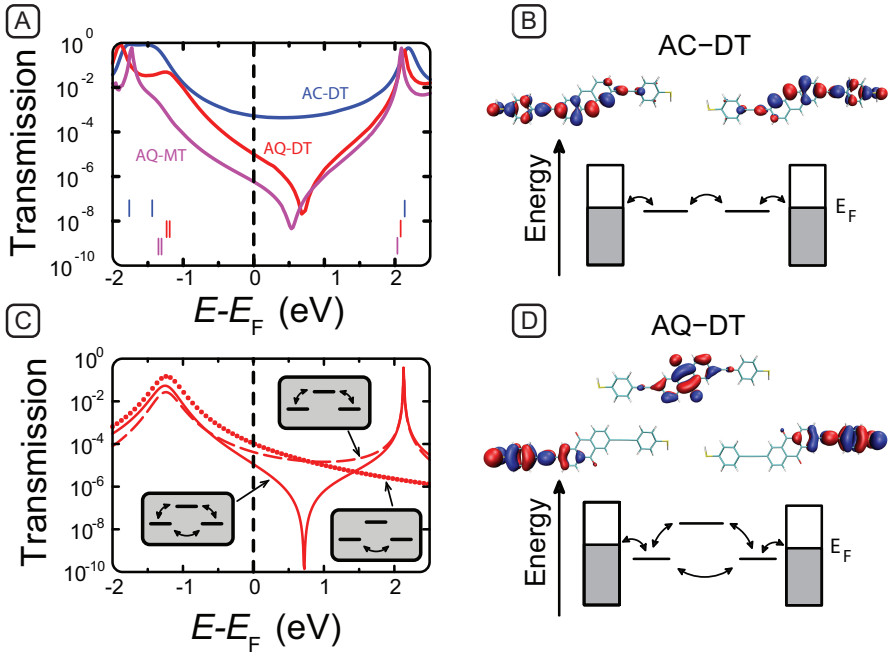

FIGURE 6.2: **Origin of interference in cross-conjugated molecules**. **A**, Transmission functions $T(E)$ for AC-DT (blue), AQ-DT (red) and AQ-MT (purple) calculated with DFT+Σ. The vertical bars mark the energies of the frontier orbitals HOMO-1, HOMO (left side) and LUMO (right side). The lower part of **B** and **D** pictures schematic transport models derived from the localized molecular orbitals presented in the upper parts. In the three-site model shown in **D**, there are evidently two routes through the molecule: a lower route directly from the left to the right site and an upper route via the central orbital. Panel **C** shows $T(E)$ for the lower (dotted line) and upper route (dashed line). A coherent addition of the transmission probability amplitudes from the two paths, with a phase difference of π, yields the three-site transmission function (solid line). This reproduces the essential features of **A**, for AQ-DT and AQ-MT..

figure 6.2-A, the $T(E_F)$-values are around two orders of magnitude lower for AQ-DT than for AC-DT. This is in reasonable agreement with the strongly reduced conductance values for AQ-DT in figure 6.1-D. We thus have a first, indirect evidence for interference in AQ-DT.

6.4 Direct evidence for quantum interference

To investigate this further, we inspect the full 2D-histogram of AQ-DT (figure 6.3-A). For the full voltage range, its dI/dV-values are dramatically lower than those of AC-DT (figure 6.1-C). However, the 2D-histogram has a parabola-like appearance similar to AC-DT, i.e. we observe no anomaly that can be connected to the calculated transmission dip. Hence, although the surprisingly low conductance of AQ-DT is most likely due to quantum interference, the evidence is only indirect. This situation is comparable to the one in Refs. [21, 22]
Let us next consider AQ-MT molecules, which should also exhibit an anti-resonance (figure 6.2-A). Figure 6.3-B shows the 2D-histogram of the dI/dV-curves for AQ-MT. Remarkably, these data do show a clear anomaly at zero bias voltage. In particular, the curvature of the dI/dV-traces in figure 6.3 B is negative for all V (except around $V = 0$). What is equally striking in figure 6.3-B is the large voltage range over which the anomaly extends. Even up to $V = \pm 1$ V, the dI/dV-curves are dominated by the minimum at $V = 0$ V. This points to a characteristic energy scale of ≈ 1 eV, which corresponds well with the width of the interference-induced dip in $T(E)$ in figure 6.2-A. Moreover, this large energy scale rules out Kondo effects and Coulomb blockade as possible explanations for the anomaly. Coulomb blockade can also be ruled out via the experimental data. If Coulomb blockade were the dominant effect behind figure 6.3-B, it should also be present in the other molecular junctions, which have the same length and hence lead to roughly the same capacitance. However, no anomaly is seen in figures 6.1-C and 6.3-A, 6.3-C and 6.3-D. Hence, figure 6.3-B makes a strong case for quantum interference.

To further validate this interpretation, we calculate dI/dV-curves for AQ-MT from $T(E)$ (see Appendix C). A key role in these calculations is played by the position of the anti-resonance in $T(E)$ relative to E_F. This position is difficult to predict theoretically. This is related to the well-known problems of the applied methodology to describe energy level alignments and to the uncertainty of the size of the surface dipoles in the experiments. At Au-S interfaces, charge is transferred from Au to S, thus creating a surface dipole that shifts the molecular levels upward in energy. This shift depends, among other factors, on the

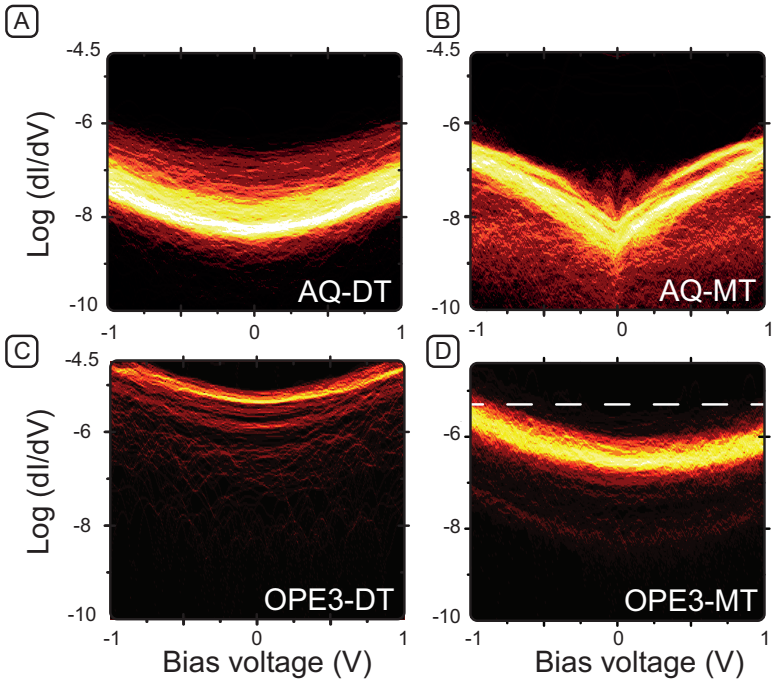

FIGURE 6.3: **Two-dimensional conductance histograms**. **A-D** show logarithmically binned 2D-histograms of dI/dV (in Ω^{-1}) vs. bias voltage V for AQ-DT (**A**), AQ-MT (**B**), OPE3-DT (**C**) and OPE3-MT (**D**). The colour scale indicates the number of counts and ranges from black (0 counts) to white (more than 40 counts). In **D**, a dashed line visualizes the asymmetry in the dI/dV-curves of OPE3-MT, resulting from asymmetric coupling. The corresponding molecular structures can be found in figure 6.1 a.

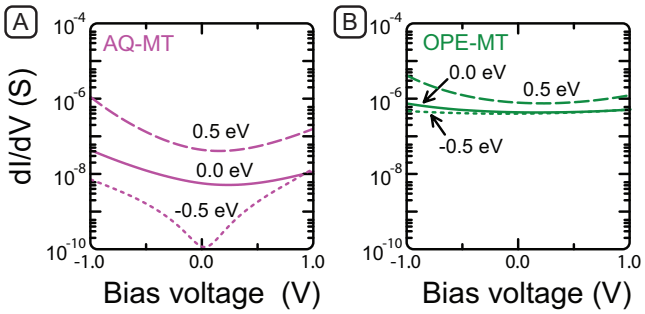

FIGURE 6.4: **Calculated dI/dV-curves for AQ-MT and OPE3-MT. A**, dI/dV for AQ-MT as computed from the transmission function in Fig. 2a. $T(E)$ was shifted by $\Delta E = 0.0$ eV, $\Delta E = 0.5$ eV and $\Delta E = -0.5$ eV, relative to E_F. We include asymmetry in the bias drop through a parameter $\eta = 0.6$ (Appendix C). To account for multiple molecules contacting the AFM-tip, we have multiplied the transmission function by a factor of 100. For $\Delta E = -0.5$ eV both the shape and the range of dI/dV, spanning two orders of magnitude, are in excellent agreement with the experiments (figure 6.3-B). **B**, Similar calculation for OPE3-MT. Asymmetric curves and higher conductance values with smaller variation are found, consistent with figure 6.3-D

surface density of molecules. The position of the anti-resonance is particularly sensitive to such effects due to the low density of states in the HOMO-LUMO gap. The computational limitation is illustrated best by comparing our calculations on AQ-DT (figure 6.2) with those in reference [22] (figure 5). In our figure 6.2, the anti-resonance lies to the right of E_F, whereas in reference [22], it lies to the left. It is thus reasonable to treat the position of the transmission minimum as a free variable within a limited energy window. In figure 6.4-A, we display dI/dV-curves for AQ-MT, calculated for three cases: no energy shift (compared to figure 6.2-A) and shifts of ± 0.5 eV. We take into account that AQ-MT molecules are probed asymmetrically. For a shift of -0.5 eV, the calculated dI/dV-characteristic is in remarkable agreement with the measured curves in figure 6.3 B. First, the V-like shape with negative curvature is reproduced. Second, the voltage scale and the range of dI/dV-values over which the minimum extends agree. Finally, the dI/dV-curves are nearly symmetric in both calculation and experiment. The latter is indeed noteworthy, since AQ-MT is contacted asymmetrically. The symmetry in figure 6.3-B must therefore be a consequence of $T(E)$ being symmetric around E_F or, equivalently, of E_F laying near the interference minimum. To independently confirm that monothiols are asymmetrically coupled, we measured dI/dV-curves for OPE3-DT (figure 6.3-C) and OPE3-MT (figure 6.3-D). As expected, symmetric data are obtained for OPE3-DT, whereas asymmetric dI/dV-curves are found for OPE3-MT (see

figure 6.4-B for calculations). Moreover in reference [34], Kim and co-workers observed linear I(V) curves around zero bias for oligoacene molecules (similar to the central part of ACDT) for both mono- and di-thiols which results in a parabolic shaped dI/dV as shown above. This reinforces the idea that the observed dip in the dI/dV is not caused by the monothiolated character of the molecules but truly a characteristic of the AQ molecules. Hence, we conclude that figure 6.3-B constitutes direct evidence for quantum interference in AQ-MT molecular junctions.

There is still the question why AQ-DT does not show a V-shaped dI/dV-curve, while its conductance is strongly suppressed. This is explained by the fact that AQ-DT junctions comprise two Au-S dipoles, whereas AQ-MT junctions have only one. Hence, in AQ-DT, the transmission dip is shifted to higher energies than in AQ-MT, i.e. it lies above E_F. In that case, no anomaly shows up in dI/dV-curves (see figure 6.4-A and Appendix C). Note that a higher energetic position of the dip of AQ-DT, compared to AQ-MT, is also predicted by our calculations (figure 6.2-A).

Now that we have direct evidence for quantum interference, the question should be asked what is needed for a full proof. One of the experiments that comes into mind is the use of a three-terminal junction set-up. Indeed the extra electrode, the gate, could be used to shift the molecular levels and so also move the interference dip in the transmission relative to the Fermi level. Indeed we have seen above that the relative position of the interference dip in the transmission function and the Fermi level are essential for the observation of the dip in the dI/dV. In this way we could show that when the levels are shifted for AQ-MT for example the characteristic dip in the dI/dV disappears. Inversely we could move the dip of AQ-DT closer to the Fermi level to make the dip in the dI/dV appear.

A second possible experiment is to look at the thermoelectric signature of the destructive interferences. Indeed by applying a temperature gradient, ΔT, between two electrodes contacting molecular species one can measure the obtained thermo-voltage, ΔV_{thermo}[35]. It has been shown that the Seebeck coefficient, $S = \Delta V_{thermo}/\Delta T$ is proportional to the slope of the transmission function at the Fermi level as shown in equation 6.1.

$$S = -\frac{\pi^2 k_B^2 T}{3e} \frac{\partial \ln(T(E))}{\partial E}\bigg|_{E=E_F} \tag{6.1}$$

As we can see in figure 6.5, we can relate the position and the sign of the Seebeck coefficient to the position of the Fermi level. For positive S, the Fermi level is located at the HOMO side of the transmission, oppositely for negative S, E_F

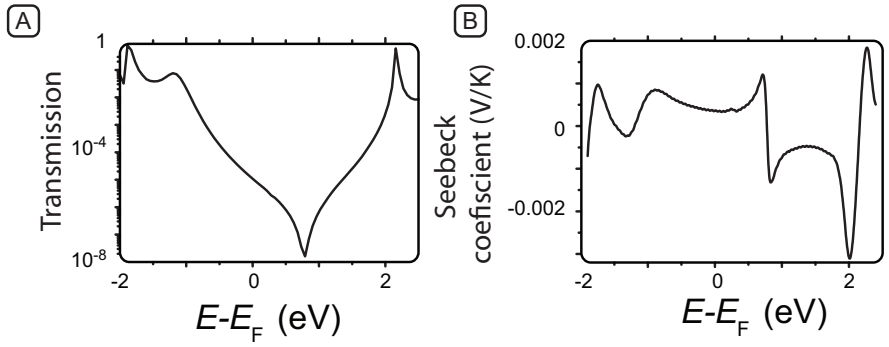

FIGURE 6.5: **Calculated transmission probability curves and Seebeck coefficient for AQ-DT. A**,transmission curves for AQ-DT calculated by DFT+Σ **B**, Corresponding Seebeck coefficient. All calculations are performed by Troels Markussen from the Danish technical university.

is located at the LUMO side of the transmission. The value of the measured S does determine the distance to the dip. Thermoelectric measurements make the determination of the Fermi level position possible.

Finally, we note that a magnetic field can not be practically used to manipulate the phase of the electrons and hence the interference.

6.5 Conclusions

In summary, our charge transport data on cross-conjugated anthraquinone derivatives are fully consistent with destructive interference in molecular junctions. The interference effects are intimately linked to the shapes and energies of the molecular orbitals and can thus be controlled by chemical design. The fact that interference in molecules is present at room temperature opens the road to a new type of molecular devices. Specifically, these include interference controlled molecular switches with very large on-off ratios[18, 23] and novel thermoelectric devices, with thermopower values tunable in magnitude and sign[36].

References

[1] R. A. Webb, S. Washburn, C. P. Umbach, and R. B. Laibowitz, *Observation of h/e Aharonov-Bohm Oscillations In Normal-metal Rings*, Physical Review Letters **54**, 2696 (1985).

[2] B. J. van Wees, H. van Houten, C. W. J. Beenakker, J. G. Williamson, L. P. Kouwenhoven, D. van der Marel, and C. T. Foxon, *Quantized conductance of point contacts in a two-dimensional electron gas*, Physical Review Letters **60**, 848 (1988).

[3] D. A. Wharam, T. J. Thornton, R. Newbury, M. Pepper, H. Ahmed, J. E. F. Frost, D. G. Hasko, D. C. Peacock, D. A. Ritchie, and G. A. C. Jones, *One-dimensional transport and the quantisation of the ballistic resistance*, Journal of Physics C: Solid State Physics **21**, L209 (1988).

[4] C. W. J. Beenakker and H. van Houten, *Quantum Transport In Semiconductor Nanostructures*, Solid State Phys. **44**, 1 (1991).

[5] P. Sautet and C. Joachim, *Electronic interference produced by a benzene embedded in a polyacetylene chain*, Chemical Physics Letters **153**, 511 (1988).

[6] D. Q. Andrews, G. C. Solomon, R. P. Van Duyne, and M. A. Ratner, *Single Molecule Electronics: Increasing Dynamic Range and Switching Speed Using Cross-Conjugated Species*, Journal of the American Chemical Society **130**, 17309 (2008).

[7] C. A. Stafford, D. M. Cardamone, and S. Mazumdar, *The quantum interference effect transistor*, Nanotechnology **18**, 424014 (2007).

[8] M. Ernzerhof, M. Zhuang, and P. Rocheleau, *Side-chain effects in molecular electronic devices*, Journal of Chemical Physics **123** (2005), ISSN 0021-9606.

[9] T. Markussen, R. Stadler, and K. S. Thygesen, *The Relation between Structure and Quantum Interference in Single Molecule Junctions*, Nano Letters **10**, 4260 (2010).

[10] T. Markussen, J. Schiotz, and K. S. Thygesen, *Electrochemical control of quantum interference in anthraquinone-based molecular switches*, Journal of Chemical Physics **132**, 224104 (pages 6) (2010).

[11] G. C. Solomon, C. Herrmann, T. Hansen, V. Mujica, and M. A. Ratner, *Exploring local currents in molecular junctions*, Nature Chemistry **2**, 223 (2010).

[12] S. Schmaus, A. Bagrets, Y. Nahas, T. K. Yamada, A. Bork, M. Bowen, E. Beaurepaire, F. Evers, and W. Wulfhekel, *Giant magnetoresistance through a single molecule*, Nature Nanotechnology **6**, 185 (2011).

[13] R. H. M. Smit, Y. Noat, C. Untiedt, N. D. Lang, M. C. van Hemert, and J. M. van Ruitenbeek, *Measurement of the conductance of a hydrogen molecule*, Nature **419**, 906 (2002).

[14] S. Kubatkin, A. Danilov, M. Hjort, J. Cornil, J. L. Bredas, N. Stuhr-Hansen, P. Hedegard, and T. Bjornholm, *Single-electron transistor of a single organic molecule with access to several redox states*, Nature **425**, 698 (2003).

[15] L. Venkataraman, J. E. Klare, I. W. Tam, C. Nuckolls, M. S. Hybertsen, and M. L. Steigerwald, *Single-molecule circuits with well-defined molecular conductance*, Nano Letters **6**, 458 (2006).

[16] E. A. Osorio, K. O'Neill, M. Wegewijs, N. Stuhr-Hansen, J. Paaske, T. Bjornholm, and H. S. J. van der Zant, *Electronic excitations of a single molecule contacted in a three-terminal configuration*, Nano Letters **7**, 3336 (2007).

[17] A. Mishchenko, D. Vonlanthen, V. Meded, M. Burkle, C. Li, I. V. Pobelov, A. Bagrets, J. K. Viljas, F. Pauly, F. Evers, et al., *Influence of Conformation on Conductance of Biphenyl-Dithiol Single-Molecule Contacts*, Nano Letters **10**, 156 (2010).

[18] S. J. van der Molen and P. Liljeroth, *Charge transport through molecular switches*, Journal Of Physics-Condensed Matter **22**, 133001 (2010).

[19] C. Patoux, C. Coudret, J. P. Launay, C. Joachim, and A. Gourdon, *Topological effects on intramolecular electron transfer via quantum interference*, Inorganic Chemistry **36**, 5037 (1997).

[20] A. B. Ricks, G. C. Solomon, M. T. Colvin, A. M. Scott, K. Chen, M. A. Ratner, and M. R. Wasielewski, *Controlling Electron Transfer in Donor-Bridge-Acceptor Molecules Using Cross-Conjugated Bridges*, Journal of the American Chemical Society **132**, 15427 (2010).

[21] M. Mayor, H. B. Weber, J. Reichert, M. Elbing, C. von Hanisch, D. Beckmann, and M. Fischer, *Electric current through a molecular rod - Relevance of the position of the anchor groups*, Angewandte Chemie, International Edition **42**, 5834 (2003).

[22] D. Fracasso, H. Valkenier, J. C. Hummelen, G. C. Solomon, and R. C. Chiechi, *Evidence for Quantum Interference in SAMs of Arylethynylene Thiolates in Tunneling Junctions with Eutectic GaIn (EGaIn) Top-Contacts*, Journal of the American Chemical Society **133**, 9556 (2011).

[23] E. H. van Dijk, D. J. T. Myles, M. H. van der Veen, and J. C. Hummelen, *Synthesis and Properties of an Anthraquinone-Based Redox Switch for Molecular Electronics*, Organic Letters **8**, 2333 (2006).

[24] M. Gholami and R. R. Tykwinski, *Oligomeric and polymeric systems with a cross-conjugated pi-framework*, Chemical Reviews **106**, 4997 (2006).

[25] H. Valkenier, E. H. Huisman, P. A. van Hal, D. M. de Leeuw, R. C. Chiechi, and J. C. Hummelen, *Formation of High-Quality Self-Assembled Monolayers of Conjugated Dithiols on Gold: Base Matters*, Journal of the American Chemical Society **133**, 4930 (2011).

[26] D. J. Wold and C. D. Frisbie, *Fabrication and characterization of metal-molecule-metal junctions by conducting probe atomic force microscopy*, Journal of the American Chemical Society **123**, 5549 (2001).

[27] M. T. Gonzalez, S. M. Wu, R. Huber, S. J. van der Molen, C. Schonenberger, and M. Calame, *Electrical conductance of molecular junctions by a robust statistical analysis*, Nano Letters **6**, 2238 (2006).

[28] U. Fano, *Effects of Configuration Interaction on Intensities and Phase Shifts*, Physical Review **124**, 1866 (1961).

[29] A. E. Miroshnichenko, S. Flach, and Y. S. Kivshar, *Fano resonances in nanoscale structures*, Reviews Of Modern Physics **82**, 2257 (2010).

[30] S. J. van der Molen, J. Liao, T. Kudernac, J. S. Agustsson, L. Bernard, M. Calame, B. J. van Wees, B. L. Feringa, and C. Schoenenberger, *Light-Controlled Conductance Switching of Ordered Metal-Molecule-Metal Devices*, Nano Letters **9**, 76 (2009).

[31] R. H. Goldsmith, M. R. Wasielewski, and M. A. Ratner, *Electron transfer in multiply bridged donor-acceptor molecules: Dephasing and quantum coherence*, Journal Of Physical Chemistry B **110**, 20258 (2006).

[32] D. Q. Andrews, G. C. Solomon, R. H. Goldsmith, T. Hansen, M. R. Wasielewski, R. P. Van Duyne, and M. A. Ratner, *Quantum Interference: The Structural Dependence of Electron Transmission through Model Systems and Cross-Conjugated Molecules*, Journal Of Physical Chemistry C **112**, 16991 (2008).

[33] T. Markussen, private communications.

[34] B. Kim, S. H. Choi, X. Y. Zhu, and C. D. Frisbie, *Molecular tunnel junctions based on pi-conjugated oligoacene thiols and dithiols between ag, au, and pt contacts: effect of surface linking group and metal work function*, Journal Of The American Chemical Society **133**, 19864 (2011).

[35] R. Pramod, J. Sung-Yeon, R. A. Segalman, and A. Majumdar, *Thermoelectricity in molecular junctions*, Science **315**, 1568 (2007).

[36] J. P. Bergfield and C. A. Stafford, *Thermoelectric Signatures of Coherent Transport in Single-Molecule Heterojunctions*, Nano Letters **9**, 3072 (2009).

A

How to synthesize superior gold nanoparticles

A.1 Ingredients

Serves 100 ml gold nanoparticles in water with approximatelly 10^{13} particles.ml^{-1} (stock solution). To transfer the nanoparticles to a chloroform solution we use 10 centrifuge tubes of 1 ml. Takes $\approx \frac{1}{2}$ day.

- 79 ml ultra-pure water (18.2 $\Omega.m^{-1}$)
- 1 ml $HAuCl_4$ solution (1% weight/volume in ultra-pure water)
- 80 μl tannic acid solution (1% weight/volume in ultra-pure water)
- 4 ml trisodium citrate (1% weight/volume in ultra-pure water)
- 16 ml ultra-pure water
- 0.194 ml octanethiol
- 22 ml ethanol (Ar flushed)
- 8 ml chloroform

- 2 Erlenmeyer
- 1 magnetic stirrer
- 1 heating plate with magnetic stirrer
- 10 eppendorf centrifuge tubes (2 ml)
- 1 centrifuge
- 1 water-cooled ultrasonic bath
- 1 glass vial
- water-cooled reflux
- nitrogen flushed glove box

A.2 Gold nanoparticles in water

- In one Erlenmeyer mix the $HAuCl_4$ solution with the 79 ml water and heat up to 60° C on the heating plate.
- In the other Erlenmeyer mix the tannic acid, the trisodium citrate and the 16 ml water and heat as well up to 60° C on the heating plate.
- When both solutions are at 60° C, mix the two solution using the magnetic stirrer and bring to boiling point with the reflux connected.
- Keep boiling for 10 minutes. The solution will turn from blue purple to rubby red.
- Let the solution cool down to RT while stirring.
- This solution of nanoparticles in water is stable for month in the refrigerator.

A.3 Gold nanoparticles in chloroform

- Divide 20 ml gold NP solution into 10 centrifuge tubes
- Centrifuge for 60 minutes, at 10 ° C at 15000 rpm
- While centrifuging make the octanethiol solution in ethanol (0.14 M). Mix 0.194 ml octanethiol in 8 ml ethanol in the glove box.

- Remove the suppernattant (water) from the centrifuge tubes.
- Add 1.5 ml ethanol (nitrogen flushed) into each tube and shake.
- Collect the solution from all the tubes into a glass vial. Put in the ultrasonic bath for 10 seconds.
- Add the octanethiol solution to the vial at once. Put in the ultrasonic bath for 10 seconds. Keep in refrigerator for at least 2 days.
- Once the nanoparticles are sedimented (black residue on the bottom of the vial), remove the ethanol and replace with the chloroform. Put in the cooled ultrasonic bath for 1 hour (recovered ruby red colour).
- The nanoparticles are ready to use, enjoy!

B

THE SIMMONS MODEL

Full formulation of the Simmons formula. According to ref [1], a full expression for the current density, J, through a barrier between two similar metal electrodes over the entire voltage range is given by:

$$\begin{aligned} J &= c\{\tilde{A}+\tilde{B}+\tilde{C}\} \\ c &= \frac{4\pi me}{h^3} \\ \tilde{A} &= eV\int_0^{\eta-eV} exp(-A\sqrt{\eta+\bar{\phi}-E_x})dE_x \\ \tilde{B} &= -\bar{\phi}\int_{\eta-eV}^{\eta} exp(-A\sqrt{\eta+\bar{\phi}-E_x})dE_x \\ \tilde{C} &= \int_{\eta-eV}^{\eta}(\eta+\bar{\phi}-E_x)exp(-A\sqrt{\eta+\bar{\phi}-E_x})dE_x. \end{aligned}$$

Here, $A = (4\pi\Delta s/h)\sqrt{2m}$, where $\Delta s = s_2 - s_1$ is the width of the barrier at the Fermi energy of the metal and $\bar{\phi}$ is the average barrier height. In ref [1], parts of the integrands are neglected. The consequence of this is that for small A and/or small ϕ, the commonly used Simmons expression gives unphysical results. Below, we calculate the full integrands.
$\tilde{A}$ and $\tilde{B}$ are of the same form:

$$-\int_{e_1}^{e_2} exp(-A\sqrt{\eta+\bar{\phi}-E_x})d(-E_x) > 0$$

By substituting $y^2 = \eta + \bar{\phi} - E_x$ and $d(-E_x) = d(\eta + \bar{\phi} - E_x) = dy^2 = 2ydy$, this becomes:

$$-\int_{y_1}^{y_2} exp(-Ay) \cdot 2ydy$$

B

Here, $y_{1,2} = \sqrt{\eta + \bar{\phi} - e_{1,2}}$. These integrals can be solved by partial integration [1]. Boundaries for $\tilde{A}$ are $e_1 = 0$, $e_2 = \eta - eV$, $y_1 = \sqrt{\eta + \bar{\phi}}$, $y_2 = \sqrt{\bar{\phi} + eV}$, yielding:

$$\tilde{A} = \frac{2eV}{A^2}\{(A\sqrt{\bar{\phi} + eV} + 1)exp(-A\sqrt{\bar{\phi} + eV}) - (A\sqrt{\eta + \bar{\phi}} + 1)exp(-A\sqrt{\eta + \bar{\phi}})\}.$$

Boundaries for $\tilde{B}$ are $e_1 = \eta - eV$, $e_2 = \eta$, $y_1 = \sqrt{\bar{\phi} + eV}$, $y_2 = \sqrt{\bar{\phi}}$, yielding:

$$\tilde{B} = \bar{\phi}\frac{2}{A^2}\{(A\sqrt{\bar{\phi}} + 1)exp(-A\sqrt{\bar{\phi}}) - (A\sqrt{\bar{\phi} + eV} + 1)exp(-A\sqrt{\bar{\phi} + eV})\}.$$

Like $\tilde{A}$ and $\tilde{B}$, $\tilde{C}$ can again be solved by substituting $y^2 \equiv \eta + \bar{\phi} - E_x$ and $d(-E_x) = d(\eta + \bar{\phi} - E_x)$ and partial integration.

$$\tilde{C} = -2\int_{y_1}^{y_2} y^3 exp(-Ay)dy$$

Boundaries for $\tilde{C}$ are $e_1 = \eta - eV$, $e_2 = \eta$, $y_1 = \sqrt{\bar{\phi} + eV}$, $y_2 = \sqrt{\bar{\phi}}$, so that:

$$\begin{aligned}\tilde{C} = \frac{2}{A}\{&(\bar{\phi}^{3/2} + \frac{3}{A}\bar{\phi} + \frac{6}{A^2}\sqrt{\bar{\phi}} + \frac{6}{A^3})exp(-A\sqrt{\bar{\phi}}) \\ &-((\bar{\phi} + eV)^{3/2} + \frac{3}{A}(\bar{\phi} + eV) + \frac{6}{A^2}\sqrt{\bar{\phi} + eV} + \frac{6}{A^3})exp(-A\sqrt{\bar{\phi} + eV}))\}\end{aligned}$$

Taking all integrals together, we can calculate J. Note that for relatively high and/or thick barriers, i.e. if $A\sqrt{\phi \pm eV} \gg 1$, the full expression for J reduces to eq. (26) of reference [1]:

$$\begin{aligned}J = J_0\{&(\phi - eV/2)exp(-A\sqrt{\phi - eV/2}) - \\ &(\phi + eV/2)exp(-A\sqrt{\phi + eV/2})\}.\end{aligned}$$

where, $J_0 = e/(2\pi hs^2)$.

Figure 1 shows V_m versus 1/d for each of the three equations mentioned above; eq. 26 of ref [1], (black), eq. 1 (Stratton) in the main text (blue) and the full Simmons expression (red). For thick barriers all three collapse on a single line. The maximum deviation between the three is in the order of a few percent for thin barriers (around $d = 5$Å). These differences are negligible compared to the spread in the experimental data as discussed in the Letter.

References

[1] J. G. SIMMONS, *Generalized Formula For Electric Tunnel Effect Between Similar Electrodes Separated By A Thin Insulating Film*, Journal Of Applied Physics **34**, 1793 (1963).

C

Complementary information on chapter 6

C.1 Formation and analysis of the Self -Assembled Monolayers

Self-Assembled Monolayers (SAMs) of the acetyl-protected mono- and dithiols were grown from solutions with triethylamine as deprotecting agent, which promotes the formation of high-quality and densely-packed SAMs, as recently showed for acetyl-protected OPE dithiols and monothiols[1]. Due to the low solubility of the AC- and AQ-compounds in THF, these SAMs were grown from 0.5 mM solutions in chloroform (Aldrich, anhydrous, =99%, stabilized by amylenes) with 10% (v/v) triethylamine (Fisher, HPLC grade, degassed) added. The SAMs of the OPE mono- and dithiol were grown from 0.5 mM solutions in dry THF, with 10% (v/v) triethylamine added. All solutions and SAMs were prepared inside a glovebox filled with nitrogen (<5 ppm O_2). We used freshly prepared samples of 150 nm gold on mica for the ellipsometry and XPS studies, and freshly prepared samples of 5 nm chromium and 200 nm gold thermally deposited on a silicon wafer for the CP-AFM studies. Samples were immersed upside down for two nights in about 3 mL solution. After this immersion time, the samples were taken from solution, rinsed three times with clean THF, and dried on the nitrogen atmosphere in the glovebox.

Ellipsometry measurements were performed using a V-Vase from J. A. Woollam Co., Inc. in air. Measurements were acquired from 300-800 nm with an interval of 10 nm at 65, 70, and 75 ° angle of incidence. For every set of experiments a fresh gold-on-mica sample was measured at three or four different spots. The data from these measurements were merged and the optical constants were fitted. For every SAM three spots were measured and the thickness of a cauchy layer (n=1.55, k=0 at all λ) on top of the gold layer was fitted and averaged over the three spots.

X-ray Photoelectron Spectroscopy (XPS) measurements were performed on a X-PROBE Surface Science Laboratories photoelectron spectrometer with a Al Ka X-ray source (1486.6 eV) and a takeoff angle of 37ž. We accumulated 20 scans for S2p, 10 for C1s, 10 for O1s, 15 for N1s, and 5 for Au4f. All reported data are averaged over four different spots per sample and presented in table C.1. WinSpec[1] was used to fit the recorded data with a background and minimum number of mixed Gaussian-Lorentzian singlets (C1s, N1s, O1s) or doublets (Au4f; Δ=3.67 eV, S2p; Δ=1.18 eV) with a width of 1.21 eV.

Molecular wire	**Au4f** (84 eV)	**C1s** CxHx (283 -287 eV)	**C1s** C=O (288 eV)	**S2p** S-Au (162 eV)	**S2p** S-R (164 eV)	**O1s** (532 eV)	Normalized intensities **C1s** per C-atom
AC-DT	7515	1343	39	19	84	57	43
AQ-DT	7564	1017	73	18	55	102	36

TABLE C.1: Composition of the SAM's: X-ray photoelectron spectroscopy measurements. The integrated intensities are divided by the sensitivity factor: 1 for C1s, 1,79 for S2p and 2,49 for O1s

We determined the thicknesses of the SAMs from our XPS results by two different methods: A) from the ratio between the carbon and the gold signals[2] and B) from the attenuation of the gold signals[3].
Method A. Thicknesses of the SAMs(d_{CS}) are determined from the ratio of the areas of C1s and Au4f peaks by equation C.1 with λ_{Au} = 31 Å, λ_C = 27 Å, d_C = d_{CS} − 1.8 Å(d_C is the thickness of the hydrocarbon layer without the thiolate); k is estimated to be 0.15 from XPS measurements on a SAM of undecanethiol

[1]WinSpec 2.09, developed at Laboratoire Interdépartemental de Spectroscopie Electronique, Namur, Belgium

on gold. We determined d_{CS} from I_C/I_{Au} by an iterative numerical approach.

$$\frac{I_c}{I_{Au}} = k\frac{1-\exp(\frac{-d_c}{\lambda_C})}{\exp(\frac{-d_{CS}}{\lambda_{Au}})} \tag{C.1}$$

Method B. Thicknesses (d) are determined from the attenuation of the Au4f signal by equation C.2 with Au0 = 109754, λ = 42 Å, and θ = 37ř.

$$I_{Au} = I_{Au0}\exp(\frac{-d}{\lambda sin\theta}) \tag{C.2}$$

We found a good agreement between the length of the molecules and the thickness of the SAMs, indicating the formation of densely-packed monolayers in which the molecules are oriented nearly perpendicular to the gold substrate surface.

Molecular wire	Length[a] (Å)	Ellipsometry (Å)	XPS method A (Å)	XPS method B (Å)	Weighed Average[b] (Å)
AC-DT	24.49	28.6*	24.1	27.1	25
AQ-DT	24.49	21.7	20.1**	26.9	24
OPE-DT	20.14	19.7	17.5	17.8	19

TABLE C.2: a: The distance from S- to S-atom as obtained by DFT calculations.
b: The thicknesses as obtained by ellipsometry and XPS are averaged. The absolute values obtained from XPS by method A are considered more accurate than those obtained by method B and therefore weighed twice as strong. Identical weights were used for ellipsometry and XPS (methods A and B combined).
*: The value for **AC-DT** as determined by ellipsometry is not included in the average, since this large (highly reproducible) value is likely to be caused by the optical absorption of this compound in the range of the ellipsometry measurement.
: The value for **AQ-DT as determined by XPS method A is not included in the average, because the oxygen atoms from the anthraquinone core do attenuate the Au signal, but do not contribute to the carbon signal, underestimating the actual thickness.

The SAMs of the monothiolated molecular wires were measured by ellipsometry. The thickness of the SAMs was 17.5 Åfor **AQ-MT** and 20.5 Åfor **OPE-DT**.

From the XPS data, the ellipsometry measurements and DFT calculations we find a densely packed, upright standing SAM for AQ-DT and AC-DT.

C.2 DATA ANALYSIS

The current-voltage data gathered for each sample are put together and analyzed further using a MatLab code. For the figures in the main text, around 95

% of the measured curves are used. A small number of curves have been removed. The curves showing no contact with molecules i.e. below the noise level of our set-up (typically ≈ 100 pA) are removed from our data set. In fact this is the case when no contact is formed with the SAM. Additionally we removed the curves presenting saturation, indicating direct contact between the tip and the gold bottom electrode. In figureC.1 we show typical single I(V) curves of data kept and removed. table II summarizes the amount of removed data, which is typically as little as 5 % of the data.

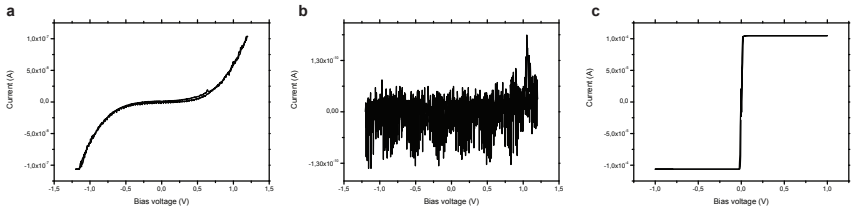

FIGURE C.1: **a**, typical I(V) curve kept in our data set for **AQ-MT**, **b**, typical I(V) curve below detection limit of our set-up, **c**, typical I(V) curve showing saturation of the current amplifier for **AQ-MT**.

Molecule	number of curves	number of curves rejected	% rejected
AC-DT	1979	98	4.9 %
AQ-DT	2502	107	4.3%
AQ-MT	2884	251	8.7%
OPE3-DT	621	32	5.1%
OPE3-MT	1574	65	4.1%

TABLE C.3: table showing the amount of curves disregarded due to no contact or saturation for the different molecules measured

Second the remaining I(V) curves are smoothed with a local regression using weighted linear least squares and a 2nd degree polynomial model. Next we take a numerical derivative of the current relative to the voltage (dI/dV). Finally we construct a 2D histogram of these dI/dV values by logarithmically binning them for each bias voltage and plotting them next to each other. This will result in a 3D graph with on the x-axis the bias voltage, on the y-axis the log (dI/dV) and on the z-axis (in colour scale) the number of counts. Such a 2D histogram can be seen as a collection of traditional 1D conductance histograms

for different bias voltages. In figureC.2 we show such 2D histogram for **AQ-MT** for both the full data set (figureC.2a) and the partial data set (figureC.2b). It is clear from this comparison that removing the contacted and saturated curves makes the picture more clear. However in the full data set plot the trend in the dI/dV curve is still easily distinguishable. We also refer to the section Supplementary Figures, where we display raw I(V)-curves, both as an ensemble and individually, and present alternative methods of analyzing the data.

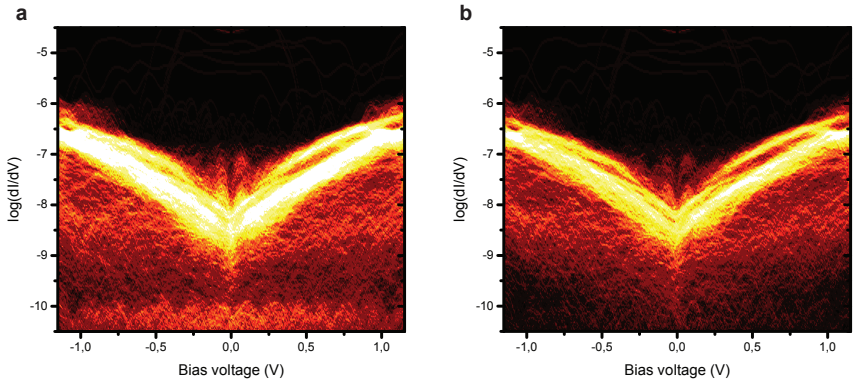

FIGURE C.2: dI/dV (Ω^{-1}) 2D histogram for **AQ-DT a**, without data rejected and **b**, with data rejected i.e. the curves with no contact and the saturated curves

C.3 CALCULATIONS

Below we present our conductance calculations in more detail. Furthermore, we elaborate on the relationship between the transmission function $T(E)$ and dI/dV-curves.

C.4 TRANSMISSION CALCULATIONS

The conductance is calculated using DFT in combination with a non-equilibrium Green function (NEGF) method as described in Ref. [4]. Our DFT-NEGF method is implemented in GPAW, which is a real space electronic structure code based on the projector augmented wave method [5, 6]. We use the Perdew-Burke-Ernzerhof (PBE) exchange-correlation functional [7], and a 4×4 k-point sampling in the surface plane. The electronic wave functions are expanded in an atomic orbital basis [6]. All atoms are described by a double-zeta plus polarization (dzp) basis set. We initially relax the molecule and the two closest Au layers until the forces on the atoms are less than 0.05 eV/Å. In the relaxed configuration, the S-atoms bind to Au at a bridge site slightly shifted toward the hollow site.

Following the standard DFT-Landauer approach, we calculate the zero-bias transmission function,

$$T(E) = \mathrm{Tr}[\mathbf{G}^r(E)\Gamma_L(E)\mathbf{G}^a(E)\Gamma_R(E)], \tag{C.3}$$

with $\mathbf{G}^r(E) = (E\mathbf{S} - \mathbf{H} - \Sigma_L(E) - \Sigma_R(E))^{-1}$ being the retarded Green's function for the junction (scattering region) described by the single-particle Hamiltonian $\mathbf{H}$ and overlap matrix $\mathbf{S}$, and where the semi-infinite electrodes are included through left and right self-energies, $\Sigma_{L,R}(E)$. The advanced Green's function $\mathbf{G}^a(E) = (\mathbf{G}^r(E))^\dagger$, and $\Gamma_{L,R}(E) = i(\Sigma_{L,R}(E) - \Sigma_{L,R}(E)^\dagger)$. The low-bias conductance can finally be obtained from the Landauer formula, $G = (2e^2/h)T(E_F)$, where E_F is the Fermi energy.

The DFT transmission for **AC-DT**, **AQ-DT**, and **AQ-MT** is shown in figureC.3.

C.5 CORRECTION OF HOMO-LUMO GAP

It is well known that DFT is unable to accurately describe energy gaps and level alignment of molecules at surfaces [8]. To correct for this inability we use a self-energy correction scheme (DFT+Σ) that has recently been shown to predict conductance values in good agreement with single-molecule experiments [9, 10]. In the DFT+Σ approach we initially correct the gas phase HOMO-LUMO gap.

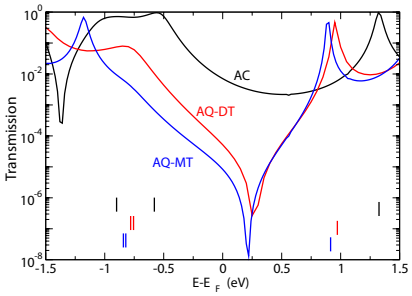

FIGURE C.3: Transmission function vs. energy calculated with with standard DFT + NEGF methods. The vertical bars mark the HOMO and HOMO-1 (to the left) and LUMO (to the right) positions. The qualitative shapes of the transmission functions are the same as for the DFT+Σ results shown in the main text, Fig. 2 (a)

This is done by calculating the ionization potential (IP) and electron affinity (EA) from total energy calculation:

$$\text{IP} = E(+e) - E(0) \tag{C.4}$$

$$\text{EA} = E(0) - E(-e), \tag{C.5}$$

where $E(0)$ is the total energy of the neutral molecule, $E(+e)$ is the energy of the molecule with one electron removed (i.e. positively charged), and $E(-e)$ is the total energy of the molecule with one extra electron on it. The gas phase HOMO-LUMO gap is calculated as ΔE =IP-EA. The calculated values are shown in tableC.4. ε_{LUMO}, corresponding to the highest occupied and lowest unoccupied eigenstates. As shown in tableC.4, the corresponding HOMO-LUMO gaps, $\Delta\varepsilon$, are significantly lower than the ones calculated from total energies, and the self-energy correction should thus shift the occupied states down in energy and the unoccupied states up in energy thereby opening the gap. When a molecule is brought close to a metallic surface, image charge interactions will further change the energy levels resulting in a shift of the occupied levels *up* in energy and the unoccupied states *down* in energy. From a simple electrostatic model [9] we get that the electrostatic interactions closes the HOMO-LUMO gap of **AC-DT** and **AQ-DT** by $\Delta_q = 1\,\text{eV}$ in total: 0.5 eV upward shift of the occupied and -0.5 eV downward shift of the unoccupied states. The electrostatic interaction is slightly larger for the OPEs because they are shorter, and we get a gap closing of $\Delta_q = 1.2\,\text{eV}$ in total. The resulting shifts of occupied states is then

$$\Sigma_{occ} = -IP - \varepsilon_H + \Delta_q/2 \tag{C.6}$$

	IP	EA	ΔE	ε_H	ε_L	$\Delta\varepsilon$	Σ_{occ}	Σ_{unocc}	$T_0(E_F)$	$T_\Sigma(E_F)$
AC	6.20	1.59	4.61	-4.87	-3.08	1.79	-0.83	0.99	$7.1\cdot10^{-3}$	$0.5\cdot10^{-3}$
AQ-DT	6.44	2.21	4.23	-5.42	-3.84	1.58	-0.52	1.13	$4.6\cdot10^{-5}$	$1.1\cdot10^{-5}$
AQ-MT	6.73	2.21	4.52	-5.46	-3.87	1.59	-0.77	1.16	$8.3\cdot10^{-6}$	$5.7\cdot10^{-7}$
OPE-DT	6.45	1.22	5.23	-4.99	-2.78	2.21	-0.86	0.96	$1.6\cdot10^{-2}$	$1.7\cdot10^{-3}$
OPE-MT	6.64	1.19	5.46	-5.08	-2.79	2.29	-0.96	1.01	$6.2\cdot10^{-4}$	$5.5\cdot10^{-5}$

TABLE C.4: Ionization potential (IP), electron affinity (EA), and corresponding HOMO-LUMO gap, ΔE, obtained from total energy calculations. Kohn-Sham HOMO, ε_H, LUMO, ε_L energy and corresponding gap, $\Delta\varepsilon$. In the DFT+Σ method, the occupied (unoccupied) states are shifted by Σ_{occ} (Σ_{unocc}). $T_0(E_F)$ is the pure DFT transmission values at the Fermi energy and $T_\Sigma(E_F)$ is the value obtained with the DFT+Σ approach. All energies are given in units of eV.

C

and of the unoccupied states

$$\Sigma_{unocc} = EA + \varepsilon_L - \Delta_q/2. \tag{C.7}$$

The calculated values are shown in tableC.4. When comparing the DFT+Σ transmissions in the main text, Fig. 2(a) with the pure DFT results in figureC.3 we see that the effect of Σ merely is to shift the occupied states down in energy and the unoccupied states up in energy. While the qualitative behaviour and the shape of the transmission functions are relatively unchanged the overall magnitude and quantitative details are changed. Previous studies [9, 10] have shown that DFT+Σ yields better agreement with experiments.

figureC.4 shows the OPE transmissions calculated with the DFT+Σ method.

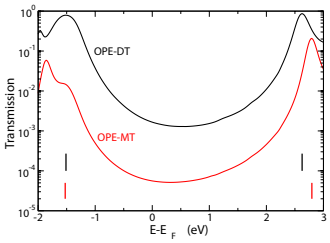

FIGURE C.4: Transmission function calculated with DFT+Σ for **OPE-DT** and **OPE-MT**.

C.6 dI/dV CURVES

We calculate current-voltage relations from the low-bias transmission function. As discussed in the main text, we allow for an energy shift ΔE of the Fermi level. We also allow for an asymmetric voltage drop at the left and right electrodes described by the parameter η. Based on previous finite bias DFT calculations[11]

on similar molecules, we use an estimated value of $\eta = 0.6$ for all the mono-thiols. The main conclusions are, however, independent of this specific choice. For the di-thiols we assume a symmetric voltage drop with $\eta = 1/2$.

The current is calculated as

$$I(V) = \frac{2e}{h} \int_{-\infty}^{\infty} T(E + \Delta E) \{ f_L[V\eta] - f_R[V(\eta - 1)] \} \, \mathrm{d}E, \tag{C.8}$$

where $f_{L/R}(V) = 1/[\exp(E_F + eV)/k_B T + 1]$ are the Fermi-Dirac distributions for the left and right contact. The $\mathrm{d}I/\mathrm{d}V$ curves are found by differentiation of (C.8). Results for AQ-MT and OPE-MT are shown in the main text (Fig. 4), while $\mathrm{d}I/\mathrm{d}V$ curves for AQ-DT, AC-DT, and OPE-DT are shown in figureC.5, for various values of ΔE.

The most important case is that of AQ-DT (left panel). Let us extend the discussion at the end of the main paper while inspecting figure C.5. Just like for AQ-MT (see Fig. 4a), we see that for AQ-DT, the shape of the $\mathrm{d}I/\mathrm{d}V$ curves depends strongly on the energy shift ΔE. For $\Delta E = -0.7$ eV, the calculations of $\mathrm{d}I/\mathrm{d}V$ yield a clear zero-bias anomaly for AQ-DT. The reason is that in that case, the dip in the transmission function $T(E)$ lies very close to the Fermi level (in the section below, we go into this more generally). However, for other values of ΔE, the shape of the $\mathrm{d}I/\mathrm{d}V$ curves tends towards a parabola-like curve. The latter is in correspondence with our measurements in Fig. 3a, where we find a strongly suppressed conductance for AQ-DT (with respect to AC-DT), but no zero-bias anomaly. In other words, although both AQ-DT and AQ-MT exhibit quantum interference, the zero-bias anomaly is only visible for AQ-MT, since for that molecule the transmission dip is much closer to E_F.

Of course, we need to consider the question why the transmission minimum is shifted to different positions for AQ-DT and AQ-MT. This is explained by the fact that AQ-DT junctions comprise two Au-S dipoles, whereas AQ-MT junctions have only one. The accompanying charge transfer results in a higher upward energy shift for the transmission function of AQ-DT than for AQ-MT (by ≈ 0.2 eV in our calculations). Hence, in AQ-DT, the transmission dip is positioned more above E_F. Consequently, no anomaly shows up in dI/dV-curves as illustrated in figure C.5. Interestingly, the inherent difference in charge transfer for AQ-DT and AQ-MT implies that it is very unlikely to see a zero-bias anomaly in the dI/dV-curves of both AQ-DT and AQ-MT.

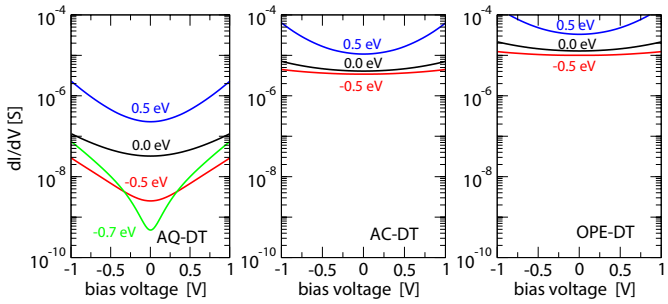

FIGURE C.5: dI/dV -curves calculated from the transmission function shifted by $\Delta E = 0.0$ eV $\Delta E = 0.5$ eV and $\Delta E = -0.5$ eV, relative to the Fermi energy. In the case of AQ-DT (left panel), we also show the result for $\Delta E = -0.7$ eV to illustrate that a dI/dV dip similar to that experimentally seen for AQ-MT could in principle be observed for AQ-DT, with a larger energy shift. In order to simulate the experimental situation with multiple molecules in contact with the AFM tip, the DFT+Σ transmission functions have been multiplied by a factor of 100.

C.7 RELATIONSHIP BETWEEN dI/dV CURVES AND THE POSITION OF THE MINIMUM IN T(E)

In the previous section, we stated that an anti-resonance in $T(E)$ leads to an anomaly in dI/dV only if this anti-resonance is situated near the Fermi level. Here, we discuss this relationship further, first mathematically, then with a model calculation.

Mathematically, the relation between $\mathrm{d}I/\mathrm{d}V$ and $T(E)$ can be written (using the Landauer formula at $T = 0$K) as:

$$\frac{\mathrm{d}I}{\mathrm{d}V} = \frac{2e^2}{h}(\eta T(E_F + \eta eV) + (1-\eta)(T(E_F - (1-\eta)eV))) \tag{C.9}$$

where η expresses the symmetry of the junction ($\eta = 0.5$ for a symmetric junction). As a first consequence, symmetric $\mathrm{d}I/\mathrm{d}V$-curves are necessarily obtained for symmetrically coupled molecules, irrespective of the (a)symmetry of T(E) around the Fermi level E_F. This is easily seen by inserting $\eta = 0.5$ into the formula above, and interchanging +V and -V.

Indeed, from eq. C.9, we can also see that if the dip in $T(E)$ is located at or near E_F, the $\mathrm{d}I/\mathrm{d}V$-curves will show a zero-bias anomaly. However, if the anti-resonance of $T(E)$ does not lie close to E_F, no dip will be observed in $\mathrm{d}I/\mathrm{d}V$. To understand this, let us suppose the transmission dip is significantly above E_F, at a distance δE. Then, it will come inside the bias window at a bias voltage

$eV = \delta E/\eta$. At this voltage, the first term in the expression will obviously become very small. However, there is still the second term (the negative border of the bias window), which will not be small at all (cf. Fig. 2a and note the logarithmic scale). Hence, the second term will dominate the conductance and the dip is washed out. We note that this reasoning also holds if the dip in $T(E)$ is below E_F, provided the molecular junctions are nearly-symmetrically coupled. Only if the asymmetry is very strong ($\eta = 0$ or $\eta = 1$), one could probe a dip at non-zero biases. However, this limit is only attained under strong tunnelling conditions and it is not relevant for the junctions considered here. For our experiments, we have η between symmetric (0.5, for dithiols) and moderately asymmetric (0.6, monothiols).

To further illustrate this, we make use of a model tight binding calculation of $T(E)$. In figureC.6 (left panel), we show three transmission functions, that differ only by a shift in energy. Three cases are chosen: one in which the minimum of $T(E)$ is exactly at E_F (red), one where it is 0.4 eV below E_F (black), and one where it is 0.2 eV above E_F. The peaks where $T(E) = 1$ correspond to the position of the HOMO and LUMO resonances. The resulting dI/dV-curves are shown in the right panel of figureC.6 (same colour coding). These dI/dV-curves have been calculated from formula (C.8) using asymmetry parameters of $\eta = 0.5$ (full line) and $\eta = 0.6$ (dashed line). These values correspond to voltage drop occurring symmetrically and slight asymmetrically over the molecule, respectively. The symmetric choice applies to our dithiol bonded jucnctions while the slightly asymmetric corresponds to our monothiol bonded junctions. The value $\eta = 0.6$ is estimated on basis of first-principles finite bias calculations for similar molecular junctions [11].

It is clear from figureC.6 that the characteristic V-shape in the dI/dV, observed for AQ-MT in Fig. 3 of the main paper, only appears when the transmission node is positioned close to the Fermi energy. When the transmission node appears below or above the Fermi energy, the shape of the dI/dV is parabola-like, similar to that observed for the conjugated molecules OPE3 and AC, see Figs. 3c-d and Fig. 1c. This shows that the presence of QI is a necessary but not a sufficient condition for observing a dip in the dI/dV curve. In particular it shows that in cases where the transmission dip lies away from the Fermi energy, destructive QI would reveal itself as a strong reduction of the numerical value of the conductance rather than a qualitative effect on the dI/dV-curve. This is indeed what we observe experimentally for AQ-DT.

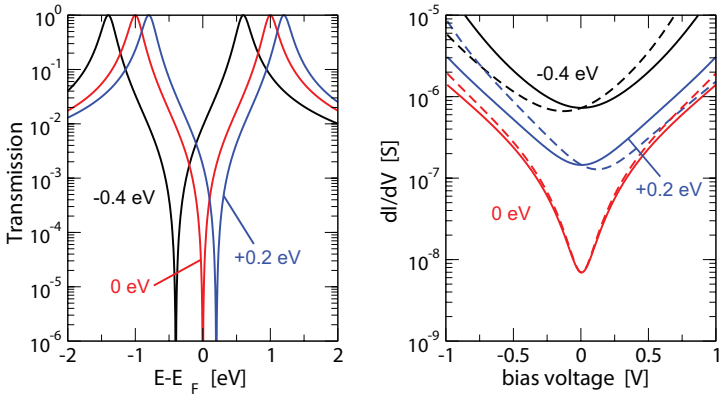

FIGURE C.6: Left panel: Calculated transmission function for a model tight binding calculation. The three curves shown are similar, but the transmission minimum is shifted in energy with respect to E_F, i.e., by -0.4 eV (black), 0 eV (red) and $+0.2$ eV (blue), respectively. The right panel shows the corresponding dI/dV curves (same colour coding). They have been obtained from equation C.8 assuming a symmetric junction with $\eta = 0.5$ (full line) and slightly asymmetric junction with $\eta = 0.6$ (dashed line), respectively.

C.8 3-SITE MODEL

We shall now show that the two different paths in the three site model have a phase difference of π, and thus contribute with different signs. The three-site model derived from localized molecular orbitals (LMOs) is shown in figure C.7 with the LMO on-site energies and hopping parameters indicated.

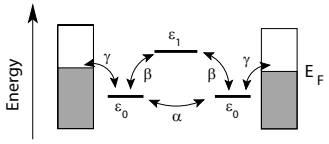

FIGURE C.7: Three-site model with on-site energies and hopping parameters indicated. For the calculations in Fig. 2 in the main text we use $\varepsilon_0 = -1.2$ eV, $\varepsilon_1 = 2.1$ eV, $\alpha = 0.04$ eV, $\beta = 0.24$ eV, and $\gamma = 0.4$ eV.[12]

Since only the left and right orbitals couple to the left and right electrodes,

respectively, the coupling matrices $\Gamma_{L,R}$ in Eq. (C.3) have the shapes

$$\Gamma_L = \begin{pmatrix} \gamma & 0 & 0 \\ 0 & 0 & 0 \\ 0 & 0 & 0 \end{pmatrix}, \quad \Gamma_R = \begin{pmatrix} 0 & 0 & 0 \\ 0 & \gamma & 0 \\ 0 & 0 & 0 \end{pmatrix}, \tag{C.10}$$

where we have assumed that the coupling is energy independent (the wide band limit approximation). From the general transmission formula (C.3) we then get

$$T(E) = \gamma^2 |\mathbf{G}_{12}(E)|^2, \tag{C.11}$$

so the transmission is determined by the (1,2) matrix element of the Green's function. Physically this quantity describes the propagation of an electron from site '1' (left) to site '2' (right). The 3-site Hamiltonian may be written as $\mathbf{H} = \mathbf{H_0} + \mathbf{V}$, where

$$\mathbf{H}_0 = \begin{pmatrix} \varepsilon_0 & 0 & 0 \\ 0 & \varepsilon_0 & 0 \\ 0 & 0 & \varepsilon_1 \end{pmatrix} \tag{C.12}$$

is the on-site Hamiltonian and

$$\mathbf{V} = \begin{pmatrix} 0 & \alpha & \beta \\ \alpha & 0 & \beta \\ \beta & \beta & 0 \end{pmatrix} \tag{C.13}$$

is the coupling between the sites. We now consider the two routes separately and set $\alpha = 0$ for the upper route and $\beta = 0$ for the lower route. Treating $\mathbf{V}$ as a perturbation we may obtain the full Green's function from the Dyson equation

$$\mathbf{G} = \mathbf{G}_0 + \mathbf{G}_0 \mathbf{V} \mathbf{G}, \tag{C.14}$$

where $\mathbf{G}_0(E) = (E\mathbf{I} - H_0 - \Sigma_L - \Sigma_R)^{-1}$, and the self energy matrices are related to the Γ-matrices by $\Gamma_{L,R}(E) = i(\Sigma_{L,R}(E) - \Sigma_{L,R}(E)^\dagger)$. For the lower route we iterate the Dyson equation (C.14) once to get the lowest order contribution and find

$$G_{1,2}^{lower} = \frac{\alpha}{(E - \varepsilon_0 + i\gamma/2)^2}. \tag{C.15}$$

Taking the upper route we need to iterate the Dyson equation twice (since there are two hops from left to right) and get

$$G_{1,2}^{upper} = \frac{\beta^2}{(E - \varepsilon_0 + i\gamma/2)^2 (E - \varepsilon_1)}. \tag{C.16}$$

Taking the ratio of the two contributions

$$\frac{G_{1,2}^{upper}}{G_{1,2}^{lower}} = \frac{\beta^2(E-\varepsilon_1)}{\alpha}, \tag{C.17}$$

we observe that for energies $E < \varepsilon_1$ the ratio has a *negative sign* showing that the two paths have a phase difference of π. Since the transmission depends quadratically on the Green's function element, the transmission through the three-site model is to leading order given by

$$T(E) = |\sqrt{T_{upper}} - \sqrt{T_{lower}}|^2. \tag{C.18}$$

for energies $E < \varepsilon_1 \approx E_{LUMO}$.

C.9 Measurements on other samples

Here we present supplementary figures showing results for **AQ-MT** for different samples (named sample 2 and 3 for clarity). First the 2D histogram of **AQ-MT** for sample 2 is shown in figureC.8. The overall shape of the dI/dV curves shown in figure 3b is well reproduced on this sample although the conductance values are lower than the ones found in figure 3b in the main text. The number of contacted molecules varies from tip to tip due to intrinsic differences in tip geometry. The displayed dI/dV curve is in agreement with theoretical calculations (see figure 4a, with a -0.5 eV shift) assuming we have 100 molecules bridging the junction.

A similar V-shaped dI/dV -curve is observed in the data displayed in figureC.9a. However, here the conductance values are much larger than in figure 3b of the main text. To investigate this interesting case further, we took a closer look at the tip geometry. On the scanning electron micrographs shown in figureC.9b we can clearly see the remains of a broken cantilever next to and more importantly below the actual cantilever used.

As a result the contact area in this case is much larger than for a regular tip i.e. much more molecules are contacted. Hence, this experimental incident confirms that the conductance is dependent on the number of molecules contacted. However, such an increase in contacted molecules does not affect the typical shape of the dI/dV-curve. We therefore show here that the overall shape of the dI/dV is independent on the number of molecules contacted.

C.10 I(V)-curves and alternative analysis

Here, we inspect the raw I(V)-curves obtained for AC-DT, AQ-DT and AQ-MT in more detail. We do so both for individual curves and for the ensemble of I(V)'s.

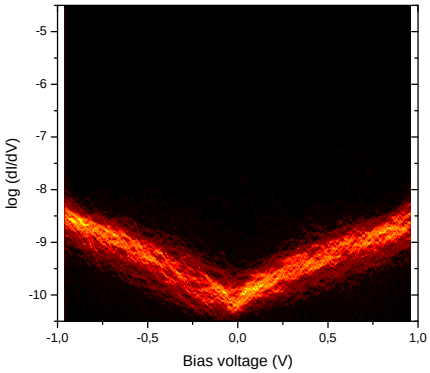

FIGURE C.8: 2D histogram for **AQ-MT** on sample 2 with the dI/dV (Ω^{-1})

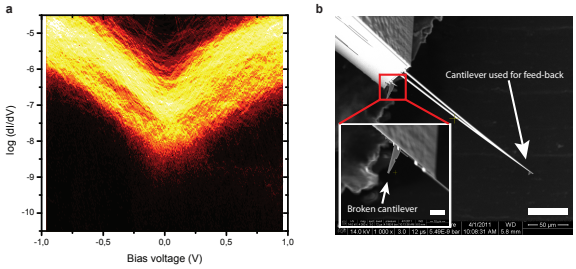

FIGURE C.9: **a**, 2D histogram for **AQ-MT** on sample 3 with the dI/dV (Ω^{-1}). **b**, SEM picture of the tip used for measurements shown in panel **a**. The overview of the chip is shown with the cantilever used and the remains of the broken one clearly at a lower position. In the inset we show a magnified picture of the broken cantilever. The scale bar in the picture is 50 μm and 10 μm in the inset.

This allows us to demonstrate the robustness of the features displayed in Figs. 1c (AC-DT) and 3a (AQ-DT) and 3b (AQ-MT).
In the Supplementary Methods section, we have explained how individual I(V)-curves are treated to obtain a 2D-histogram of dI/dV data for the ensemble. For AQ-MT, a clear zero-bias anomaly is observed in the resulting 2D-histogram (Fig. 3b). Here, we go back to the individual measurements to check that the zero-bias anomaly is truly intrinsic to single I(V)-curves. In figure C.10, we show three representative I(V)-curves for AQ-MT (a subset of the data in Fig. 3b, another curve is shown in figure C.1a). Each contains 1000 points, taken at a sample rate of 10 kHz (i.e. 0.1 s per curve). Raw data are presented, with original noise and a slight hysteresis. The latter is a result of the relatively large RC-time of the system at these high resistances. In figure C.11, we show a representative I(V)-curve for AC-DT. Upon inspection by eye, there is indeed a difference between the I(V)'s for AQ-MT and AC-DT. Whereas the curves in figure C.10 display a plateau with near-zero slope around zero bias, the curve in Fig. SC.11 has finite slope around zero bias. However, this distinction may be in the eye of the beholder. For that reason, we have taken the derivative of the individual I(V)'s, after smoothing. The resulting dI/dV-curves are displayed in Figs. SC.10b, d, and f for the AQ-MT case. Clearly, these curves show a negative curvature, except near zero bias where an anomaly is seen. This demonstrates that the anomaly in Fig. 3b stems from the individual I(V)-curves indeed. figureC.11b shows the dI/dV calculated from figure C.11a. It shows the same parabola-like shape that we found in Fig. 1c.

Now that we have checked individual I(V)- and dI/dV-curves, let us turn to the full ensembles of I(V)-curves. In figure C.12, we present the full batch of I(V)-curves for AC-DT (corresponding to Fig. 1c), AQ-DT (cf. Fig. 3a) and AQ-MT (samples presented in Fig. 3b and in figure C.9, i.e. with broken tip), respectively. To allow for a good comparison between the data sets for different molecules, all I(V)-curves have first been normalized in the current scale. Apart from that, these are raw data. Upon visual inspection, a plateau around zero bias is visible for the AQ-MT data set (Fig. SC.12c,d), which is not there for AC-DT and AQ-DT. However, such a distinction should be checked to be independent of the observer. It is for that reason that we performed the data analysis described in the Supplementary Methods section. Clearly, it is also important to demonstrate that the final conclusions do not depend on the exact analysis method chosen. Hence, we use a different statistical treatment below, by first determining average I(V)'s for the entire batch and then calculating the corresponding dI/dV.
In all panels of figure C.12, a red line represents the average of all I(V)-curves in the panel. In addition, a blue line represents an average of all curves, after

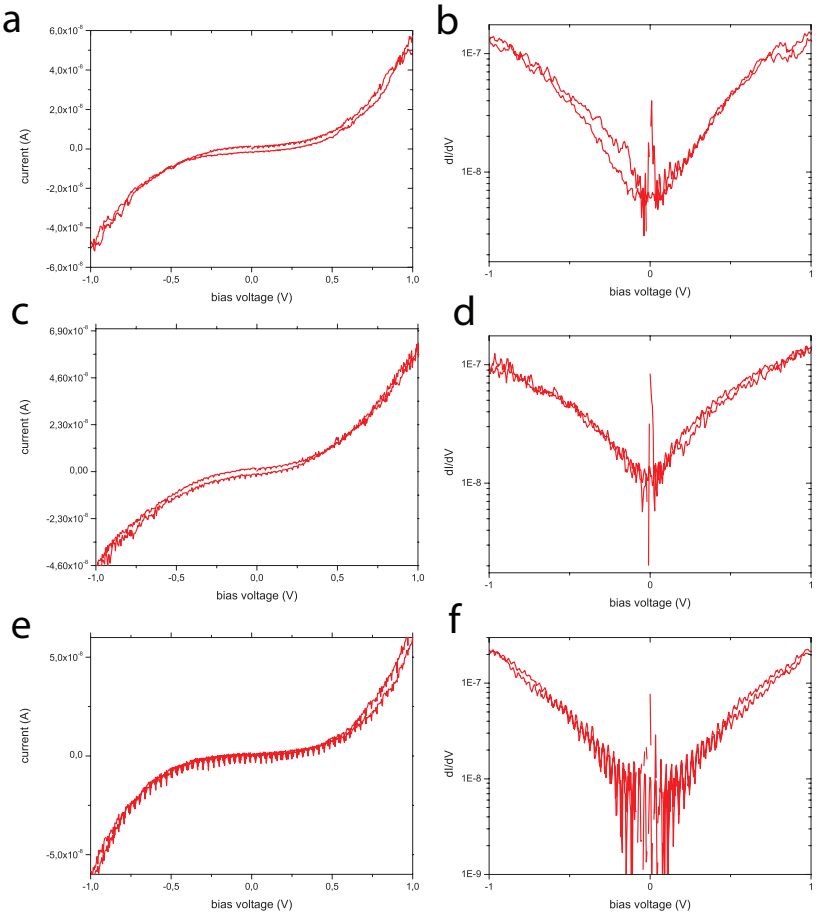

FIGURE C.10: a, c, e) typical raw I(V) traces for AQMT. b, d, f) dI/dV-traces based on the I(V)'s shown in a, c, e), respectively. The I(V)'s were first smoothed and then numerically differentiated

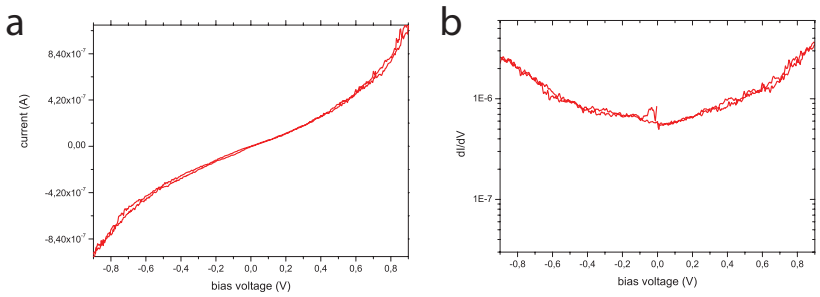

FIGURE C.11: a) typical raw I(V) trace for ACDT. b) dI/dV-trace based on the I(V) shown in a. The I(V) was first smoothed and then numerically differentiated

each I(V)-curve has first been smoothed (the blue line is almost indistinguishable from the red line). In figure C.13, we present the derivative of these two averaged I(V)-curves (again in red and blue, respectively) on a semi-log scale. For AC-DT and AQ-DT, these dI/dV's display a parabolic shape. For AQ-MT, however, the blue and red lines display negative curvature at all voltages except near $V = 0$, where an anomaly is seen. It is instructive to compare these curves to the data sets obtained by the analysis method described above. For this reason, the set of dI/dV-curves that were represented in Figs. 1c (AC-DT), 3a (AQ-DT), 3b (AQ-MT) and SC.9 (AQ-MT, "broken tip") are also plotted in Fig. SC.13a, b, c, and d respectively (in black, each curve is 99% transparent). We see that the shape of the average curves (red, blue lines) corresponds well with the individual curves, although there is some rounding off. For completeness, we note that logarithmic averaging of the absolute I(V)-curves leads to the same conclusions, i.e., a negative curvature and an anomaly is observed for AQ-MT, but not for AC-DT and AQ-DT.

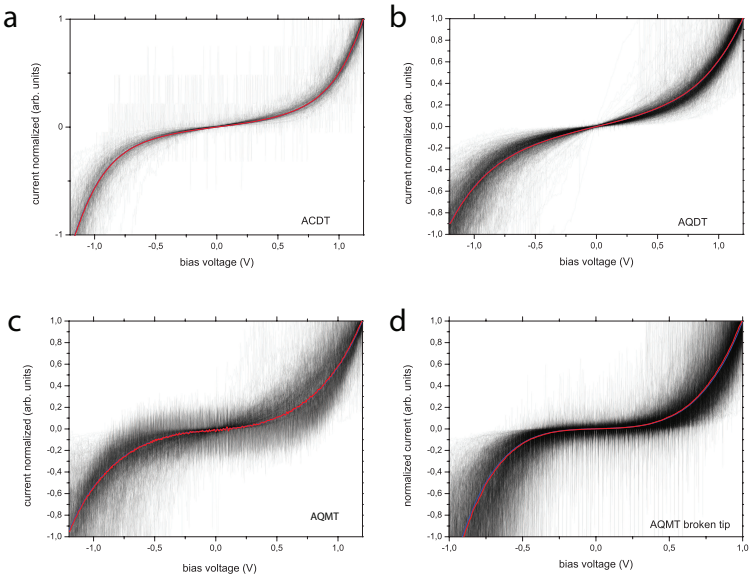

FIGURE C.12: I(V)-curves, with the current normalized. In grey, we show all the measured raw I(V)-traces. The black line represents the linearly averaged raw traces; the dark gray line represents linear average of the traces after they have been smoothed with a 50 points window. a) for ACDT, b) for AQDT, c) for AQMT and d) for AQMT with a broken tip as explained above

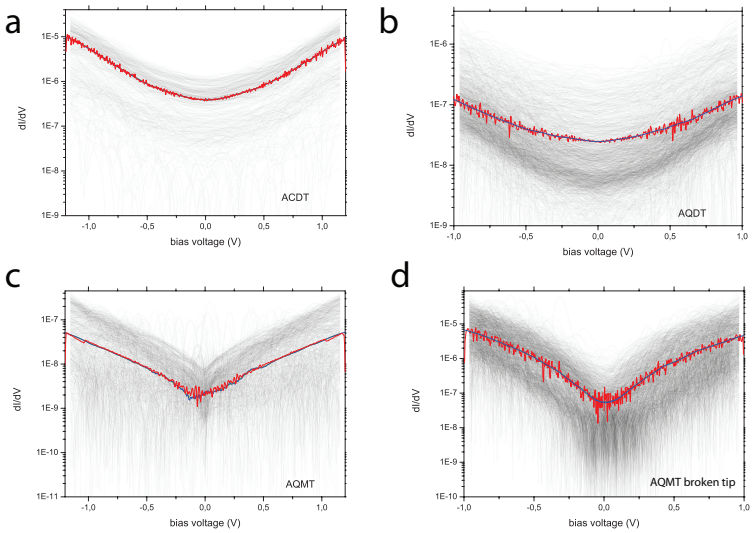

FIGURE C.13: dI/dV curves a) for ACDT, b) for AQDT, c) for AQMT and d) for AQMT with a broken tip as explained above. In grey: all the raw I(V) traces after smoothing and numerical differentiation, on a semi log scale. Black (dark gray) lines: numerical derivative of the black (dark gray) lines in the corresponding panels in Fig. C.12.

References

[1] H. Valkenier, E. H. Huisman, P. A. van Hal, D. M. de Leeuw, R. C. Chiechi, and J. C. Hummelen, *Formation of High-Quality Self-Assembled Monolayers of Conjugated Dithiols on Gold: Base Matters*, J. Am. Chem. Soc. **133**, 4930 (2011).

[2] J. Thome, M. Himmelhaus, M. Zharnikov, and M. Grunze, *Increased Lateral Density in Alkanethiolate Films on Gold by Mercury Adsorption*, Langmuir **14**, 7435 (1998).

[3] C. D. Bain and G. M. Whitesides, *Attenuation Lengths of Photoelectrons in Hydrocarbon Films*, J. Phys. Chem. **93**, 1670 (1989).

[4] J. Enkovaara, C. Rostgaard, J. J. Mortensen, J. Chen, M. Dulak, L. Ferrighi, J. Gavnholt, C. Glinsvad, V. Haikola, H. A. Hansen, et al., *Electronic structure calculations with GPAW: a real-space implementation of the projector augmented-wave method*, J. Phys Condens. Matter **22** (2010).

[5] J. J. Mortensen, L. B. Hansen, and K. W. Jacobsen, *Real-space grid implementation of the projector augmented wave method*, Phys. Rev. B **71**, 035109 (2005).

[6] A. H. Larsen, M. Vanin, J. J. Mortensen, K. S. Thygesen, and K. W. Jacobsen, *Localized atomic basis set in the projector augmented wave method*, Phys. Rev. B **80**, 195112 (2009).

[7] J. P. Perdew, K. Burke, and M. Ernzerhof, *Generalized gradient approximation made simple*, Phys. Rev. Lett. **77**, 3865 (1996).

[8] J. M. Garcia-Lastra, C. Rostgaard, A. Rubio, and K. S. Thygesen, Phys. Rev. B **80**, 245427 (2009).

[9] D. J. Mowbray, G. Jones, and K. S. Thygesen, *Influence of functional groups on charge transport in molecular junctions*, J. Chem. Phys. **128**, 111103 (2008).

[10] S. Y. Quek, H. J. Choi, S. G. Louie, and J. B. Neaton, Nano Lett. **9**, 3949 (2009).

[11] J. Z. Chen, T. Markussen, and K. S. Thygesen, *Quantifying transition voltage spectroscopy of molecular junctions: Ab initio calculations*, Phys. Rev. B **82**, 121412 (2010).

[12] T. Markussen, J. Schiötz, and K. S. Thygesen, *Electrochemical control of quantum interference in anthraquinone-based molecular switches*, J. Chem. Phys. **132**, 224104 (2010).

SAMENVATTING

Het wetenschappelijk vakgebied van 'moleculair ladingstransport' is ontstaan in de jaren zeventig van de vorige eeuw. De oorspronkelijke droom was om op termijn de traditionele elektronicacomponenten zoals transistoren, diodes en weerstanden te vervangen door moleculen van slechts enkele nanometers groot (een nanometer is een miljoenste millimeter). Nu ligt de nadruk meer op fundamentele vragen over de invloed van de chemische structuur van moleculen op hun geleidingseigenschappen enerzijds, en op toepassingen in de organische elektronica anderzijds. Het bestuderen van moleculair ladingstransport vormt daarmee een basis voor het begrijpen van verschijnselen relevant voor organische elektronica. Organische elektronica is een verzamelnaam voor toepassingen waar een groot deel van de componenten vervangen is door organische films of polymeren, bijvoorbeeld flexibele elektronica, organische zonnecellen en printbare elektronica.

In dit proefschrift wordt er gekeken naar de relatie tussen de structuur van de moleculaire orbitalen en de geleidingseigenschappen. Door de stroom (I in Ampère) te meten bij bepaalde spanningen (V in Volts) kan de geleiding ($G = I/V$ in Siemens) worden bepaald voor verschillende moleculen.

In figuren C.14, C.15 en C.16 zijn de verschillen tussen de door mij gemeten soorten moleculen schematisch weergegeven. De categorie 'geconjugeerd' geleidt het meest (felste lampje). Geconjugeerde moleculen zijn te herkennen aan een strikte afwisseling van enkele (C−C) en dubbele (of drievoudige) (C=C, C≡C) koolstofbindingen door het molecuul. In degelijke moleculen zijn de zogenaamde π-orbitalen gedelocaliseerd, wat resulteert in een begaanbaar pad voor elektronen om door het molecuul heen te reizen. Niet-geconjugeerde moleculen zoals alkanen, daarentegen hebben geen gedelocaliseerde π-orbitalen en daardoor een veel lagere geleiding dan geconjugeerde moleculen. De categorie 'kruisgeconjugeerd' ten slotte, geleidt verrassend slecht. Kruisgeconjugeerde moleculen lijken op lineair geconjugeerde moleculen, omdat ook hier elk koolstofatoom een dubbele (of drievoudige) binding heeft. Deze moleculen hebben echter geen strikte afwisseling van enkele en dubbele (of drievoudige) bindingen tussen de uiteinden van het molecuul. Er is echter wel een soort conjugatie in de vorm van een zijpad (in figuur C.16 de twee C=O zijgroepen).

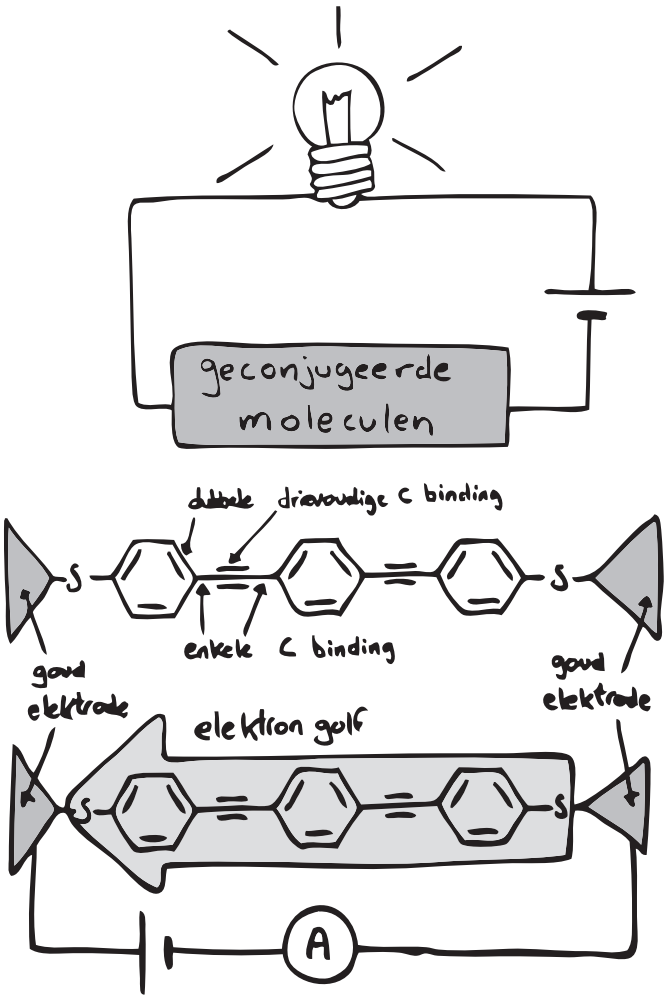

FIGUUR C.14: **Schematische weergaven van de geconjugeerde moleculen gemeten in dit proefschrift.**

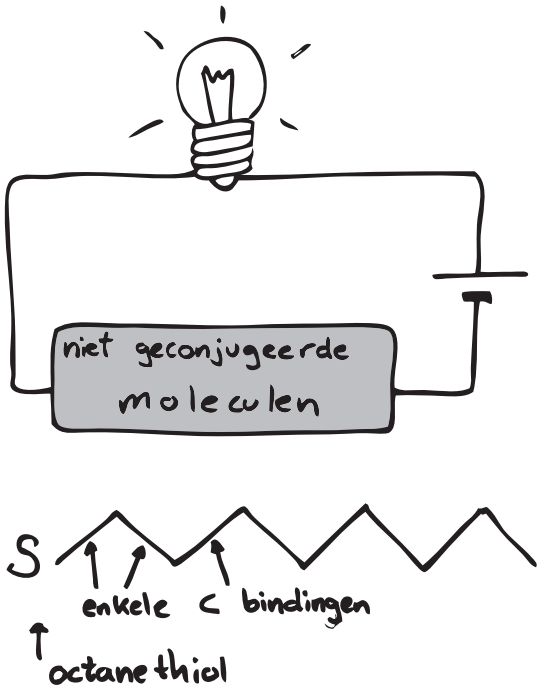

FIGUUR C.15: **Schematische weergaven van de niet geconjugeerde moleculen gemeten in dit proefschrift.**

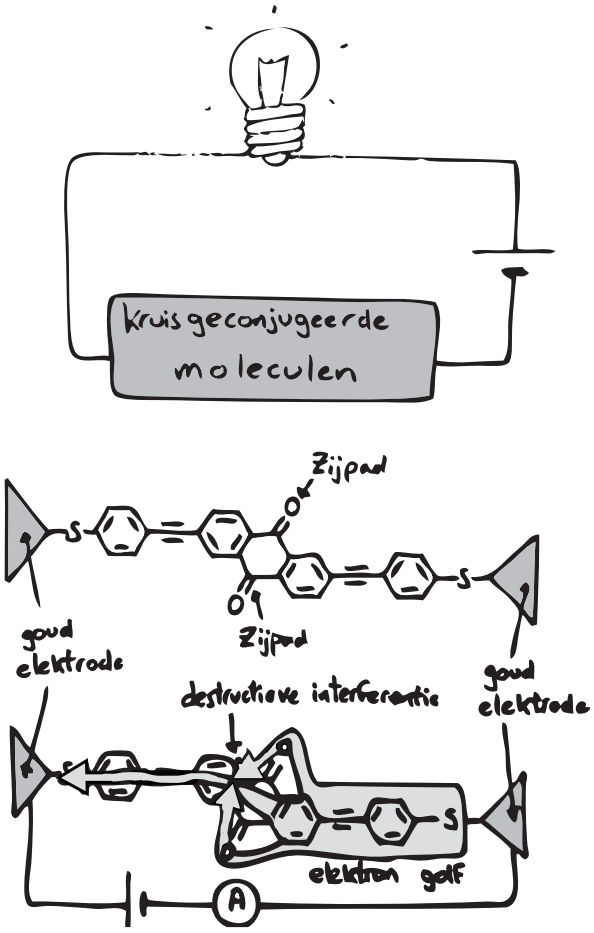

FIGUUR C.16: **Schematische weergaven van de kruisgeconjugeerde moleculen gemeten in dit proefschrift.**

Hierdoor ontstaan er twee mogelijke routes voor een elektron door het molecuul. Eentje rechtdoor en eentje met een omweg in een van de zijpaden. Een elektron gedraagt zich als een golf. Deze golf kan zich opsplitsen in verschillende golfjes die elk met hun eigen route door het kruisgeconjugeerde molecuul lopen. Deze golfjes ontmoeten elkaar weer aan het eind van het molecuul. Als de golven precies in tegenfase lopen (de een gaat net door zijn maximum als de ander net door zijn minimum gaat), heffen ze elkaar op. Er kunnen dan geen (of veel minder) elektronen door het molecuul lopen en de stroom wordt dus klein of nul. Dit fenomeen heet destructieve interferentie en was al wel bekend voor grotere metallische structuren bij heel lage temperaturen. In dit proefschrift laten we zien dat het ook mogelijk is om die interferenties te observeren met moleculen bij kamertemperatuur (hoofdstuk *zes*).

Een uitdaging was om contact te maken met de moleculen via elektroden aan de meetelektronica. In dit proefschrift beschrijven we twee technieken, beide gebaseerd op de goud-zwavel binding (Au-S) tussen het organische deel (molecuul met een zwavel atoom aan het uiteinde) en het anorganische deel (goud elektroden). In hoofdstuk *twee* en *drie* maken we gebruik van een netwerk van goud nanodeeltjes om uiteindelijk een twee-dimensionaal molecuul -nanodeeltje-netwerk te krijgen. Een schematische weergave van een dergelijke netwerk is afgebeeld in figuur C.17. Op deze manier kunnen we de geleiding bepalen van een hele verzameling moleculen en dus ook een soort ruimtelijke gemiddelde bepalen voor een enkel molecuul. Deze techniek heeft als voordeel dat we genoeg moleculen hebben om optische metingen te verrichten, wat niet mogelijk is met enkel-moleculaire juncties. In hoofdstuk *drie* laten we zien dat we een netwerk kunnen uitrekken en zo de afstand tussen de nanodeeltjes kunnen beïnvloeden. Door te kijken naar de verandering in de geleiding kunnen we de deformatie van het molecuul-nanodeeltjes netwerk monitoren. In feite werkt het netwerk nu als een 'rekstrookje' met extra gevoeligheid, omdat het gebaseerd is op quantummechanisch geleiden door moleculen: een kleine uitrekking leidt tot een grote verandering in geleiding. In hoofdstuk *vijf* en *zes* gebruiken we een techniek gebaseerd op AFM (atomic force microscope; atomaire krachtmicroscoop): C-AFM (conducting-AFM). Hier assembleren we de moleculen loodrecht op een goud oppervlakte (onderste elektrode) en maken we contact via het goud-bedekte punt van de AFM (bovenste elektrode). De regeltechniek van de AFM maakt het mogelijk om de moleculen met een kleine kracht aan te raken. In ons geval worden de moleculen met maar twee nanoNewtons aangedrukt. Met deze techniek maken we contact met ongeveer honderd moleculen in parallel. Een schematische uitleg van de opstelling is te vinden in figuur C.18.

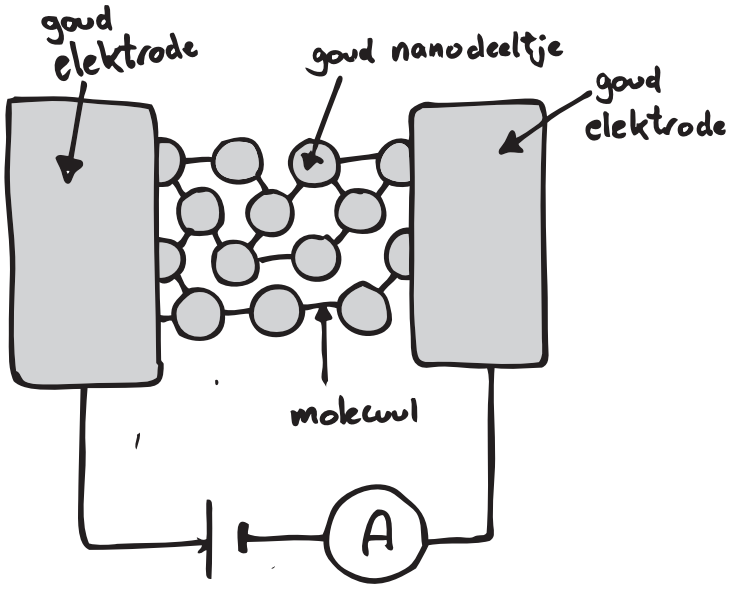

FIGUUR C.17: **Schematische weergave van een netwerk van nanodeeltjes verbonden door moleculaire bruggen.** .

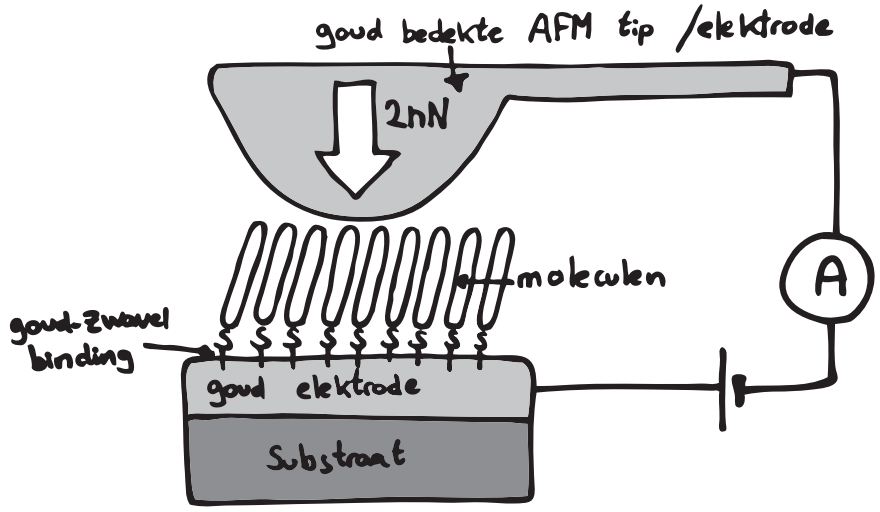

FIGUUR C.18: **Schematiche weergaven van een C-AFM opstelling.** .

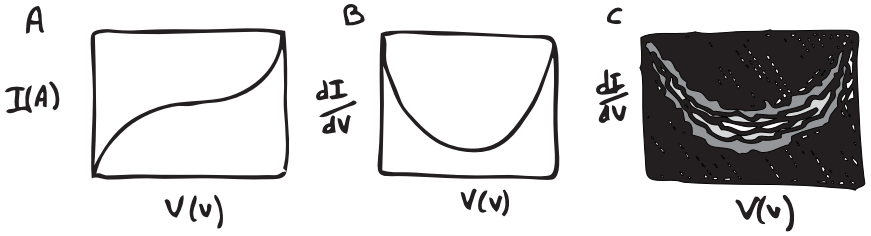

FIGUUR C.19: **A I-V curven, B afgeleiden en C 2D histogrammen.** .

In beide technieken wordt een spanning tussen de twee elektrodes aangebracht en wordt de stroom gemeten met behulp van een versterker (I-V converter). De resultaten worden meestal als een zogenaamd 'I-V curve' gepresenteerd zoals is te zien in figuur C.19 A. In hoofdstuk *vijf* en *zes* wordt ook de eerste afgeleide van de stroom, $\frac{dI}{dV}$, de differentiele geleiding, gebruikt (figuur C.19 B). In figuur C.19 C is ook te zien hoe we meerdere (duizenden) curven combineren tot een kleurengrafiek. Hier correspondeert de kleur met de hoeveelheid curven, zwart staat voor geen curven en wit voor veel (typisch honderd). In deze zogenaamd '2D-histograms' is zowel de algemene vorm van de curven als de spreiding in de data te zien.

In hoofdstuk *vier* geven we een kritische bespreking van een nieuwe manier om 'I-V' curven te analyseren, de zogenaamde 'transition voltage spectroscopy' (TVS). We laten zien door simpele theorie en slimme experimenten dat TVS niks toevoegt aan de informatie die al aanwezig is in de 'I-V' curven. Bovendien laten we zien dat het transitieminimum (V_m) geen bijzondere fysisch betekenis heeft.

Met dit proefschrift heb ik een bijdrage geleverd aan het uitpluizen van de relatie tussen moleculaire orbitalen en geleidingseigenschappen. Meer werk is nodig om een volledige overzicht te krijgen van de invloed van chemische structuur op de geleiding van organische moleculen. Uiteindelijk zal het mogelijk zijn om een set van ontwerpregels op te stellen die chemici kunnen gebruiken om een breed scala aan functionaliteit te integreren in organische elektronica.

Dankwoord

Ik wil graag iedereen bedanken die rechtstreeks of zijdelings betrokken is geweest bij het onderzoek beschreven in dit proefschrift. In het bijzonder gaat mijn dank uit naar: Sense Jan voor zijn begeleiding en enthousiasme. Jan van Ruitenbeek omdat hij naast het directeurschap van het instituut ook nog mijn promotor heeft willen zijn. Zowel de leden van mijn promotiecommissie als die van mijn oppositiecommissie. Federica en Marcel voor hun onmisbare hulp. Hennie voor de moleculen en vooral voor de leuke samenwerking. Troels en Kristian voor de theoretische ondersteuning. Monica voor de geweldige tijd in en buiten 716b. Bert en Raymond van de ELD voor alle elektronische assistentie. Ruud, Ewie en Martijn van de FMD voor het oplossen van al mijn fijnmechanische problemen. Daniëlle, Ellie, Barry en Daniëlle voor alle hulp. De leden van de AMC groep voor alle interactie, geweldige werksfeer en inspiratie. De leden van de MSN groep voor de leuke woensdagochtenden. Afstudeerstudenten Max, Jeroen, Marijn, Inge en Peter voor de samenwerking. Alle mensen van de zevende verdieping voor de heerlijke koffie. Mijn paranimfen, Edwin en Monica. Mijn ouders en Annetje voor alles wat heeft geleid tot dit wetenschappelijke avontuur. En natuurlijk Katelijne en Lucas zonder wie dit boek (en veel meer) nooit gelukt zou zijn ♡.

Curriculum Vitæ

Constant Guédon

Constant Guédon werd geboren in Den Haag op 18 september 1979. Na vele omzwervingen rond de wereld haalde hij, in 1997, zijn Baccalaureat diploma bij Lycée Sainte-Marie de Fenelon in Parijs. In 1998 ging hij levensmiddelentechnologie studeren aan de landbouwuniversiteit (later Wageningen Universiteit) in Wageningen. In 2007 studeerde hij af in de levensmiddelen-proceskunde, waarvoor hij twee onderzoeksprojecten deed. Het eerste onderzoek betrof de ontwikkeling van polymeren microcapsules voor ultrasoontherapie en diagnostiek onder begeleiding van dr. M. Böhmer en dr. K. Schöen bij Philips Research in Eindhoven. Voor het tweede onderzoek werkte hij onder supervisie van dr. C.A. Martin en prof. dr. ir. H.S.J. van der Zant aan moleculaire schakelaars en aan de toepassing van CdSe nanodeeltjes in nanojuncties, bij de MED groep van de TU Delft. Na zijn afstuderen begon hij zijn promotieonderzoek aan de Universiteit Leiden in het Kamerlingh Onnes Laboratorium, als lid van de *Atomic and molecular conductors* vakgroep, onder begeleiding van dr. ir. S.J. van der Molen. Het onderzoek dat hij heeft verricht staat beschreven in dit proefschrift. Met ingang van het najaar van 2012 zal hij werkzaam zijn bij het Shell Technology Center Amsterdam.

List of Publications

1. C. Chlon, C. M. Guédon, B. Verhaagen, W. T. Shi, C. S. Hall, J. Lub, and M. R. Boehmer, *Effect of Molecular Weight, Crystallinity, and Hydrophobicity on the Acoustic Activation of Polymer-Shelled Ultrasound Contrast Agents*, **Biomacromolecules**, **10**, 1025 (2009).

2. E. H. Huisman, C. M. Guédon, B. J. van Wees, and S. J. van der Molen, *Interpretation of Transition Voltage Spectroscopy*, **Nano Letters**, **9**, 3909 (2009).

3. C. M. Guédon, J. Zonneveld, H. Valkenier, J. C. Hummelen, and S. J. van der Molen, *Controlling the interparticle distance in a 2D molecule-nanoparticle network*, **Nanotechnology**, **22**, 125205 (2011), see also:

   Selected for IOP select http://iopscience.iop.org/collections

   Featured on Nanotechweb http://nanotechweb.org/cws/article/lab/45592

4. M. L. Trouwborst, C. A. Martin, R. H. M. Smit, C. M. Guédon, T. A. Baart, S. J. van der Molen and J. M. van Ruitenbeek, *Transition Voltage Spectroscopy and the Nature of Vacuum Tunneling*, **Nano Letters**, **11**, 614 (2011).

5. C. M. Guédon, H. Valkenier, T. Markussen, K. S. Thygesen, J. C. Hummelen and S. J. van der Molen, *Observation of quantum interference in molecular charge transport*, **Nature Nanotechnology**, **7**, 281 (2012), see also:

   News and views **Nature Nanotechnology**, **7**, 305 (2012)

6. J. Dayen, E. Devid, M. V. Kamalakar, D. Golubev, C. M. Guédon, V. Faramarzi, B. Doudin and S. J. van der Molen, *Enhancing the molecular signature in molecule-nanoparticle networks via inelastic co-tunneling*, Accepted for publication in **Advanced Materials**

7. H. Valkenier, C. M. Guédon, T. Markussen, K. S. Thygesen, S. J. van der Molen and J. C. Hummelen, *Relationship between the π-Conjugation Pattern and Quantum Interference in Charge Transport through Molecular Wires*, in preparation.